DEVELOPING AN ENERGY-DISSIPATING PLASTIC HINGE CELL FOR
EARTHQUAKE PROTECTION OF BUILDINGS

A THESIS SUBMITTED TO
THE GRADUATE SCHOOL OF NATURAL AND APPLIED SCIENCES
OF
MIDDLE EAST TECHNICAL UNIVERSITY

BY

SADUN TANIŞER

IN PARTIAL FULFILLMENT OF THE REQUIREMENTS
FOR
THE DEGREE OF DOCTOR OF PHILOSOPHY
IN
CIVIL ENGINEERING

MARCH 2024

Approval of the thesis:

DEVELOPING AN ENERGY-DISSIPATING PLASTIC HINGE CELL FOR EARTHQUAKE PROTECTION OF BUILDINGS

submitted by **SADUN TANIŞER** in partial fulfillment of the requirements for the degree of **Doctor of Philosophy** in **Civil Engineering, Middle East Technical University** by,

Prof. Dr. Naci Emre Altun
Dean, Graduate School of **Natural and Applied Sciences**   _____

Prof. Dr. Erdem Canbay
Head of the Department, **Department of Civil Engineering**   _____

Prof. Dr. Haluk Sucuoğlu
Supervisor, **Department of Civil Engineering, METU**   _____

Examining Committee Members:

Prof. Dr. H. Polat Gülkan
Department of Civil Engineering, Başkent University   _____

Prof. Dr. Haluk Sucuoğlu
Department of Civil Engineering, METU   _____

Prof. Dr. M. Altuğ Erberik
Department of Civil Engineering, METU   _____

Prof. Dr. Cem Topkaya
Department of Civil Engineering, METU   _____

Asst. Prof. Dr. F. Soner Alıcı
Department of Civil Engineering, Başkent University   _____

Date: 08.03.2024

I hereby declare that all information in this document has been obtained and presented in accordance with academic rules and ethical conduct. I also declare that, as required by these rules and conduct, I have fully cited and referenced all material and results that are not original to this work.

Name, Last name : Sadun Tanışer

Signature :

ABSTRACT

DEVELOPING AN ENERGY-DISSIPATING PLASTIC HINGE CELL FOR EARTHQUAKE PROTECTION OF BUILDINGS

Tanışer, Sadun
Doctor of Philosophy, Civil Engineering
Supervisor: Prof. Dr. Haluk Sucuoğlu

March 2024, 173 pages

Capacity design is the prevailing seismic design procedure for ductile frame systems. It permits formation of plastic hinges at the beam ends for dissipating the seismic energy imparted by strong ground motions through inelastic response, hence reducing seismic demand in frame members. These reduced force demands however have a cost: Increased deformations and displacements, and more importantly damage caused by nonlinear deformations which occur at the formed plastic hinges.

A replaceable plastic hinge (P-Cell) is developed in this study that is placed at the beam-ends during construction. P-Cell is a metallic internal energy dissipating device whose dimensions fit to the beam dimensions whereas its length along the beam is significantly smaller than the beam depth. P-Cell dissipates energy through cyclic moment-rotation response with rotations exceeding 0.05 radians. Their moment capacity is adjusted to values lower than the end-moment capacity of the connecting beams. Hence, entire nonlinear deformations in the frame system occur at the P-Cells, leaving all other members in the linear elastic range during the earthquake.

Seismic performance of P-Cells has been verified by laboratory testing under severe load reversals. Further, a two-story steel frame equipped with P-Cells at the first story beam ends is tested through PsD testing. P-Cells which develop inelastic response during the earthquake can be removed and replaced, accordingly the remaining linear elastic frame restores the deformations.

P-Cells can be easily implemented in modular steel and precast concrete frame systems. Their implementation in cast-in-place RC is also straight forward with the provided connection details.

Keywords: Seismic Response, Energy Dissipating Device, Plastic Hinge Cell, Replaceable Device

ÖZ

BİNALARIN DEPREME KARŞI KORUNMASI İÇİN ENERJİ SÖNÜMLEYİCİ PLASTİK MAFSAL HÜCRESİ GELİŞTİRİLMESİ

Tanışer, Sadun
Doktora, İnşaat Mühendisliği
Tez Yöneticisi: Prof. Dr. Haluk Sucuoğlu

Mart 2024, 173 sayfa

Kapasite tasarımı, sünek çerçeve sistemleri için en geçerli sismik tasarım prosedürüdür. Kapasite tasarımı, güçlü yer hareketlerinin neden olduğu sismik enerjiyi inelastik davranış yoluyla sönümlemek için kiriş uçlarında plastik mafsalların oluşmasına izin verir, böylece çerçeve elemanlarındaki sismik talebi azaltır. Ancak bu azaltılmış kuvvet taleplerinin bir maliyeti vardır: Artan deformasyonlar ve yer değiştirmeler, daha da önemlisi kiriş uçlarındaki plastik mafsallarda oluşan doğrusal olmayan deformasyonların neden olduğu hasar.

Bu tez çalışmasında, yapıda kiriş uçlarına inşaat sırasında yerleştirilen değiştirilebilir bir plastik mafsal (P-Cell) geliştirilmiştir. P-Cell, boyutları kiriş boyutlarına uyan ve kiriş boyunca uzunluğu, derinliğinden önemli ölçüde daha küçük olan metalik, dahili bir enerji sönümleyici cihazdır. P-Cell, 0.05 radyanı geçen dönme genlikleri ile ve çevrimsel moment-dönme ilişkisi yoluyla enerjiyi sönümler. P-Cell moment kapasitesi, P-Cell'in bağlandığı kirişin uç moment kapasitesinden daha düşük değerlere ayarlanmaktadır. Bu nedenle, çerçeve sistemindeki tüm doğrusal olmayan

deformasyonlar, deprem sırasında diğer tüm elemanları elastik bırakarak P-Cell'lerde oluşur.

P-Cell'lerin sismik performansı, şiddetli tersinir yüklemeler altında laboratuvar testleri ile doğrulanmıştır. Ayrıca, birinci kat kiriş uçlarına P-Cell'ler yerleştirilmiş iki katlı bir çelik çerçeve, dinamik benzeri testler ile test edilmiştir. Deprem sırasında inelastik davranış gösteren P-Cell'ler çerçeve sisteminden çıkarılabilir ve değiştirilebilir, buna bağlı olarak doğrusal elastik seviyede kalan çerçeve, kendisini eski haline getirir.

P-Cell'ler modüler çelik ve prefabrik beton çerçeve sistemlerde kolaylıkla uygulanabilir. Yerinde dökme betonarme çerçevede uygulamaları da gerekli bağlantı detaylarının sağlanmasıyla birlikte basit bir uygulamadır.

Anahtar Kelimeler: Sismik Tepki, Enerji Sönümleyici Cihaz, Plastik Mafsal Hücresi, Değiştirilebilir Cihaz

My family and friends

ACKNOWLEDGMENTS

I would like to thank my thesis advisor, Prof. Dr. Haluk Sucuoğlu for his guidance, support, and patience through this long journey, besides being my advisor and mentor throughout my graduate life. It would not be possible to do this study without his inventive thinking, vision, and drive.

I also thank Prof. Dr. Polat Gülkan and Prof. Dr. Altuğ Erberik, who were also my progress committee members; Prof. Dr. Cem Topkaya, Dr. Soner Alıcı, Dr. Kaan Kaatsız and Dr. Salim Azak for their contributions, guidance, and suggestions throughout the study. I shall also express my gratitude to Salim for his companionship that I always felt while I was in the lab.

Another group of people that played a big part in achieving this study is the people of TİS. I thank all the employees of the factory for their labor and opinions they shared where necessary. Especially, I would like to thank Uğurcan Özçamur for his support, friendship, advice, and patience where it surely matters the most.

My gratitude to my mother and sister is far beyond all the expressions. I love them and consider myself very lucky to be their son and brother they always support unconditionally.

I have similar feelings for my friends who accompany me through my life as well as this study, for which I am grateful. I shall mention their names; Ali, Alp, Serdar, AFKoç, Suzan, Berker, Erdinç, Serap, Erhan, Betül, Kaan, Ahmet Abi, Bahar and Owain Pedgleys. Their presence is what makes my life more enjoyable, and easier.

TABLE OF CONTENTS

xii

LIST OF TABLES

TABLES

LIST OF FIGURES

FIGURES

xv

CHAPTER 1

INTRODUCTION

1.1 Problem Statement

In the current practice of earthquake engineering, structures are designed with the premise that heavy damage or collapse during a severe earthquake will be prevented, but that they will experience a certain level of damage in a way that the life safety of the inhabitants is ensured. It is practically not possible to design an economical and undamaged structure under the force levels calculated according to the earthquake hazards defined for the design level in current earthquake-resistant design standards. Based on the earthquake hazard in question, behavior in the linear elastic range, hence an undamaged structural response during a design level earthquake may mean that the structure sustains a lateral earthquake force capacity at an order close to its weight. Considering the structure types and their material properties that constitute the common building stock of a particular region, such level of earthquake intensity creates internal forces that will not make the design of structural elements possible. Therefore, earthquake forces should be reduced with certain approaches in order to make structural design in high-hazard seismic zones practical. The use of reduced seismic forces in the design also brings about the pre-acceptance that the structure will suffer a certain level of damage during the considered earthquake.

Admittedly, designing a structure by accepting in the first place that it will be damaged may be seen as a weakness of earthquake-resistant structural design principles, although the design is done using widely accepted methods in the literature and standards. These weaknesses arise from the fundamentals of those design methods and the uncertainties that they may have. While explaining these

weaknesses and uncertainties, it is necessary to mention the principles on which earthquake resistant design is based. The first of these is the expected damage mode of the structure to be designed. When designing a structure, it is accepted that the damage must be of ductile nature, in other words, in the flexural mode, and brittle damage to any element must be strictly avoided in order to achieve the targeted performance level.

In addition to the principles consisting of determining the damage mode in structural elements in this way, another principle is to ensure that the expected damage will occur in the pre-determined order in the structural elements. This principle is called the plastic hinging hierarchy in literature and in practice. As its name implies, the well-known principle states that in order to achieve a significant post-elastic behavior of the structure under a severe earthquake and sustainable damage control to utilize life-safety performance level, expected plastic deformation in the structural elements shall follow a certain sequence throughout the structure. For instance, in a classical moment resisting frame structure, columns shall exhibit plastic deformation only after a significant number of beams exceed their elastic deformation level. This is achieved through another well-defined and applied principle of seismic design methods, which is called "strong column-weak beam principle". This principle is practiced by designing the columns connecting to a particular joint with a higher strength capacity than the connecting beams so that beams will reach their force capacity and start to exhibit post-elastic deformation before the columns. Only in that way, a structure shall possess a significant deformation capacity without collapse, which is accepted as a crucial advantage during an earthquake.

Besides the damage mode of the structure resulting from the damage that the lateral load-carrying members suffer and the damage sequence, the deformation level the structure sustains also creates a certain level of uncertainty. This uncertainty is due to the nature of the earthquakes that cause the damage because they cannot be predicted thoroughly and related seismic parameters such as acceleration and displacement are determined probabilistically. According to the capacity design, which includes design principles such as hinging hierarchy and strong column-weak

beam principle, there is some uncertainty at what level they will be damaged in the region of post-elastic deformations, although the structural elements reach their clearly defined strength capacities.

Until recently, this basic phenomenon of earthquake resistant design was included in design standards and common practice as an approach that allows design against severe earthquakes while ensuring the life safety of inhabitants, despite the aforementioned weaknesses. It is still widely accepted and used according to the intended use and service life of the building in question. However, although it makes the design possible under severe earthquakes, this performance level and practice, which accepts that structures will be damaged in certain situations and structural systems, when high performance is desired and required, has begun to be considered insufficient by the designers, owners, and administrations. For various reasons, it is desired that the structures continue their functionality without being damaged even in severe earthquakes. These reasons can be listed as follows.

1. Buildings need to be used after an earthquake depending on their intended performance. For example, hospitals have to continue their services in the disaster area even after a very severe earthquake. Bridges and viaducts, and airports, should ensure continued transportation. Similarly, the buildings of public institutions responsible for post-disaster management should remain functional.

2. Demanding the use of buildings with high commercial value without incurring high operating and/or repair costs such as repairs and rebuilding after earthquakes.

3. Targeting high performance, such as no-damage at the building scale, increases earthquake resilience at the regional scale. Targeting the acceleration and cost reduction of the region's return to normalcy after the disaster.

It has become essential to develop and use advanced technologies in earthquake-resistant design and construction applications, due to the concerns of all stakeholders

of civil engineering applications. Beyond the resistance of buildings against earthquakes, the development of advanced technologies has come to the fore in order to increase earthquake resilience of both the structures and the earthquake region. The main reason for the damage occurrence at the load-carrying components of a structure is the demand to dissipate the energy stored in the structure in various ways during an earthquake. For this reason, the primary development that needs to be done in order to prevent the components of the structure from being damaged is to provide additional energy dissipation capacity to the structure in question with various methods and devices. Research and development studies carried out in the literature on this subject and turned into practical engineering practice so far have been in this direction.

The research and development in the literature and practice, which have shown their effectiveness in different building types, can be grouped as follows.

1. Seismic base isolation
2. External energy-dissipation devices
   a. Metallic dampers
   b. Friction dampers
   c. Fluid viscous dampers
   d. Buckling-restrained braces
   e. Tuned mass dampers
3. Internal energy-dissipation devices: Constructed plastic hinges

These technologies are briefly described in the following paragraphs.

Seismic Base Isolation

Seismic base isolation is one of the most prominent earthquake engineering technologies, which is being used for the protection of the structures against the effects of earthquakes. The technology is based on the separation of the superstructure from the substructure and the ground via specifically designed and manufactured devices called seismic isolators. The main rationale of the separation

of the structure is to reduce the movement transmitted from the ground to the superstructure and its members, and to accumulate the displacement demand at a certain interface, commonly named as base isolation floor. Besides these two main behaviors, seismic base isolation also achieves the addition of energy dissipation capacity and re-centering capacity to the structure thanks to the geometrical and material properties of the seismic isolators.

Seismic isolators are designed to create an interface having considerably low horizontal stiffness as compared to the stiffness of the superstructure stories in order to achieve aforementioned reduction in movement and displacement accumulation. The stiffness of this interface is so low that the dynamic behavior of the entire structure is dominated by the dynamic properties of the isolation system, i.e., the structure has a much longer fundamental vibration period and higher energy dissipation capacity, resulting in much lower design acceleration values. The seismic isolators achieve these modified dynamic properties as a result of low stiffness, with their low-friction surfaces or usage of very low-stiffness materials, according to their type.

There are two main types of seismic isolators, which are currently available in the market. The first and older one is the rubber isolator, mainly subdivided as high damping rubber bearing (HDRB) and lead-rubber bearing (LRB) (Figure 1.1a). Low horizontal stiffness and energy dissipation capacity in both types are provided mainly by shear stiffness and chemical properties of the rubber material, while they are also modified by placing inside a lead core in the LRB type. The vertical load-carrying capacity is provided by the steel sheets placed inside the rubber as a predetermined number of layers. The second and newer isolator type is the curved surface slider (CSS), in other words, the friction pendulum (FPS) isolator (Figure 1.1b). In this type of isolator, low stiffness and energy dissipation capacity are provided by a sliding interface, which is created by mating a low-friction, high-strength sliding material with a stainless-steel surface having a very low friction. Vertical load-carrying capacity, on the other hand, is provided with high compressive strength of

both sliding material and main components of the isolators, manufactured by structural steel.
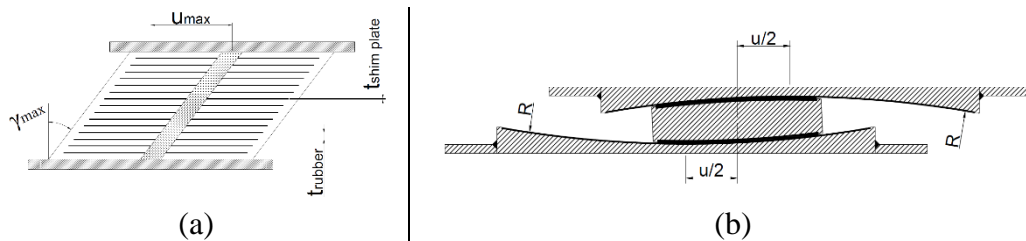
Figure 1.1: Seismic isolators. (a) Rubber isolator (b) Friction pendulum isolator

Metallic Dampers

Metallic dampers have emerged as highly favored devices for energy dissipation in structural earthquake engineering. These dampers are specifically designed to absorb and dissipate energy induced by seismic excitation, wind loads, or dynamic forces in general, thereby enhancing structural resilience and reducing the risk of structural damage. Manufactured from mild steel or other metallic alloys, these dampers possess considerable ductility and energy-dissipation capabilities (Figure 1.2).
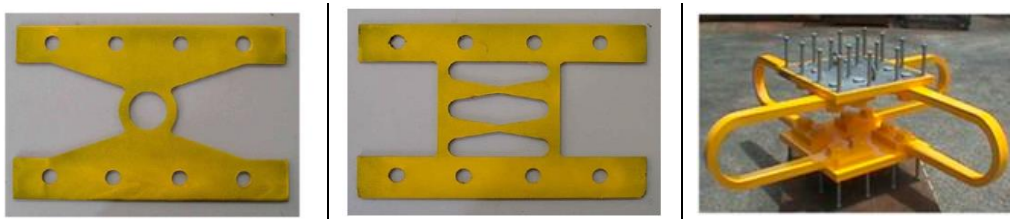
Figure 1.2: Metallic damper examples

Under dynamic loading conditions, metallic dampers undergo plastic deformation, proficiently converting input energy into dissipated energy. This mechanism effectively reduces the transmission of internal forces occurring as a result of

earthquake forces to primary structural elements, thereby protecting them against potential failure. Strategically positioned within structures such as between floors, within bracing systems, or integrated into lateral load-resisting system, metallic dampers proficiently dissipate energy via controlled yielding, thereby reducing structural displacement and accelerations. The utilization of metallic dampers in structural systems offers a dependable and cost-efficient means of enhancing seismic performance, increasing occupant safety, and circumventing extensive structural reparations or reinforcements.

The types of metallic dampers are not defined as clearly as seismic base isolation since the materials used in the dampers, the locations in the structure and behavior under seismic loads differ considerably. Nevertheless, the energy dissipation mechanism for each type is very similar; they dissipate energy by exhibiting extensive post-elastic deformation with a hysteretic behavior under dynamic loading. However, utilization of the seismic forces in terms of the deformation mode of the damper are different from device to device, or structure to structure. For instance, a triangular-shaped metallic damper can be used at the connection of a brace to a column or beam by allowing the device to exhibit shear deformation under lateral load; whereas a U-shaped damper can be used concurrently with a structural bearing system that undergo lateral deformation, thus resulting in deformation in torsional mode.

Friction Dampers

Friction dampers have been developed as another energy dissipation device for the protection of structures from severe deformation demands during a seismic event. As their name implies, the energy dissipation capability of such devices arises from the frictional behavior at a specific surface that is formed between the plates manufactured from, mostly, different materials (Figure 1.3). The most common materials that are used in the friction surfaces of such dampers are metals, such as steel, brass, bronze, or various types of polymers.
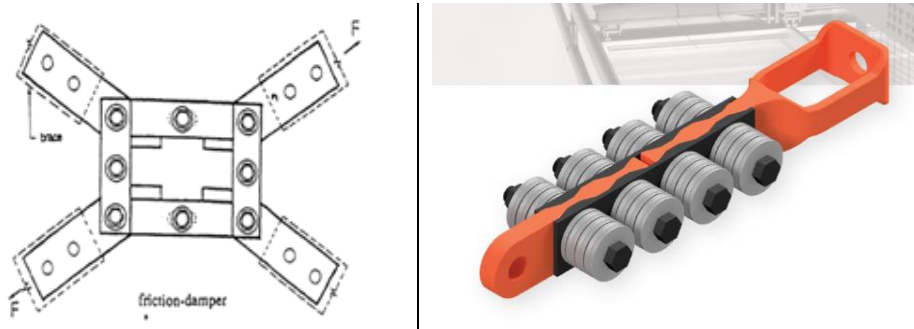
Figure 1.3: Friction damper examples *(taken from Tectonus Inc.)*

During an earthquake, the relative motion between the plates generates frictional forces, converting the input energy into thermal energy. This dissipation mechanism helps dissipate the seismic energy, effectively reducing the vibrations and displacements experienced by the structure. The frictional resistance offered by these devices acts as a supplementary force, working "in parallel" with the primary structural elements to mitigate seismic forces. Friction dampers can be installed at key locations within the structure, such as in bracing systems or between floors, to enhance the overall seismic performance and increase the structure's ability to withstand strong ground motions. Their adoption provides an efficient and reliable approach to minimize structural damage, enhance occupant safety, and improve the overall seismic resilience of buildings and infrastructure.

While the frictional behavior generated by such a damper type adds a considerable energy dissipation capacity to the structure, their contribution depends on several parameters that include some uncertainties. For a friction damper to generate friction force, it shall be compressed by a force normal to the friction surface, which is applied via bolts or spring-type apparatus. Likewise, such externally applied compressive force depends on the application of such external force (fastening, pre-stressing, etc.), not a naturally composed force such as the weight of structure. That condition creates significant uncertainty on the level of the normal force, and eventually the friction coefficient of the device throughout their service life. Another likely disadvantage of such device comes from the uncertainty related with the

durability of materials used in the friction damper. Since the performance of the device depends completely on the properties of the friction surface, any deterioration or change in one or more surfaces comprising the device may hinder the expected energy dissipation performance of the device.

Fluid Viscous Dampers (FVD)

Fluid viscous dampers (FVDs) are another type of dampers designed to reduce the vibration and displacement demand that occur during the earthquake, and add energy dissipation capacity to structures subjected to dynamic loads, such as earthquakes, winds or traffic loads. These dampers consist of a piston that moves within a fluid-filled cylinder. As the structure experiences dynamic forces, the piston moves, forcing the fluid to flow through valves, generating viscous resistance. This resistance converts the kinetic energy of the structure into thermal energy, reducing the amplitude and duration of the vibrations (Figure 1.4).

Figure 1.4: Fluid viscous damper *(taken from Taylor Devices Inc. catalogue)*

FVDs offer several advantages over traditional passive damping systems. They provide highly effective energy dissipation, allowing structures to better withstand dynamic loads and reducing the displacement demand, especially under very high

seismic hazard levels. These dampers can be incorporated into new buildings during construction or retrofitted into existing structures, making them a commonly used solution for enhancing the seismic performance of buildings, bridges, and other infrastructure. Additionally, FVDs can offer adjustable damping characteristics, allowing engineers to tailor their performance to specific design requirements.

While FVDs offer numerous advantages, there are also a few disadvantages to consider. One drawback is the potential for overheating. During severe and long-duration earthquakes, the high energy dissipation in FVDs can lead to a significant heat buildup. If the heat is not adequately dissipated, it can cause the fluid to reach high temperatures, potentially leading to a reduction in damping performance or even damage to the damper itself. Proper design considerations, such as incorporating cooling mechanisms or using heat-resistant materials, are necessary to address this issue.

Another limitation is the complexity of their design, manufacturing, and installation. FVDs require careful engineering and expertise to ensure that they are properly sized, located, and integrated into the structure. The manufacturing of FVDs also require very high-level expertise, precision and quality-control, as compared to other types of dampers; as the life-span of these devices and expected performance during a severe earthquake may be considerably reduced because of leakage, corrosion, etc., if they are not carefully manufactured. As the size and weight of the FVDs are considerably high, their installation often involves significant modifications to the building's structural system, which can be time-consuming and costly.

Buckling-Restrained Braces (BRB)

Buckling restrained braces (BRBs) are another type of external structural protection system that enhances the seismic performance of buildings and structures. Distinctly from other types of energy dissipating devices, BRBs are installed within the frame of a structure to provide resistance against lateral forces, such as those generated

during earthquakes. These braces consist of steel core members surrounded by high-strength steel casing, forming a flexible system (Figure 1.5). The primary function of BRBs is to reduce lateral deflections, interstory drifts and extensive yielding/buckling of structural members under severe earthquakes.

Figure 1.5: Buckling-restrained braces *(taken from Vira Brace Inc.)*

One of the main advantages of BRBs is their high energy dissipation capacity. During an earthquake, the BRBs absorb and dissipate a significant amount of energy by undergoing inelastic deformations. This behavior reduces the overall seismic demand on the structure, preventing potential damage and enhancing its resilience. BRBs are also known for their ductility, which allows them to undergo large deformations without significant loss of strength or stiffness. While BRBs can be used as an additional energy dissipation source in a structure, another area of use is to modify the stiffness and behavior of the superstructure and reduce lateral deformation where the deformation levels exceed certain level, i.e., serviceability limit. This situation is especially significant where the superstructure is more flexible than required for a seismic base isolation application.

As BRBs are one of the widely known structural protection system alternative, especially for design of taller building type structures and also for the retrofit of existing structures, these devices pose some drawbacks in terms of the design,

installation and behavior during a seismic event. One notable drawback is the introduction of additional stiffness and strength to the structure, which can result in higher forces being transmitted to the superstructure during a seismic event. The increased stiffness provided by BRBs alters the dynamic characteristics of the structure, affecting its natural periods, mode shapes, and global damping matrix. This change in stiffness distribution can lead to a redistribution of seismic forces within the system. As a result, certain parts of the superstructure that were originally designed to dissipate energy may experience higher forces than anticipated. The concentration of forces on specific load carrying members can result in localized damage or potential overstressing.

Another disadvantage of BRBs over their alternatives is that the architectural design of the newly designed building and their installation into an existing building may be troublesome when the utilization is highy desired. In order to set the BRBs work as designed during a seismic event, they shall be placed in substantially different places in the superstructure. This may create issues during the architectural design phase, even before the structural design.

Tuned Mass Dampers (TMD)

A tuned mass damper (TMD) is a passive damping device used to reduce the dynamic response of structures subjected to vibrations or oscillations. It is typically applied to tall buildings, bridges, chimneys, and other structures that may be subjected to earthquake vibrations or oscillations resulting from wind.

A TMD schematically consists of a mass, a spring, and a dashpot component. The mass is connected to the structure, usually through a set of cables or rods, and it is free to move in response to the structure's vibrations. The spring provides the restoring force, while the damping element dissipates energy, reducing the amplitude of the structural vibrations (Figure 1.6).

Figure 1.6: Tuned mass damper

The TMD is tuned to the specific natural vibration period of the structure it is installed in. By adjusting the mass and stiffness of the TMD, it is set to vibrate out of phase with the structure's vibrations, effectively counteracting and reducing the motion of the structure. This concept of out-of-phase motion helps mitigate resonance and minimize the transmission of energy to the structure. TMDs are particularly effective in attenuating wind-induced vibrations in tall buildings and cable-supported structures. They can also be used to mitigate vibrations caused by seismic events, reducing the structural response, and enhancing the safety and comfort of occupants and users.

The advantages of TMDs include their simplicity and effectiveness in reducing vibrations. However, it's important to note that TMDs require careful design and tuning to match the specific characteristics of the structure. Additionally, TMDs are typically effective in reducing a specific type of vibration (e.g., wind-induced vibrations at a particular frequency). However, they may not be as effective in attenuating vibrations at different frequencies or caused by other sources. Further disadvantages of TMDs are their heavy mass, hence additional gravity load imposed on the structure, and the large space required for their placement.

Internal Plastic Hinges

Internal plastic hinges can be considered as an integral part of the framing system in contrast to the external energy dissipation devices defined above. Hence, they are "internal". They provide continuity in the frame system through a device implanted into the system, such as a beam-column connection device or a plastic hinge device at the member ends where seismic demands are large (Figure 1.7). These plastic hinges imitate the intentional plastic hinges formed at beam ends in reinforced concrete, precast or steel structures in view of the capacity design principles. Their role is to confine all plastic deformations within themselves, hence leaving the connecting concrete (or steel) members free of damage, i.e., they remain in the linear elastic response range.

A primary target of plastic hinge cells is their removal after a strong earthquake excitation, and replacement with a new one. Although this is an ambitious, if not a pretentious claim for practical implementation, technically it is possible.

<div align="center">(a)   (b)</div>
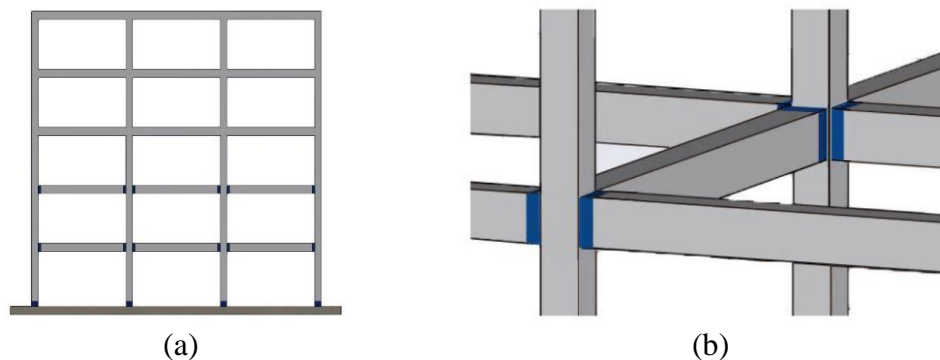
Figure 1.7: (a) Frame with implanted plastic hinges (b) Close-up view of beam-ends

1.2 Review of Past Studies

1.2.1 Seismic Base Isolation

Seismic base isolation is briefly introduced in Section 1.1, by classifying the currently used base isolators into mainly two types: lead rubber (LRB) and high damping rubber bearings, and friction pendulum isolators (FPS). The research on seismic base isolation, which is very briefly summarized with the studies that may be accepted as pioneers, is also contained with those two main types.

The earliest research on lead rubber bearing goes back to 1970s, where the first development and testing of LRB type isolators were presented by Robinson and Tucker (1977) and Skinner et al. (1980). The papers consisted of the design and manufacturing of the first LRB by modifying a laminated rubber bearing by placing a lead core at the middle of the device. At that time, lead material had already been used in the development of hysteretic energy dissipation devices. The first tested device (Figure 1.8) was a square LRB isolator with a displacement demand of 68 mm, and it was followed by the production and test of a cylindrical LRB with a displacement demand of 90 mm. The latter paper also mentioned the development and design works of the first base isolated structure projects, where one of them was William Clayton Building, the first base isolated building in New Zealand, isolated with LRBs.
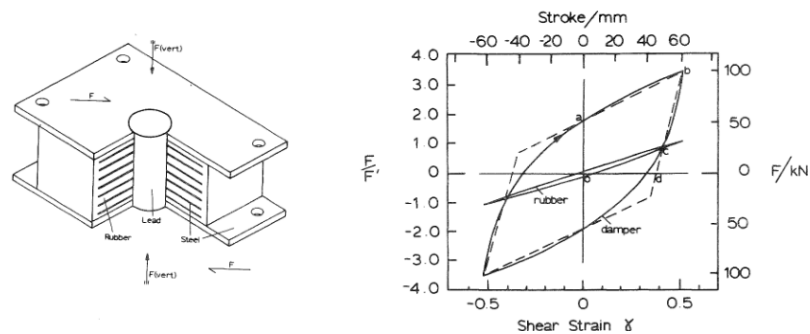
Figure 1.8: Schematic of a LRB and its hysteresis curve (Skinner et al., 1980)

Approximately 10 years after the first development of LRB isolators, friction pendulum isolators were developed in 1980s, with the most prominent studies published by Zayas et al. (1990) and Mokha et al. (1991), which included the introduction of Friction Pendulum System (FPS) (Figure 1.9) by setting forth its theory, component testing, design application to a framing system, and shake-table testing on a scaled base-isolated structure. The former study consisted of the introduction and discussion of theory behind a single-curvature FPS, along with exemplary test results from a set of approximately 150 prototype tests performed under different levels of ground motion simulations, and consequently, a design example.
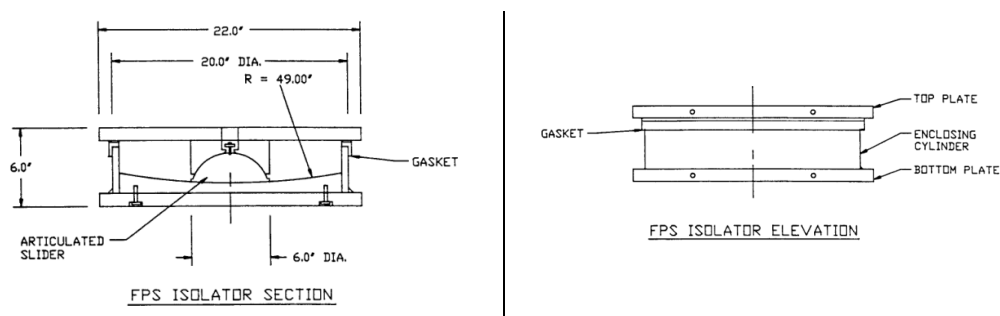
Figure 1.9: Section view and elevation view of an FPS isolator (Zayas et al., 1990)

The study investigated the several aspects of FPS and drew conclusions as follows.

- The transmission of ground motion from the ground to the superstructures with varying fundamental period of vibration were investigated, concluding as the strength of ground acceleration increases, the percentage of acceleration transmitted to the superstructure decreases.
- Base shear forces were investigated in five different structures and compared with non-isolated structures on a response spectrum. It was concluded that the variation of base shear ratio with the type of structure in terms of vibration

16

period was insignificant, and force amplitudes were significantly reduced, especially in the periods smaller than 1.0 sec.

- The behavior of FPS was investigated with different sliding periods and friction coefficients, concluded that increase in sliding period and decrease in friction coefficient resulted in a decrease in base shear and an increase in displacement.

- The restoring stiffness of an FPS depends on the supported weight on it (in other words, vertical force occurring on an isolator) and the radius of curvature. This feature automatically concluded that on the superstructure, the center of stiffness coincided with the center of mass, resulting in the minimization of torsional motions, especially in asymmetric plan structures. This feature was also validated with experiments during the study.

- The sliding period of FPS depends only on the radius of curvature. This feature leads to the design of base isolation system practically independent of the mass of superstructure, with only controlling the radius of curvature of FPS components while determining the sliding behavior of the system.

The latter study, on the other hand, consisted of the shake-table test of a six-story, steel, ¼-scale prototype moment-resisting frame, equipped with FPS. Two types of sliding materials with different friction coefficients were used, and the behavior of isolated structure and FPS components were investigated under a set of seven ground motion records with varying frequency content and peak ground acceleration (PGA). Mainly, base shear ratios, interstory drifts, isolator displacements, peak accelerations, and permanent displacements were determined and investigated.

Despite two different sliding materials used in FPS components during the study, the presented results were obtained from the prototype having the FPS with higher-friction material, since higher acceleration, base shear and interstory drift were expected from higher-friction FPS. The following observations were drawn.

17

- The elastic interstory drift limit of 0.005 was reached for a PGA of 0.1g in an exemplary ground motion record under fixed-base conditions, whereas the same limit under the same record was reached for a PGA approximately 0.6g.

- The peak floor accelerations were effectively reduced under different ground motions, even when the records were scaled two-to-three folds.

- The displacement histories and base shear-displacement hysteresis curves of the entire FPS interface were obtained. The results indicated that the maximum permanent displacement in the interface under the ground motion record set was determined as less than 6% of the isolator design displacement.

The FPS devices that were studied in the literature in 1980s through 2000s were, originally, single curvature type curved surface sliders. Although that originality ensured the desired and envisaged behavior and performance, validated with both component tests and frame-scale tests, single-curvature FPS type had some practical limitations, such as difficulty in production and application mainly because of the geometry. Therefore, research and development continued on the friction pendulum system in search of more efficient, economical, and applicable devices. The most substantial, widely accepted, and applied advancement was on the number of sliding surfaces of a FPS, i.e., Double Curvature FPS (DCFPS) and Triple Curvature FPS (TCFPS). The rationale for increasing the number of sliding surfaces of an FPS is to divide total displacement demand resulting from seismic hazard into two surfaces and by this means reduce the outer dimensions of FPS and achieve a more economical and easy-to-apply alternative.

Although it was conceived in several works and patents dated back long ago, the first studies on the modern Double Curvature FPS (Figure 1.10) were reported in Tsai et al. (2005) and Tsai et al. (2006), where the former study reported the experimental evaluation of theoretical solution method for the response of DCFPS, and latter study issued the component and shake-table tests of DCFPS. The former study mainly focused on the derivation of a piecewise exact solution method for the calculation of

seismic response histories, by dividing the response of a DCFPS into three phases: sliding phase, non-sliding phase, and initiation of the sliding phase. Afterwards, a three-story full-scale steel frame was tested on a shake-table under three different ground motion records, and the response histories were compared with the analytical seismic responses of the same structures. The comparison was made for the isolator displacement, velocity, and acceleration. It was concluded that the results were in good agreement, with the deviation being the most in accelerations and the least in the displacements.

Tsai et al. (2006), which was the companion study of Tsai et al. (2005), included the PTFE sliding material component tests and full-scale DCFPS component tests, besides the shake-table tests and numerical comparisons that was mostly the subject of former study, but similar results were also presented in this study. The sliding material component tests established the relation between contact pressure, friction coefficient and sliding velocity under sliding material component tests with severe displacement reversals, while full-scale DCFPS component tests determined the behavior, force-displacement relationship, and durability of a full-scale DCFPS under reversed cyclic loading. One of the main conclusions that was come was that the friction coefficient of the sliding material had an inversely nonlinear proportion with the contact pressure, and friction coefficient approached a constant value after sliding velocity exceeded a certain value. The main conclusion drawn from full-scale component tests was that FPS component had a good durability after 248 cycles, with retaining restoring force at the last cycles within 93% of that of first cycle. Shake-table tests, on the other hand, indicated the result that the floor accelerations at the superstructure were reduced between 70-90% of the acceleration obtained for fixed-base counterpart, under different ground motion records.
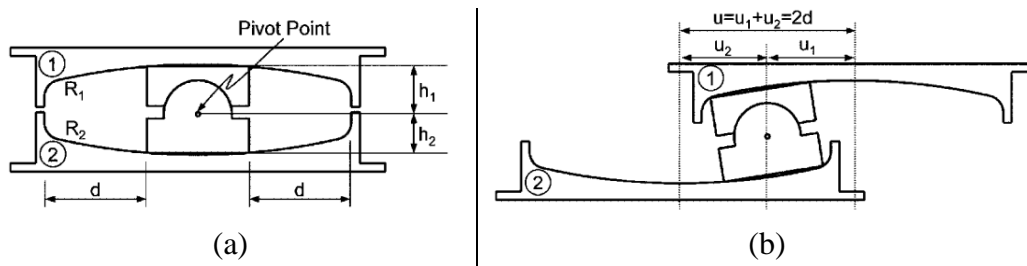
Figure 1.10: Schematic view of a DCFPS (a) at rest (b) at maximum displacement
(Fenz & Constantinou, 2006)

While the studies discussed above considered that two surfaces of double curvature FPS had the same radii of curvature and friction coefficient values, therefore exhibiting the same sliding behavior on two identical surfaces and offering the advantage of dividing the total displacement equally into two surfaces. Fenz and Constantinou (2006, 2008), on the other hand, discussed the double curvature FPS in a more general manner, developing theoretical relationships for FPS devices with different radii of curvature and friction coefficient values in the two surfaces, and testing DCFPS components with surfaces with different curvature and friction coefficient values (Figure 1.10). In this way a more adaptive behavior, for instance, in terms of displacement and acceleration demand under different levels of earthquake, would be achieved for practical use.

More recently Fenz and Constantinou (2008a, 2008b) studied the adaptive behavior of FPS in a more different manner in their companion papers, in which the theoretical background and experimental verification of a triple curvature friction pendulum system were proposed, by naming the device as Triple Friction Pendulum Bearing (TFPB). The former study also issued theoretical work on single curvature and double curvature FPS with variable curvature and friction coefficient. Nevertheless, the "adaptiveness" of the TFPB came from the adaptability of its stiffness and damping in accordance with the displacement level of the bearing. In practice, seismic base isolation systems are practically designed according to a single displacement demand, which is obtained for the maximum expected earthquake

hazard, and because there is one homogeneous sliding surface or multiple surfaces with the same mechanical properties, the main parameters that affect the performance of the system such as dynamic (or sliding) stiffness do not change with respect to earthquake levels. However, TFPB offered multiple surfaces with different geometrical and/or mechanical properties, such as radius of curvature, friction coefficient, in search of achieving different behavior under different levels of earthquake. Figure 1.11a shows the schematic of a TFPB that has practically two double curvature friction pendulums placed inside each other, where the surfaces of both inner device and outer device theoretically had different curvature and friction coefficient. The force-displacement response of such a device can be investigated in Figure 1.11b.

The accompanying study, on the other hand, validated the theoretical background of the adaptive behavior of FPS devices by performing component tests on TFPB, as well as adaptive FPS and DCFPS devices. The three different TFPB devices that were tested during the study had equal lubricated surface conditions at inner pendulum and unequal dry surface conditions at outer pendulum, whereas the curvature was different for inner and outer pendulums but symmetrical for each pendulum, for the sake of simplicity.

(a)   (b)
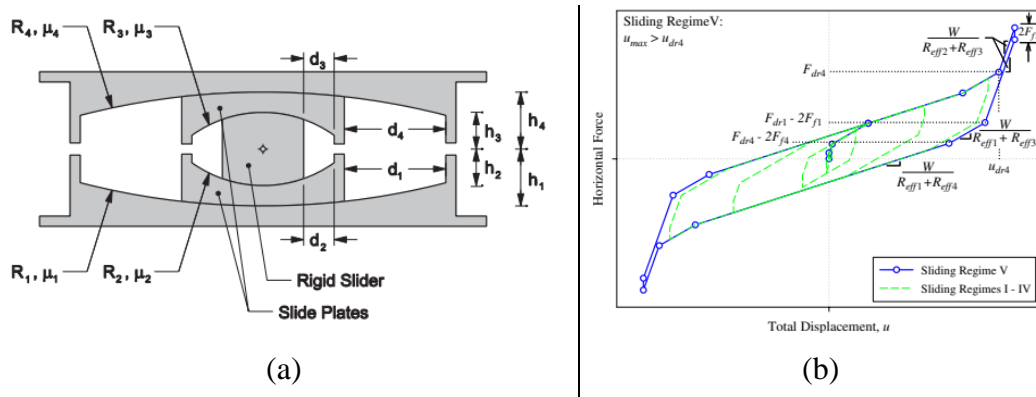
Figure 1.11: (a) Schematic of TFPB (b) Force-displacement hysteresis of TFPB (Fenz & Constantinou, 2008)

1.2.2   Fluid Viscous Dampers (FVD)

A typical fluid viscous damper (FVD) is schematically shown in Figure 1.12. Although the technology has long been used in several industries i.e., aerospace, naval, automotive, defense, and machinery, it has started to be utilized in structural earthquake engineering as a passive and external energy-dissipating device in the 1990s. In parallel, research and development on the testing and optimization of the device for the protection of buildings against earthquakes were carried out on several research projects (Reinhorn et al. 1995, Symons & Constantinou 1998). Lee and Taylor (2001), as the most prominent developer and supplier of FVD in construction sector, presented the main characteristics of FVD devices and its future trends in earthquake engineering, by introducing the device, identifying the critical parameters effecting its performance during an earthquake, and exemplary installation techniques to a framing system.
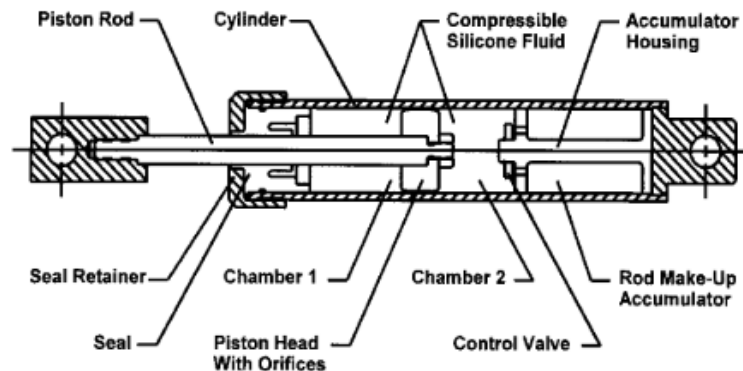
Figure 1.12: Typical fluid viscous damper (Lee and Taylor, 2001)

As presented in the cited paper, the most prominent parameter of an FVD is the damping exponent, which practically varies between 0.3 and 1.0. When the coefficient equals 1.0, FVD behaves linearly, i.e., the velocity during an earthquake and developed force changes linearly, and damping forces are completely out of

phase with the structural forces; whereas a coefficient of 0.3 corresponds to the lowest damping possible, where damping forces tend to superimpose on the structural forces. In that relation, it would be more advantageous for FVD to work in the linear range as much as possible.

It was also presented that FVD devices may be placed in different regions of a structure and with various external structural elements, such as in a diagonal direction at the end of a diagonal brace, horizontally at the top of a chevron brace, or horizontally between adjacent structures. They may also be incorporated with the seismic base isolation system at the base isolation floor.

Whereas a FVD is regarded as a reliable source of external energy dissipation when properly incorporated into the structural design, several inherent features of it may reduce the working life of a FVD or cause failure of the device. One leading issue is related to the temperature rise, as mentioned in Section 1.1, and its effect on the components of FVD. Makris (1998) and Makris et al. (1998) studied the heating problem in two companion papers, where the viscous heating was investigated for both small amplitude and large amplitude motions. While functioning, an FVD moves with a high velocity and fluid inside also flows with a high velocity at the piston head. This has the potential for causing heat induced damage in the damper seals.

1.2.3   Buckling-Restrained Braces (BRB)

Research and development studies of buckling-restrained braces (BRB) started in 1970s with Kimura et al. (1976) as a brace-type external energy dissipating device but without any restraining against buckling. In their research, a brace that was encased in an outer tube filled with mortar was developed and experimental studies were conducted. However, it was reported that due to lack of a stable confinement, the device did not exhibit a consistent behavior under cyclic loading since compressive forces caused the filling mortar to break and create voids inside the

tubes and weaken the brace against further cyclic loading. In the following years, several research including Mochizuki et al. (1980) and Wada et al. (1989) in Japan studied similar device types. In 2000s, the most widely referenced study on BRBs was conducted by Black et al. (2004), which included component testing, evaluation, and characterization under seismic loading, particularly of BRB types that are named as Unbonded Braces (Figure 1.13).

The study was conducted with the aim of verifying the theoretical predictions of the stability of BRBs, determining the inelastic capacity of BRBs, and proposing a hysteretic model for the force-displacement relation. It was, in summary, concluded that the unbonded braces as BRB exhibit a more reliable and practical alternative to conventional braces of a framing system. Also, it was concluded that the primary failure mode was the plastic buckling of the inner core, as may be expected from a BRB type device. Nevertheless, BRBs with the configuration presented herein as Unbonded Brace had several shortcomings such as low-cycle fatigue, geometrical imperfections, and inconsistent material behavior. Subsequent research in buckling-restraint braces aimed to reduce those shortcomings. For instance, Zhao et al. (2011) developed the Angle Buckling-Restraint Brace (ABRB), which was a modification of conventional BRB, created by rotating the outer core about its longitudinal axis and by welding several stiffeners throughout its length (Figure 1.14a). Hao et al. (2014) studied a steel unbuckling brace (SUB) with H-section core and cross-shaped end connectors (Figure 1.14b).
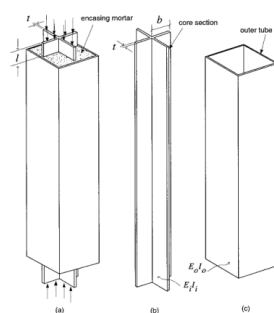
Figure 1.13: Sketches of an unbonded brace (Black et al., 2004)
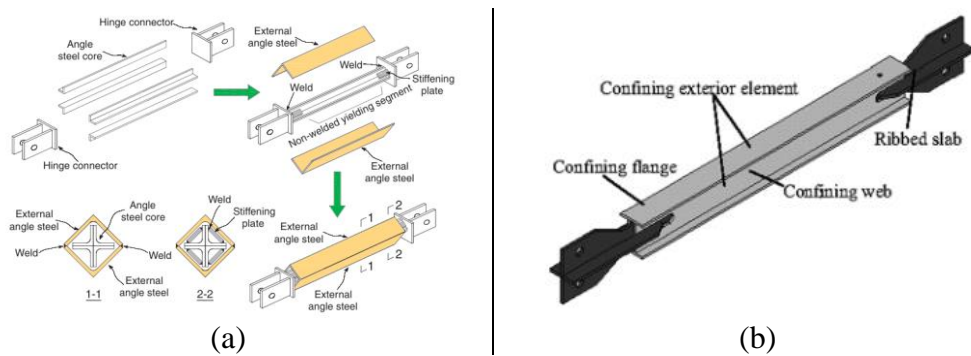
Figure 1.14: (a) ABRB (Zhao et al., 2011) (b) SUB (Hao et al, 2014)

1.2.4 Friction Dampers

The earliest studies on the development of friction dampers go back to the 1980s, while Pall et al. (1980, 1982) presented the first development steps. The very first research, and the former of the two papers, included a Limited Slip Bolted Joint (LSB) type developed for the use in large precast panel structures, where the ductility existing in conventional moment-frame structures is absent due to limited lateral continuity in structural members. The rationale for developing such a device for the joints of large panel structures was the concentrated damage specifically at the joint locations due to slipping along those planes, while panels themselves essentially remain elastic. The LSB device was comprised of an insert, which creates a recess for connecting angles, and bolts that were used to create friction force by applying pre-stressing; while different sliding surfaces between the insert and connecting angles were examined in the study such as milled, sandblasted, painted, and covered with brake pads. The most stable behavior was obtained where in-brake pad and milled surface mating was applied. Using obtained hysteresis curves and related parameters, an analytical study on 5, 10, 15 and 20 story structures was also conducted and forces and drift ratios at the structural models were investigated.

The latter study on the other hand, was conducted on a modified sliding friction device compared with the LSB device, with the aim of applying it on framed

buildings with the help of bracing systems. The proposed friction device was very similar to the one developed in the former study, but this time they were placed at either at the intersection of two braces at a specific span, named as X-bracing (Figure 1.15a), or at the top ends of chevron braces, named as K-bracing (Figure 1.15b). As seen in the associated figures, when the bracing was formed as X-, lateral motion of braces would activate the device with outward motion in the tensioned brace, and inward motion in the compressed brace. In the case of K-bracing, lateral motion would lead the chevron bracing to move in the lateral direction while activating the device in the direction of motion. In both cases, the sliding of friction pad on the milled steel surface, and the pre-stressing force on the clamping bolts together would create stiffness and energy dissipation capability to the framed structure, leading a concept named as Pall Friction Damper (PFD) in literature.

(a)

(b)
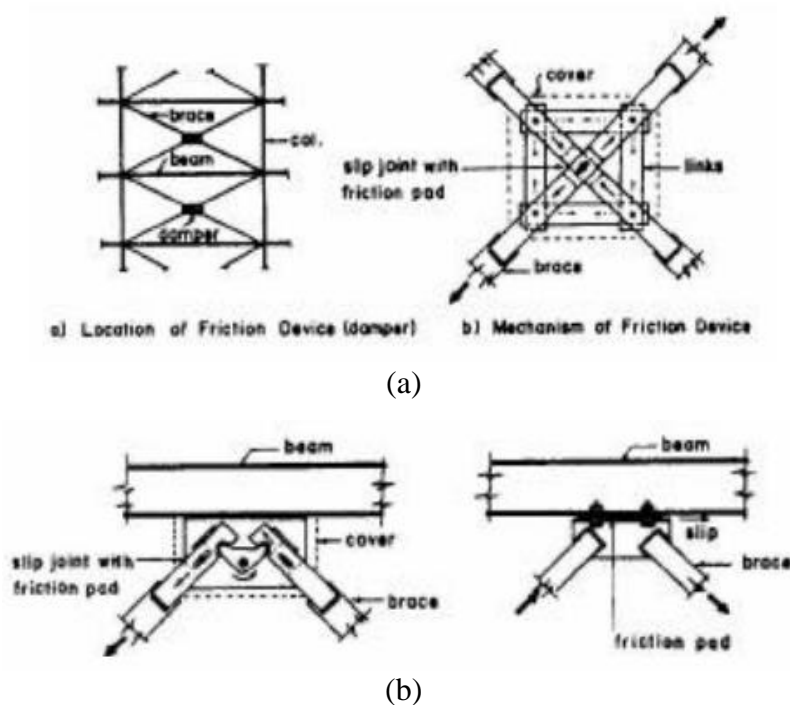
Figure 1.15: Friction damped braced frames. (a) X-brace (b) K-brace (Pall et al., 1982)

While the logic of creating a frictional surface with appropriate sliding interface and stressing force normal to the interface established in the literature as the backbone of friction dampers, Wu et al. (2005) proposed an improvement directly on the original PFD device and named it as Improved Pall Friction Damper (IPFD) (Figure 1.16). As can be seen in the figure, the cross-shaped plate in the device was replaced with a T-shaped plate (labeled as 1) and sliding was collected to a single region (labeled as 5). The results of the study showed that the friction forces were identical under the same damper forces and displacements, and IPFD was successful in replicating PFD in terms of mechanical properties. On the other hand, experimental work on IPFD concluded a cheaper, easy-to-manufacture and easy-to-be-modeled device as compared to PFD. Besides, the study also captured that vertical motion on the original PFD caused significant increase in tensile forces on the connecting braces, which IPFD eliminated with sliding only in the lateral direction.
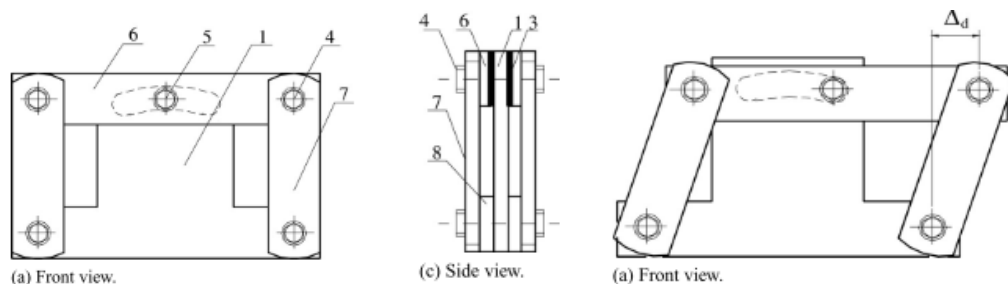
Figure 1.16: Improved Pall Friction Damper (Wu et al., 2005)

Fitzgerald et al. (1989) and Grigorian et al. (1993) utilized the concept of creating a sliding interface with adequate mating materials and leading it to develop friction force and deformation by clamping the materials with pre-stressed bolts and developed two similar friction damper devices to be used at the ends of concentrically placed braces in framing systems. Both research presented similar devices in terms of their designated places in a system and formation of friction forces, even with the same naming; Slotted Bolted Connection (SBC). The

configurations of the developed devices are given in Figure 1.17. It could be seen in the figure that there is one major difference between the two devices almost identical in terms of working mechanisms; the former device composed only of mild steel whereas the latter device incorporated brass plates at the sliding interfaces.

(a)

(b)
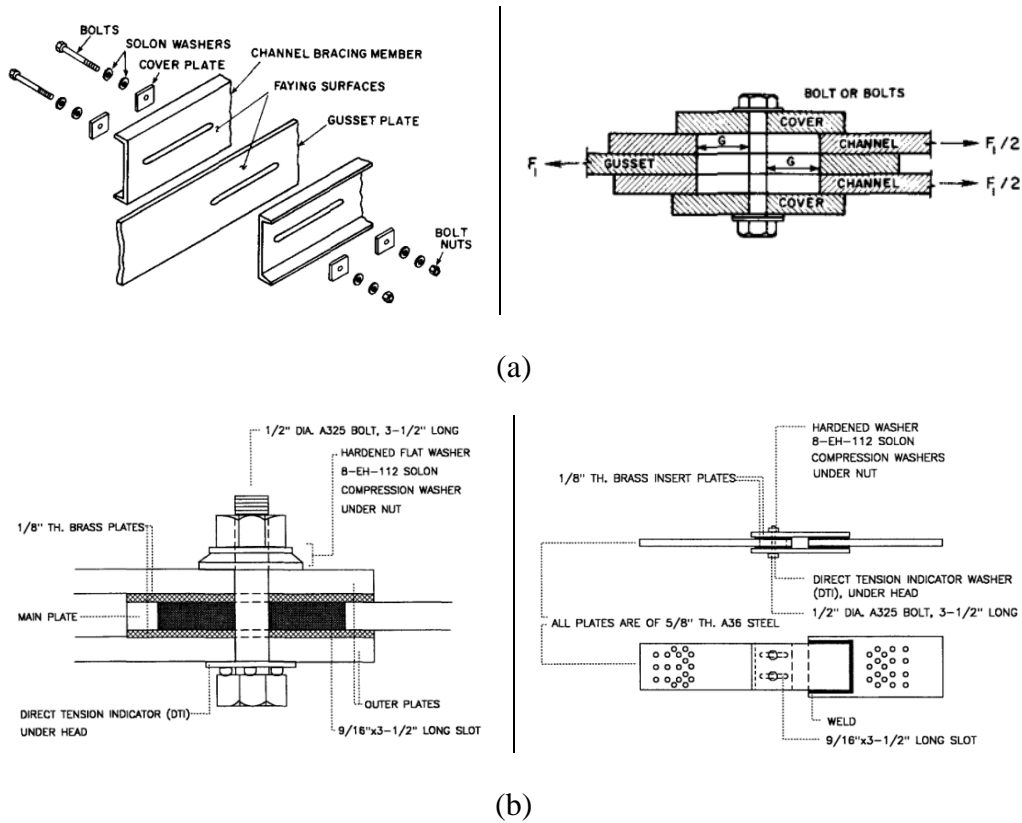
Figure 1.17: Slotted Bolted Connection (SBC) proposed by (a) Fitzgerald et al. (1989), (b) Grigorian et al. (1993)

The development of these devices was based on the observations that PFD type had relatively low load resistance capacity, and demanding manufacturing and installation processes. Owing to these shortcomings, it was aimed at developing a simpler device with the same working mechanism. Other improvements of SBC devices were the usage of Belleville springs to better adjust the frictional force, and alignment of braces to be axially symmetrical, essentially eliminating the eccentric

moments. However, further studies such as Lukkunaprasit et al. (2004) analytically found that pre-stressing bolts exhibited loss of friction force up to 50% and proposed the use of restrainers on SBC devices.

1.2.5   Metallic–Yielding Hysteretic Devices

The concept of using external energy dissipation devices as a technology for structural protection against earthquake effects is first discussed by Kelly et al. (1972) and Skinner et al. (1974). In their conceptual and experimental research, they first identified the problem regarding energy dissipation through the deformation of the structural members during a seismic event as a reliability issue for the earthquake resistance of structures. Then the concept of increasing the energy dissipation capacity of structures and separating the primary dissipation mechanism from load-carrying members is introduced by defining three different mechanisms of deformation of an external energy dissipating device; mainly, rolling/bending of U-shaped strips, torsion of rectangular/circular bars, and flexure of thick beams, labeled respectively as Type A, B and C. The main designated locations of the devices are between flexibility-based shear walls for Type A, foundations for Type B, and diagonal braces in frames for Type C.

During their study, force-deformation relationships, energy dissipation capacity, and fatigue resistance of the devices were investigated. All types were tested for their deformation mechanisms. It was concluded that the damper device Type B, where the deformation and energy dissipation mechanism is torsion of the rectangular bars, is more efficient in energy dissipation capacity and fatigue resistance, i.e., withstanding more cycles before a significant drop in force capacity. Though, Type C devices that dissipate energy in the form of flexural deformation have advantages in the installation and replacement after a seismic event.

Skinner et al. (1980) further updated and summarized the ongoing research on the steel hysteretic devices, lead hysteretic dampers and PTFE sliding bearings by

expanding the research on the structural protection against earthquakes to base isolation area by using lead material as an energy dissipater and PTFE material as a sliding material. Considering the content of this section, only the steel hysteretic dampers part was covered. The research included the development of the following device types, which are presented in Figure 1.18 for convenience; (1) torsion beam device, (2) round steel cantilever, (3) taper plate cantilever, (4) round bar, and (5) flexural beam damper (Figure 1.18). Torsion beam device (1), among them, was the first developed device, which was designed to deform under torsional force applied via a loading arm at the mid span of a fixed-end beam. The objective was to create overstraining of short beam sections in torsion and bending. Round steel cantilever (2) was developed to be used as an additional source of damping at the base isolation interface in a building. As such, it was aimed for the device to yield and deform with its whole length under relative lateral movement between upper and lower ends of the device. Taper plate cantilever (3) was developed as an alternative to torsion beam device considering it would be a better alternative especially if there was enough space to utilize the cantilever arm for larger movements and deformations. Round bar (4) was developed inspired by the energy dissipation behavior of reinforcing bars inside a reinforced concrete member when deforming after concrete spalling during the flexural behavior. However, unlike reinforcing bars, those round bars were designed as bent or looped along their length, in order to prevent premature fracture under tensile forces. The last device type, flexural beam damper (5) was designed to be comprised of a circular-section main beam and two cranked arms fixed at the ends of the beam, which would exhibit the designated flexural behavior during lateral movement of free ends of cranked arms.

The paper also discussed the aging behavior of all steel damper types apart from its geometry, behavior and working mechanism, and it concluded that the aging of dampers did not create any significant issue. Therefore, the replaceability of such devices because of any effect for aging was not discussed further.
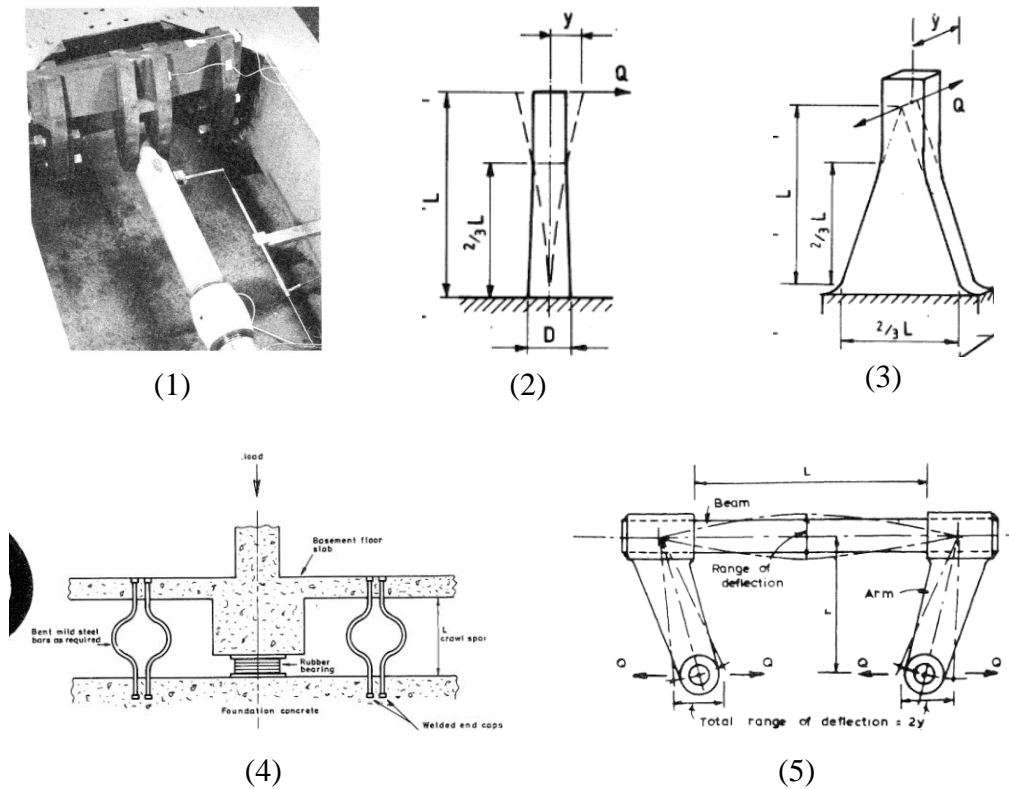
Figure 1.18: Steel hysteretic dampers, which are introduced in Skinner et al. (1980). (1) Torsion beam device, (2) Round steel cantilever, (3) Taper plate cantilever, (4) Round bar, (5) Flexural beam damper.

The introduction of external energy dissipation devices to ductile moment-resisting frames where dissipation demand occurs significantly via the deformation of structural members was followed by the research studies conducted by Whittaker et al. (1991) and Tsai et al. (1993), respectively. Those studies comprised the first development and testing of metallic-yielding dampers by naming such devices as Added Damping and Added Stiffness (ADAS) and Triangular ADAS (TADAS), as commonly known in the literature. While the common rationale for developing ADAS devices was to increase the energy dissipation capacity, strength, and stiffness of a moment-resisting frame; the studies were conducted on a X-shape ADAS in the former research and on a triangular shape ADAS in the latter research. As can be inferred from the selection of device shape as a preliminary evaluation, expected

deformation of such a device is of primary importance considering its energy dissipation. Whittaker et al. (1991) discussed possible alternatives of ADAS shapes between rectangular, triangular, and X-shaped plates in terms of their bending under lateral movements and resulting deformations and stress distributions. The summary of discussion is given in Figure 1.19.
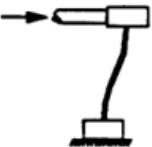
Figure 1.19: Alternatives of steel plate shapes in an ADAS device (Whittaker et al., 1991)

Both studies utilized ASTM A36 class steel to produce ADAS devices, which have minimum yield and ultimate strengths of 250 MPa and 400 MPa, respectively. Both studies performed component and MRF-scale tests during the research, by creating components with multiple ADAS plates and placing the device at the ends of chevron braces of the MRFs. Simple demonstrations of the devices are given in Figure 1.20.
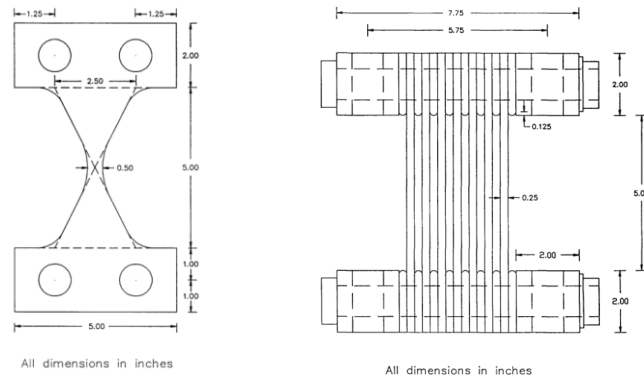
(a)
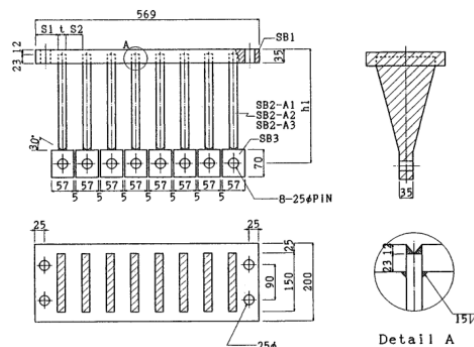
(b)

Figure 1.20: (a) X-shaped ADAS (Whittaker et al, 1991) (b) Triangular ADAS
(Tsai et al., 1993)

It was concluded in both studies that ADAS devices are simple and efficient devices
in terms of the predictability of elastic stiffnesses and ultimate strength, as well as
general stability of hysteresis relationship. During the component tests, a large
number of reversals were achieved without any significant loss of strength or
stiffness. Also, it was determined that the hysteretic behavior at design earthquake
levels depends on mechanical properties such as the yield strength and yield
displacement, and the degree of end-fixities of the devices. Deformation modes of
the devices were also observed as expected. It was also concluded from MRF-scale
tests that ADAS devices increased the global stiffness by 150% and significantly
increased the ability to dissipate energy at less than or equal to interstory drift ratio
of 1.5%.

Li and Li (2007) conducted research on ADAS type devices, of which the initiating development is summarized above, by introducing two different device geometries for the same purpose. That same purpose of providing additional stiffness and energy dissipation capability led the researchers to name the device in the study as "dual function metallic damper (DFMD)" by referring to those two functions. During the study quasi-static testing of dual function devices (Figure 1.21) and shake-table test of a two-story, relatively small-scale steel frame with the devices placed with chevron-braces were performed with four different scaled ground motions to estimate the effects of dampers on the seismic behavior of the structure in terms of displacement response and energy dissipation ratios.

Shake table tests were performed by implementing three different stages to investigate the behavior of DFMDs during yielding, large deformation, and failure. The yielding stage was achieved with ground motions scaled with a PGA between 0.37g and 1.04g, whereas large deformation stage was achieved with a PGA between 1.0g and 2.0g, under different ground motion records and DFMD types. As a result of a series of shake table tests, it was revealed that the first and second story displacements, where DFMDs were placed, were reduced by 90% and 70% on average, respectively. The results in terms of energy dissipation indicated that DFMD devices dissipated an amount of energy between 42% and 87% of total seismic energy.
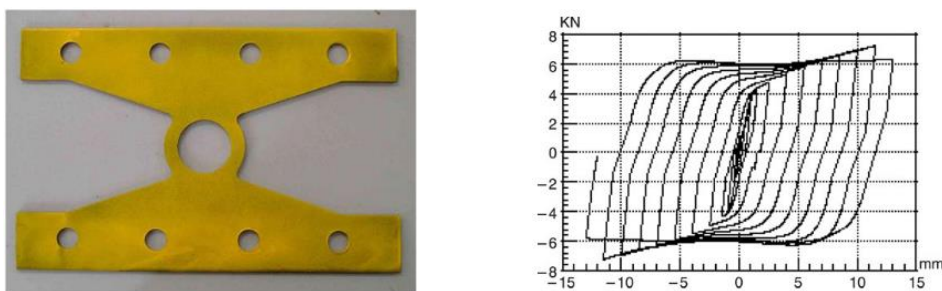
(a) Single round-hole metallic damper

Figure 1.21: Geometry and hysteretic behavior of dual function dampers (Li and Li, 2007)
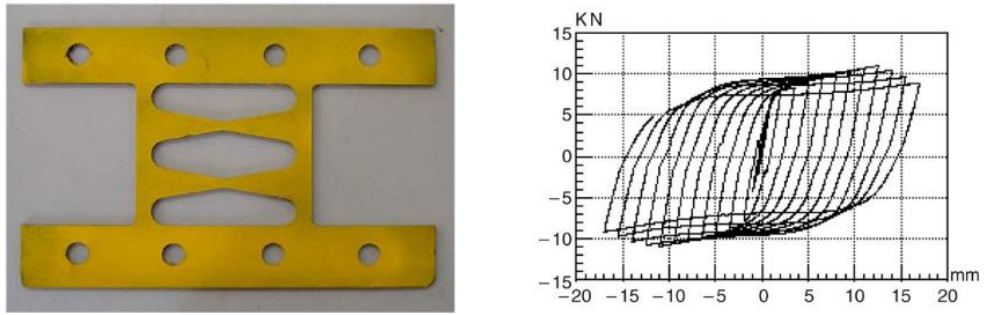
(b) Double X-shaped metallic damper

Figure 1.21 (cont'd)

FUSEIS system is another type of external energy dissipation system that utilizes metallic-yielding dampers in moment-resisting frames (MRF), which was studied experimentally and analytically in Dimakogianni et al. (2012). A FUSEIS is fundamentally an external seismic-resistant steel frame that resembles a shear wall, which is placed at the external spans of a space MRF systems, consisting of two continuous strong columns throughout the structure height and varying number of relatively weak energy-dissipating beams connecting the columns. Whereas the main source of energy dissipation by deformation is contained in a FUSEIS to protect the main structure, the deforming members in a specific FUSEIS are beams. Essentially, the entire FUSEIS research consisted of two main sub-types of FUSEIS systems: FUSEIS1-1, where the strong columns are rigidly connected to continuous beams, and FUSEIS1-2, where the connecting beams are separated at the mid-span and energy-dissipating steel pins are placed to further contain the inelastic response to those pins, which would act essentially as metallic damper. This section introduces and summarizes the findings on the research done on FUSE1-2 (Figure 1.22).
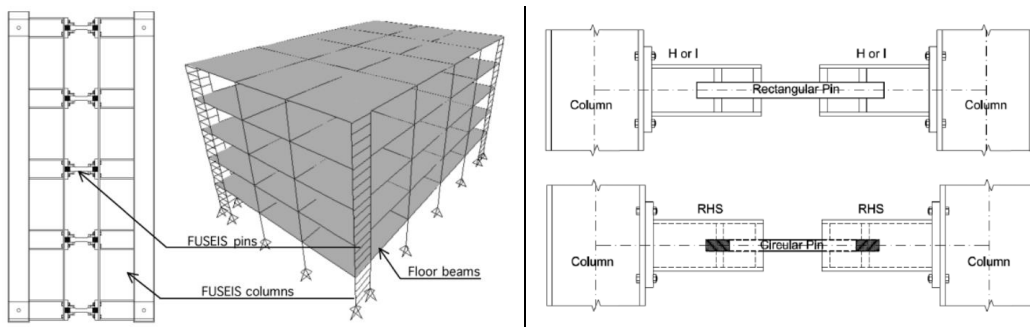
Figure 1.22: FUSEIS1-2 system and its configuration in a building (Dimakogianni et al.2015)

During the study, two full-scale tests on the frames with FUSEIS1-2 were performed in the following two ways: (1) pins with the same cross-sections and different lengths, (2) pins with the same length and different cross-sections. Low-grade S235 steel was used in the production of the pins, and the loading procedure was displacement controlled reversed cyclic with increasing inter-story drift ratio up to 5% with main increments of 0.5%.

The following results and observations were come up with:

- FUSEIS1-2 system may offer an alternative solution to multi-story steel buildings with considerable ductility and architectural easements, compared to a BRB or an ADAS device placed by using chevron braces. Ease in installation and removal may be mentioned as another feature.

- Inelastic deformations were concentrated to steel pins in the FUSEIS system, as desired.

- The ductility factor, which is one of the factors that estimates the behavior factor in Eurocode 8, was determined as an average of 5.4 in the two experiments.

- The replacement of steel pins after the tests were completed was also recorded and reported to be around 60 minutes.

Zhang et al. (2020) contributed to the literature by developing a novel curved steel plate metallic damper (CSPD), with theoretical analysis of the device that sets out the design parameters, followed by experimental work on four sets of component specimens. The proposed curved metallic damper was based on the principles of the U-shaped damper and offers improvement over its shortcomings related with yield strength levels, stress concentrations. The mechanical characteristics and energy dissipation capacity of CSPD, of which scheme and photo are presented in Figure 1.23, were investigated through experimental study.

1-Connecting plate, 2-inverted T-splint,
3-T-base, 4-the damper, 5-bolts
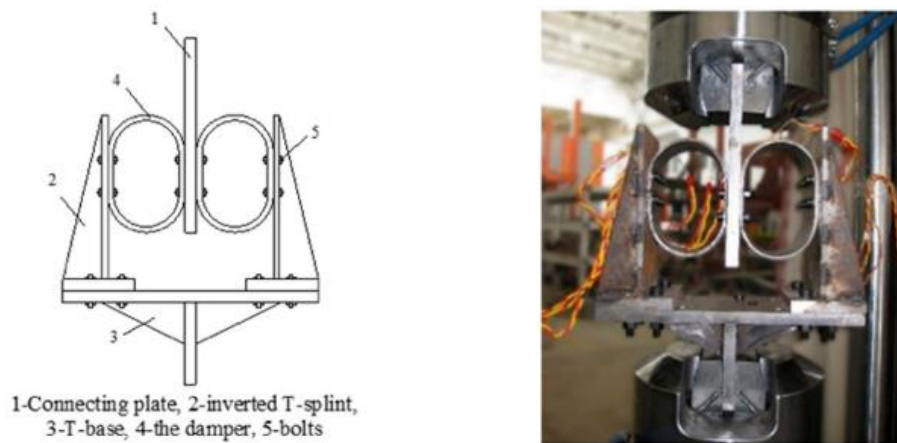
Figure 1.23: Curved steel plate damper (Zhang et al., 2020)

The tested four specimens were produced with S235 low-strength steel with an average yield strength of 246 MPa, and elongation of 35%. Specimens were designed and tested with varying geometrical properties such as plate thickness, width and/or radius of curvature. Testing protocol was prepared and applied as displacement controlled with incremental displacement that was determined according to the theoretical yield displacement of each specimen. That is, each specimen was loaded up to 10 times yield displacement in standard loading procedure. It was basically concluded from the tests that the CSPD specimens exhibited stable hysteresis throughout the standard loading procedure, which was applied up to 10 times yield

displacement (Figure 1.24). It should be noted that the tests were not continued until the failure.
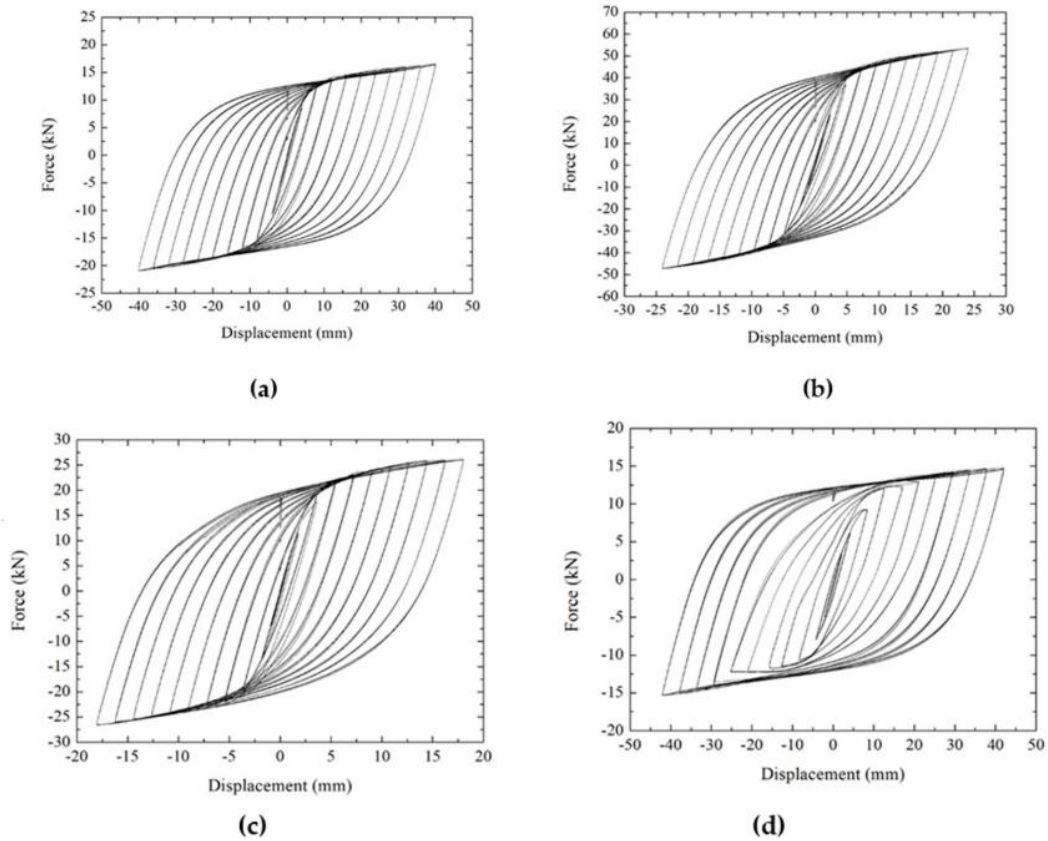
Figure 1.24: Hysteresis curves of four specimens under standard loading (Zhang et al., 2020)

1.2.6 Beam-Column Connection Devices

One of the earliest research programs on the introduction of connection devices in the form of plastic hinge cells to structures for improving their seismic performance was carried out in Nakaki et al. (1994) and Englekirk (1995). Their research was specifically conducted on precast concrete structures, where the ductility required during a high seismic event is limited because of the discrete nature of the system. The former paper introduced the concept of a frame with plastic hinge connectors,

named Ductile Precast Concrete Frame (DPCF) that was designed with Ductile Connectors (DC) between the ends of beams and column faces; and test results of such connection by comparing a monolithic reinforced concrete connection. The latter paper focused on the introduction and design considerations of Ductile Connector (DC) devices in detail.

A DC was basically comprised of ductile rods manufactured from a high ductility steel with a well-defined yield strength, high-strength bolts and washers, and connector plates. Ductile rods that were threaded for the bolts to be fastened during the assembly were first cast in concrete column during production, whereas connector plates are placed at the ends of beams, fixed to their own reinforcement bars (Thread bar). Then, during the erection of precast frame, beams were connected to the columns via fastening of the high-strength bolts. The detail of a DC formation and introduction of hardware are presented in Figure 1.25.

The main working mechanism of a DC was that during a seismic event, the bending moment demand occurred at the beam ends would be converted into a force couple on the ductile rods placed inside columns. In other words, all the ductility demand would be compensated for the deformation of the ductile rods. Also, concrete column itself would resist the compressive and tensile forces that would occur on the ductile rod with its bearing capacity. Shear force demand that would develop as a result of both the self-weight of the structure and seismic action, on the other hand, would be accommodated entirely by the ductile rods and the friction at the connector plate interface. Regarding the system capacity and the definition of strength limit states, load transfer and equilibrium conditions resulting from the working mechanism of DC was considered. That is to say, the most important element of the DC was the ductile rod, which would be the only yielding element during a seismic event. Design values of a DC was utilized to determine the configuration of ductile rods, whereas the material of the ductile rod was selected as a low-carbon, high-ductility structural steel, having a nominal yield strength of 414 MPa (60 ksi) and an elongation capacity of $25\varepsilon_y$. The nominal yield strength of selected bolts was 614 MPa, corresponding to Class 8.8 bolts, implying an overstrength around 1.5.

39
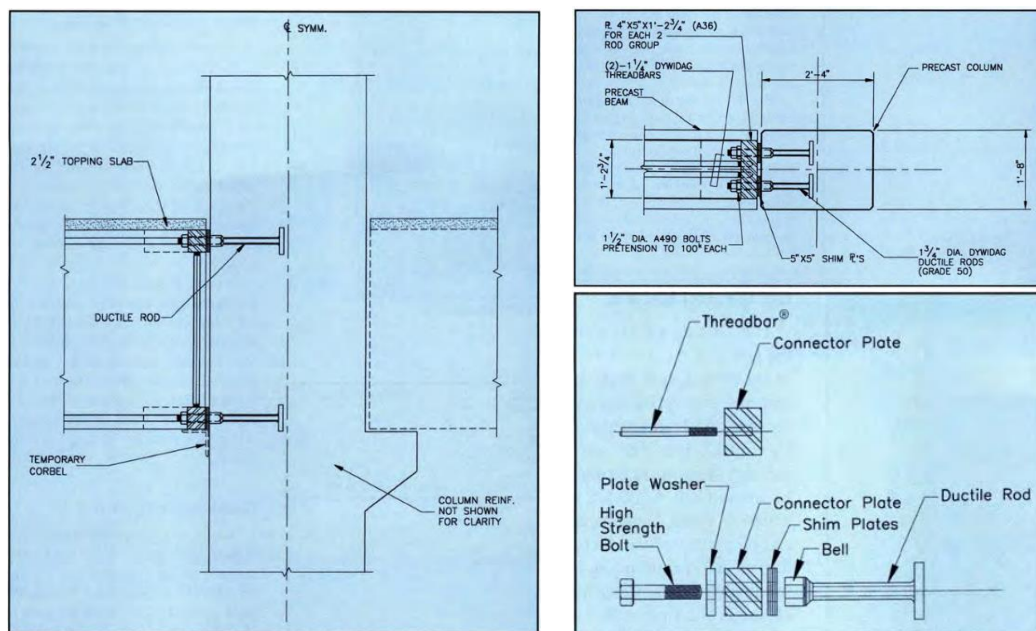
Figure 1.25: Ductile Connector (DC) elevation and plan details, and hardware details (Nakaki et al. (1994))

The designed DC connection was tested under reversed cyclic loading applied with incremental drift ratios with 0.5% increments up to 4.5%, with the aim to determine the limit state for progressive force deterioration. The results were then compared with the test results obtained under a conventional reinforced concrete connection. It was evaluated that DC did not exhibit any force deterioration during the test. However, considering the ultimate strain of the ductile rod and the connection geometry, the plastic rotation capacity of the connection was around 0.035 rad.

The ductile connection (DC) system that was proposed and studied in Nakaki et al. (1994) and Englekirk (1995) had one major drawback inherently; the ductile rods that bring ductility and plastic hinging behavior in the structural system were placed inside precast concrete columns. This condition made the ductile connection practically irreplaceable after a seismic event that would lead it work and protect the building as designated. Essentially, such plastic hinging devices must be replaceable after an earthquake, since the phenomenon is to achieve a structure that remains in the elastic range.

Shen et al. (2011) was one of the first developers of the nonlinear replaceable link concept that would be used in structures as a plastic hinge connection device. In their research, they utilized steel moment-resisting frames as the application stage for the developed replaceable link. As it was stated in the paper, nonlinear replaceable link concept is an advanced state to reduced beam section (BRS) connection, where specific portions of the beam were detailed to force plastic hinge formation away from welded or bolted beam-column connection interface, but in turn did not have any replaceability option.

In their research, two main replaceable link concepts were introduced, different mainly in their bolt configurations to adjacent structural members. They were named as (1) bolted web link with bolted web connection, and (2) W-section link with end-plate connection (i.e., end-plate link). Production and assembly details are given in Figure 1.26. Following the design and analysis of a five-story prototype steel building, four full-scale subassemblages representing first story beam-column connections were tested under reversed cyclic loading, to determine the strength and ductility responses of replaceable links. 3D FEMs were subsequently developed to capture the observed experimental results. Both replaceable link types were designed and manufactured by using rolled steel sections, having a yield strength for Type-1 as 350 and 370 MPa and for Type-2 as 390 and 442 MPa. The loading protocol specified in AISC was utilized, and a story drift of 0.04 rad without fracture and a strength degradation less than %20 of peak load was determined as acceptance criteria. Test results presented in the paper are given as hysteretic responses in Figure 1.27 and as damage details in Figure 1.28.
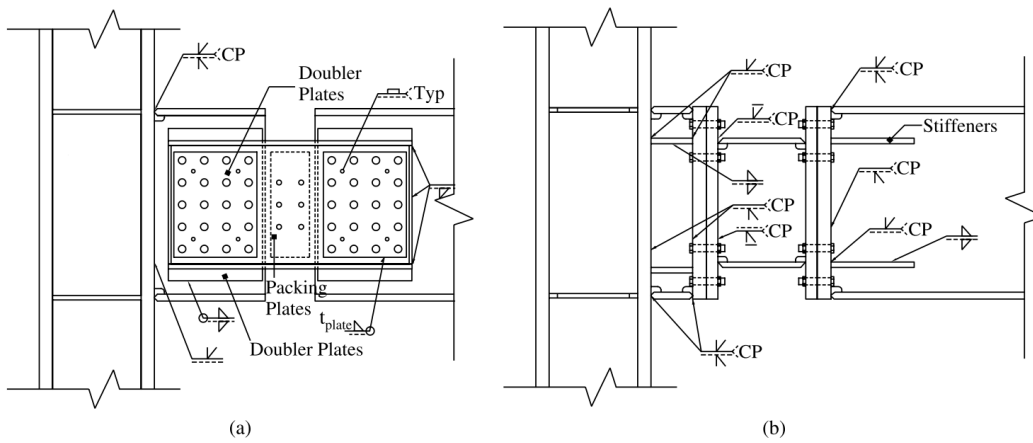
Figure 1.26: Nonlinear replaceable link types developed in Shen et al. (2011)
(a) Type-1: Bolted web link (b) Type-2: End-plate link
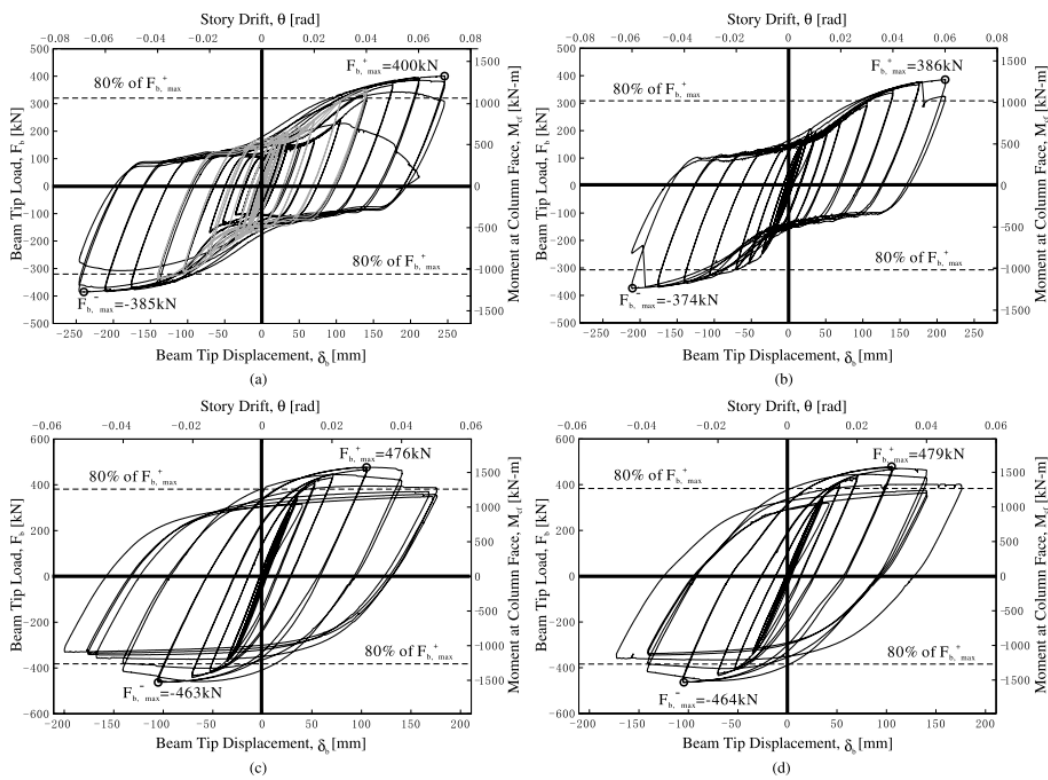
Figure 1.27: Hysteretic response of Type-1: (a) and (b), Type-2: (c) and (d)
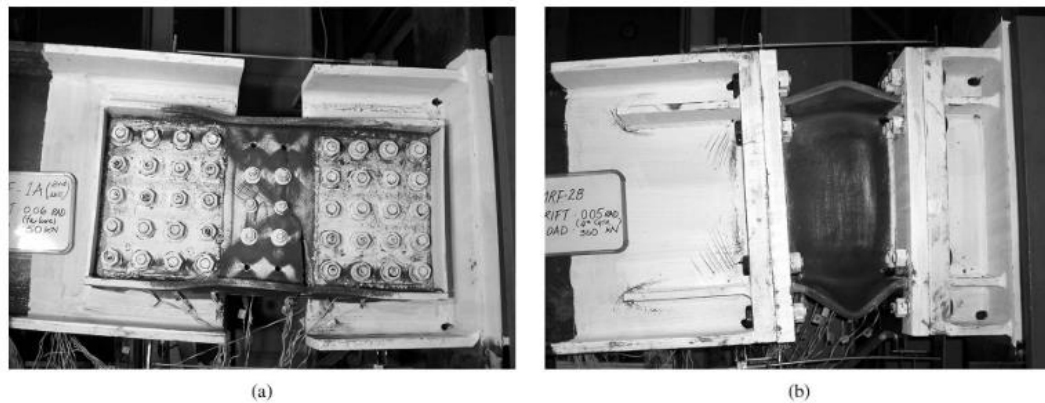
Figure 1.28: Observed damage in (a) Type-1, (b) Type-2

The numerical test results indicated that the total story drift values observed for Type-1 were approximately 50% higher than the values observed in tests performed on Type-2 links, with average total story drifts of 0.065 and 0.04 rad, respectively. The failure modes of the link types were, on the other hands, observed as ductile and brittle tearing in flange and webs of bolted links for Type-1, and local flange and web buckling of end plates for Type-2 link. In summary, it was concluded during the study that end-plate link (Type-2) exhibited greater energy dissipation capacity that the bolted web link, presented in Figure 1.26; however, because of the higher level of deformations occurred in the link, bolted web links (Type-1) achieved much higher rotational capacity.

Wang et al. (2018) and Wang et al. (2019) developed another type of nonlinear link device that may be used as an energy dissipater in precast structures as a connection device that would add energy dissipation capacity and a plastic hinge region. The developed device was named as all-steel bamboo-shaped energy dissipater (SBED). The first paper discusses the dissipater component itself, with the design and testing; whereas the second paper presents the testing of a precast concrete beam-column connection developed with the SBED component. For convenience, they are summarized here chronologically, first the component development and following the SBED connection.

SBED is an energy dissipater component that consists of an inner bamboo-shaped core and an outer restraining tube, which all are made of S235 class structural steel. The component was developed inspired by BRBs with its working mechanism, geometrical shape, and detailing. However, SBED is much smaller in size since it was intended to be used in beam-column connections. Another important difference is the filling between inner core and outer tube, as the confinement of the core is typically achieved through concrete filling. There is not any filling in SBED components as the buckling is intended to be prevented with slubs, which create a segmented core throughout the length to reduce the buckling length in the core. Details of such SBED components are given in Figure 1.29, for convenience.
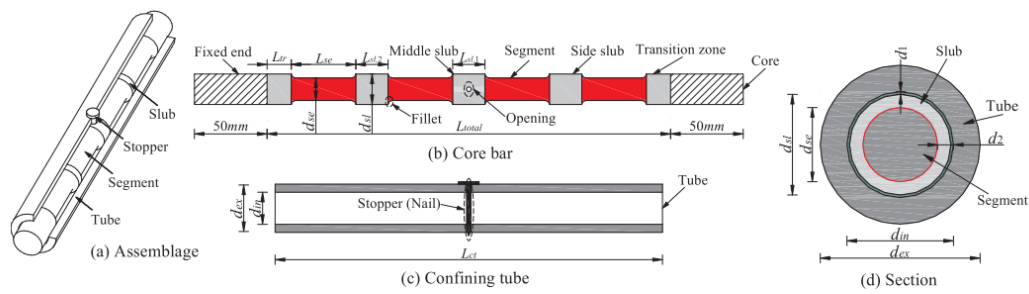
Figure 1.29: All-steel bamboo-shaped energy dissipater (SBED) component (Wang et al., 2018)

During the study, parametric studies were performed on the geometrical variables to investigate low-cycle fatigue and deformation patterns. Afterwards, twelve different SBED components with different slub-segment configurations, and total lengths varying between 230-400 mm, with constant inner and outer diameters, and under different loading patterns up to 4% ultimate strain values were tested and parametric studies were completed. The main conclusions obtained from the study are as follows.

- The length of slubs and segments have significant influence on the resulting force-deformation hysteresis and deformation patterns.

- The failure modes are affected by the lateral deformation from the bending, stress concentration around the fillet, and torsion in the segments. It was discussed that stress concentrations may be prevented by smoothing the fillets and torsion may be eliminated by controlling and limiting the length of segments.

- The compressive strength adjustment factor, which is defined in AISC 341, considering the contact and friction between the core and the outer tube, was determined as 1.0 up to 2.0% strain and 1.2 at 4.0% strain, with linear interpolation in between.

- In general, apart from the specimens that low-cycle fatigue was investigated, strain values close to 4.0% were achieved before failure by excessive bending, stress concentration, or torsion was observed.

Wang et al. (2019), on the other hand, is the follow-up study, which consists of the experimental study on the precast concrete beam-column connection designed with SBED component and post-tensioned tendons. SBED components were used to supply the frame system with energy dissipation capacity and post-tensioned tendon through column and beam was placed to achieve self-centering after a seismic event. During the study, five beam-column connections were tested with different SBED configurations and geometries, and prestressed forces, under simulated seismic loading. The application of SBED components and prestressed tendons are presented in Figure 1.30. Loading protocols were applied in two different manners, one as standard loading incrementally applied up to a drift ratio of 3.5%, and one as repetition loading where repetition started with the residual drift ratio of the first standard application. Connection strengths, equivalent viscous damping values, and self-centering capabilities were investigated during the tests. Force-displacement/drift ratio curves obtained under five different connection tests are given in Figure 1.31. The following conclusions were drawn from the study.

- Small flexure cracks and crushing were observed near the embedded connection plate, which connects SBED to beam. Even if they were regarded

as elastic due to strain values, the structural members exhibited a certain level of damage.

- The energy dissipation capacity of the connection increased with increasing number of SBEDs and decreased with increasing length of SBEDs. Strength of connections increased with increasing prestressing force.

- Bending behavior was observed in SBED components during the rotation of the connection, besides tension-compression and shear behavior occurrence.

(a) Elevation view of the connection zone

(b) Top view of the beam

(c) Side view of the column

(d) SBED (all of the dimensions are marked in the picture)
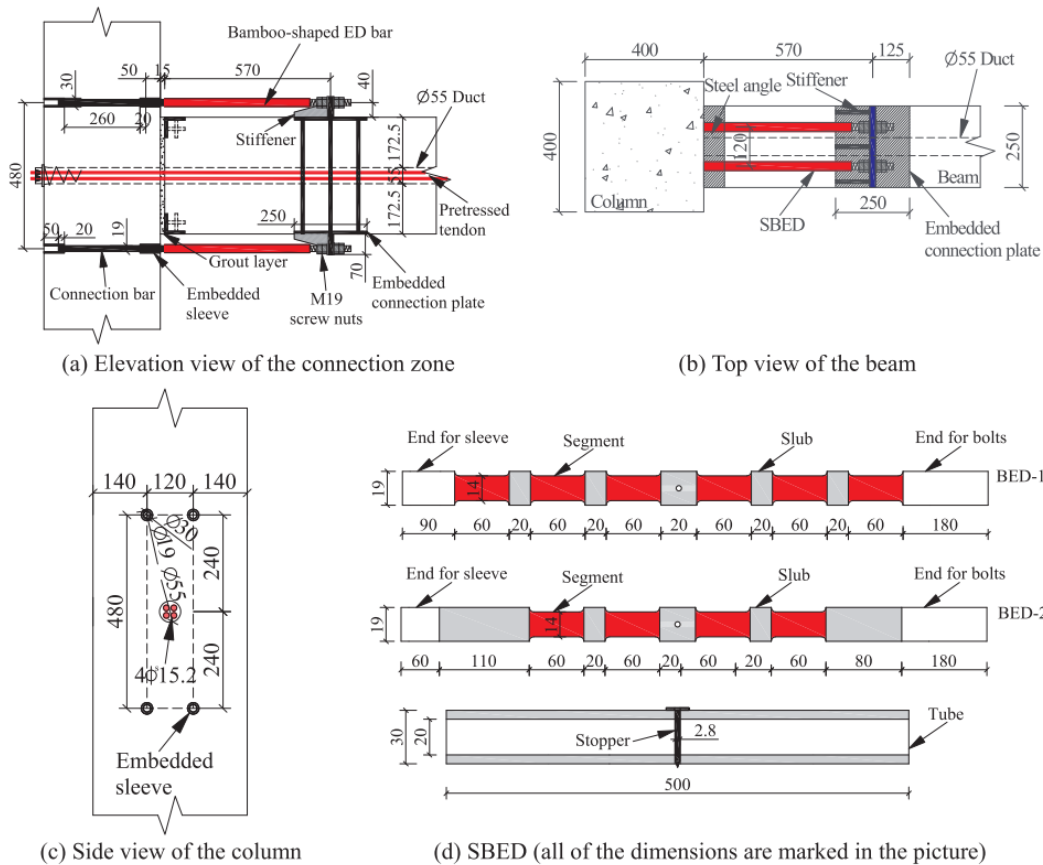
Figure 1.30: Configuration of beam-column connection with SBED (Wang et al., 2018)

46
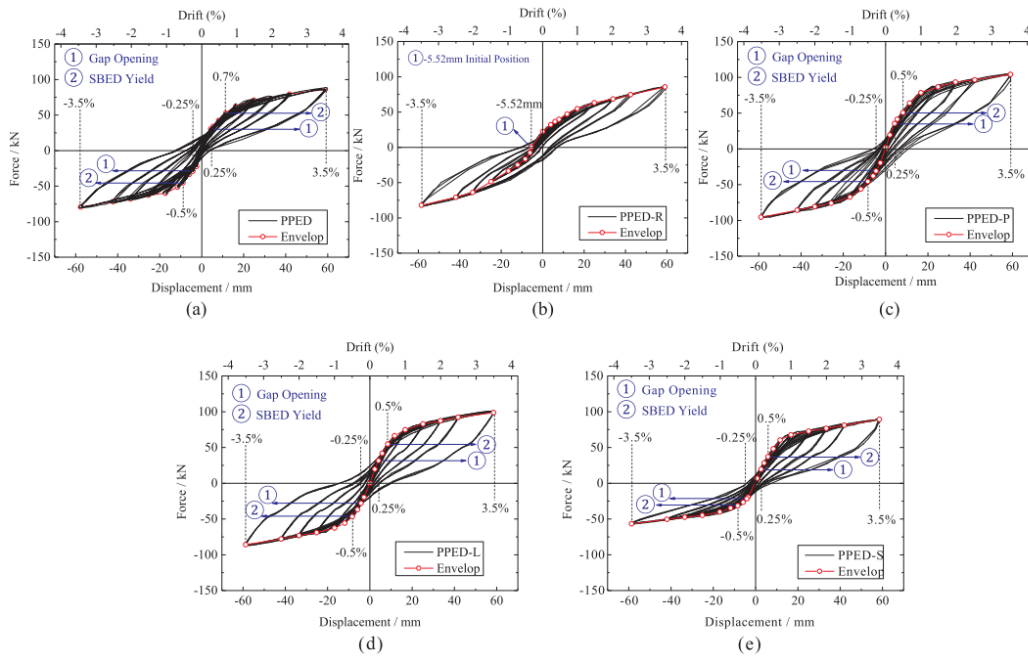
Figure 1.31: Force-displacement/drift ratio curves obtained during connection tests
(Wang et al., 2019)

Huang et al. (2020) conducted research on another hinge connection device type that would be used at beam-column connections of precast concrete frames with the objective of enhancing the stiffness of the frame and the energy dissipation capacity. The connection device type was a friction damper, named Variable Friction Damper (VFD), different from the connection devices that comprise of components made of high-ductility structural steel. The proposed device was also different from other friction dampers that had flat sliding surfaces, which led to single dynamic stiffness after the activation of device. The configuration of VFD and theoretical comparative behavior are given in Figure 1.32 and Figure 1.33, respectively. As given in Figure 1.32, VFD device mainly comprises of an inner steel plate (ISP) connected to the beam, grooved middle steel plate (GMSP), grooved exterior steel plate (GESP), friction pads, clamping bolts and springs (CBS), and high strength bolts. Also, as it can be seen in Figure 1.32(b), a hidden corbel (HC) was placed at the interface, to increase shear strength of the connection. The three main features of this type of

connection are the non-metallic friction pad between GESP and GMSP that supply energy dissipation during the rotational movement; and post-tensioned (PT) tendons through beam and column, to accommodate self-centering capability, and most prominently, additional stiffness to the system through grooves on the sliding interface that leads to a second activation during high seismic demands.

(a) Configuration of HC–VFD–SCPC beam–column connections

(b) Rotation mechanism of HC–VFD–SCPC connections

(c) Variable friction mechanism
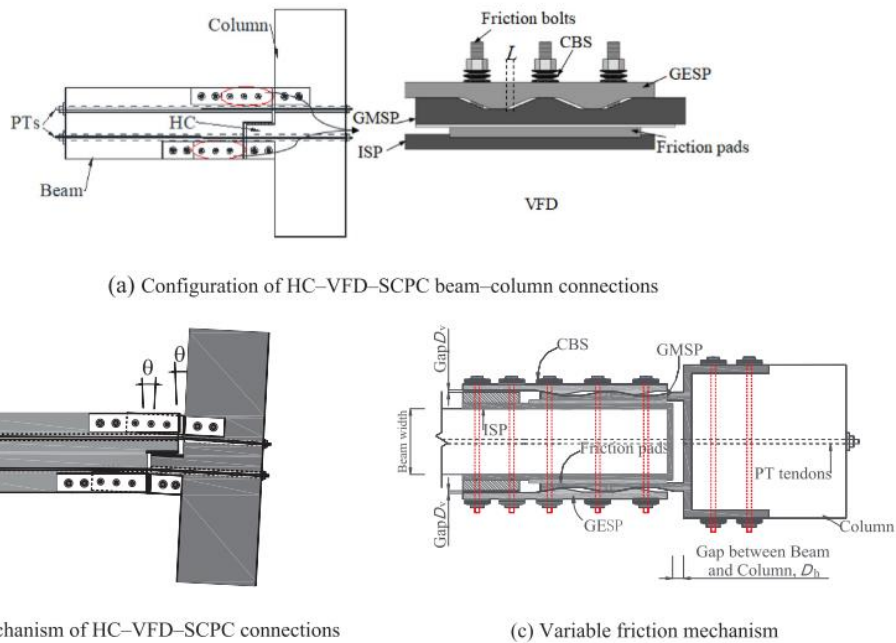
Figure 1.32: Configuration of variable friction damper developed in Huang et al. (2020)

(a) VFD

(b) PT

(c) HC–VFD–SCPC
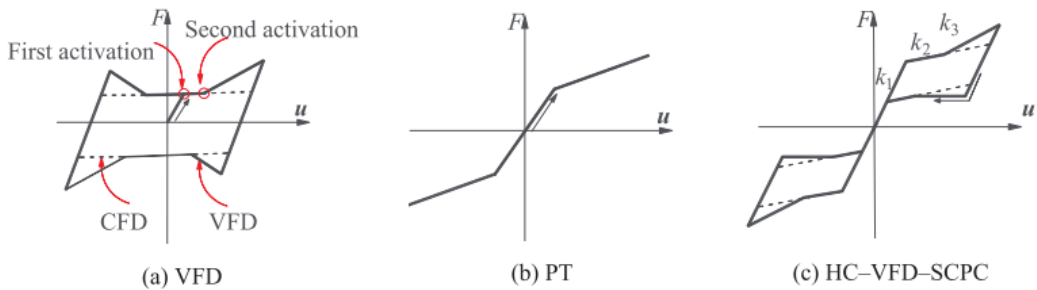
Figure 1.33: Comparative theoretical behavior of VFD compared with flat sliding friction dampers (Huang et al., 2020)

During this study, six beam-column connection tests were performed differing with several parameters such as the number of prestressing tendons, initial tendon force and clamping force on the CBS that controls the friction inside the VFD. Testing protocol was applied to the system with varying story drift ratios up to 4.0% increasing with amplitude of 0.5%. The following results and observations were come up with during the tests.

- Initial PT force affected both the residual displacement and gap opening behavior, as expected, and second activation of VFDs.
- The behavior aimed with the highest importance, added stiffness through second activation, depends mainly on the total CBS force and the angle of grooves on the sliding surface. Therefore, higher stiffness and energy dissipation could be achieved with increasing the number of CBS, along with existence of grooves, compared with the need of increase of clamping force in flat surface friction damper types. It was concluded that this would increase the lifetime of such a type of device, compared with flat surface equivalents.
- Due to the geometry of CBS members, sliding behavior between the springs and bolts occurred at the onset of second activation, which led to loss of expected friction forces through sliding at the grooves.
- Unlike theoretical study, it was observed during the tests that the loss of PT forces should be carefully considered, alongside with the design of CBS members to minimize sliding behavior at the springs.

More recently, Saravanan et al. (2021) published experimental research on a novel fuse-type energy dissipating device that was intended to be used in beam-column connections of steel moment-resisting frames with the aim of containing plastic hinge formation in the internally placed device and ensuring the main structural members to remain undamaged after an earthquake. As Figure 1.34 shows, energy dissipating fuse links are placed at the top and bottom flanges of beams, by fixing them to both beam and column flanges. Fuse links, on the other hand, consist of dog-

bone shaped fuse plates as the main energy dissipating component, and horizontal plates to hold them together and fix the link to beam and column. It was intended that, during an earthquake, rotational motion occurring at the beam ends would cause the links to deform primarily in vertical direction and it would create tensile and compressive strains at the fuse plates. While the working mechanism of fuse links are summarized as that, the primary properties were determined to be the initial stiffness, overstrength connection moment transfer capacity (which was intended to be less than yield moment of connecting beam), and rotation capacity (of at least 0.04 rad).

(a)

(b)
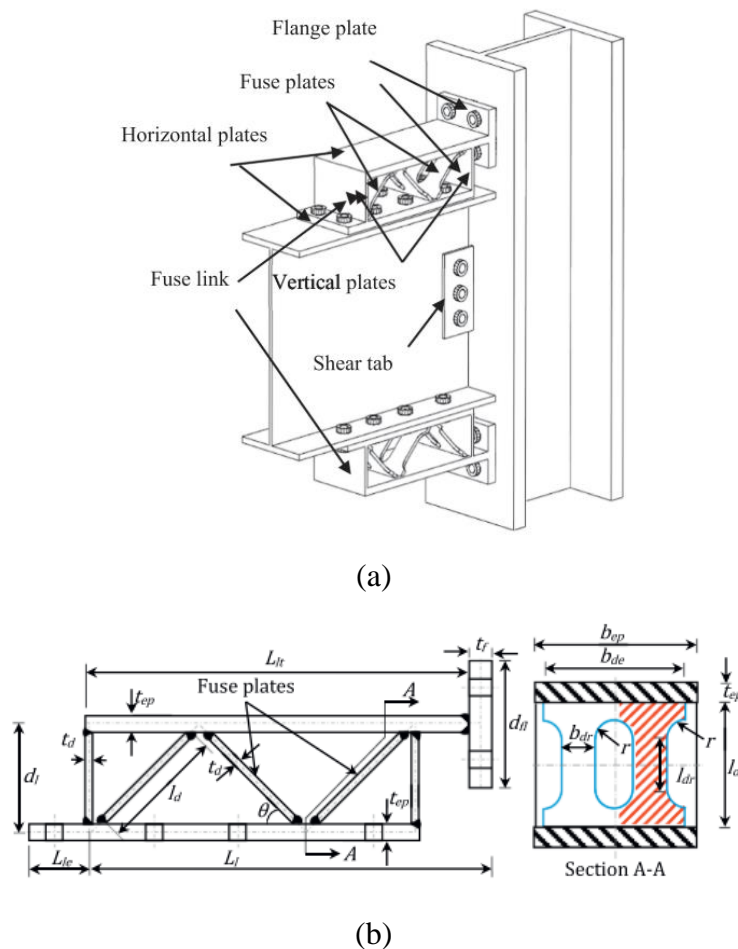
Figure 1.34: (a) Schematic sketch of proposed beam-column connection (b) Geometrical details of fuse link (Saravanan et al, 2021)

The study on beam-column connection with fuse links involves component level tests performed on four different fuse links, mainly varying in slenderness ratio of fuse plates (between 13.5 and 22.5); and beam-column connection subassemblage tests performed on four different connections with varying bolt pretension forces, type of loading and fuse installation configuration. In component tests, the load-deflection behavior, energy dissipation behavior and failure modes of four specimens were investigated to evaluate the comparative performance of the fuse links. In summary,

- all four specimens survived 30 cycles with 0.04 rad drift angle without fracture,
- all specimens reached yield load levels before buckling and ultimate to yield load ratio were 1.07 on average,
- energy dissipation capacities of the specimens were within 15% variation, indicating different slenderness ratios led to similar energy dissipation capacities,
- failure of fuse plates occurred due to buckling, at the middle of plate spans, as expected.

In sub assemblage tests on the other hand, the investigated parameters and observed behaviors were moment-rotation behavior of the connection, energy dissipation, and failure modes. The results and observations of sub assemblage tests are as follows.

- Moment-rotation relationships of four sub assemblages, along with the properties of sub assemblages are given in Figure 1.35. Apart from the specimen where monotonic loading was applied, hysteresis curves are roughly the same.
- Cumulative energy dissipation of three sub assemblages had similar magnitudes, where bolt pre-tension had approximately 10% effect, observed in fourth specimen.
- Investigating the hysteresis curves and damage photos, damage including bucking of fuse plates in the links started at around 0.02 rad, whereas fracture

of them occurred between 0.04 and 0.05 rad. Also, strength degradation beyond 0.04 rad exceeded 20 percent. However, the links exhibited reasonable strength and behavior up to 0.04 rad.

- As a last item, the replaceability of the fuse links are favorable, considering its connection form to beam and columns is suitable.

Details of complete experimental matrix.

Specimen	Config.	Depth of link (mm)	Bolt pretension (kN)	Type of loading	Approx. Max. Strain rate per sec in fuse plate
S1	Regular	100	180	Monotonic	0.00005
S2	Regular	100	180	Cyclic	0.00046
S3	Modified	100	180	Cyclic	0.00046
S4	Modified	100	215	Cyclic	0.00046
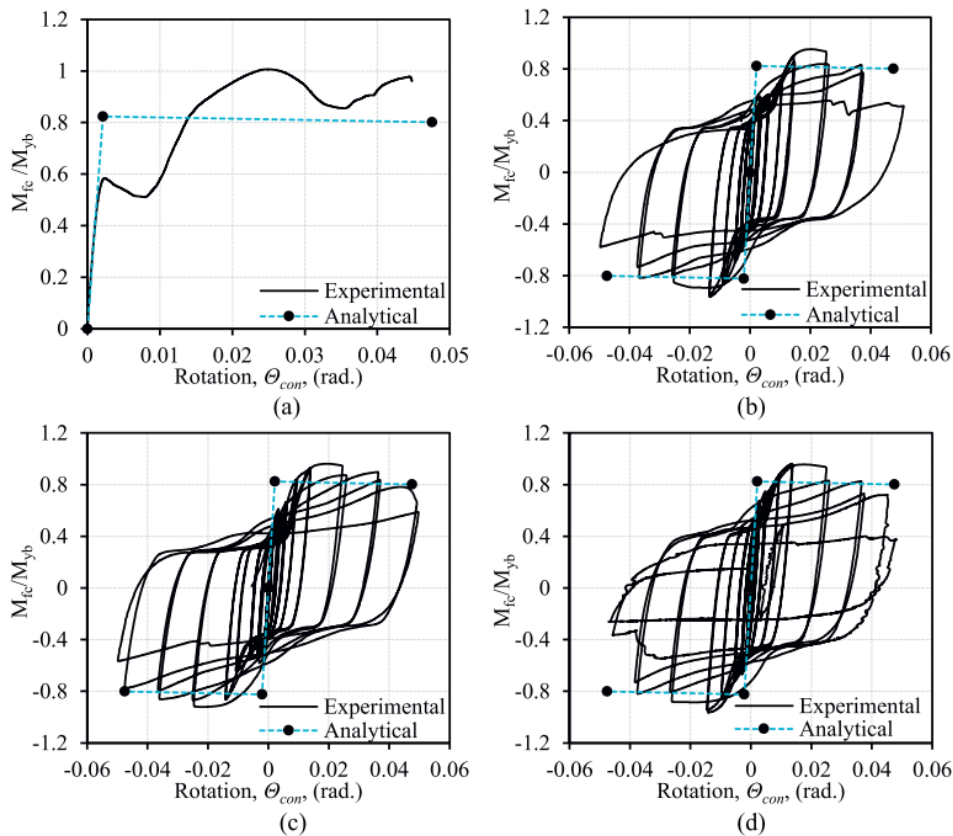
Figure 1.35: Test matrix and Moment-rotation relationships of beam-column connections with fuse links (Saravanan et al, 2021)

52

1.3   Review of Current Professional Practice

Section 1.2 consists of the summary of seismic base isolation and external energy dissipation device literature, by classifying them into several device types, mainly according to the material used and working mechanisms. The section is built on the rationale that the device types are classified from the least to the most relevant, considering the similarities on the mechanisms and utilization in a structural system, for which the device changes its behavior and performance level.

In a similar manner, this section includes the review of the most widely used international standards that are practiced in structural and earthquake engineering. As may be followed in the previous sections and in those international standards, the energy dissipating device types that are discussed so far can be classified into two main groups in terms of the response under cyclic loading such as an earthquake ground motion, which are displacement dependent (rate-independent) devices and velocity dependent (rate-dependent) devices. The last device type of external energy-dissipation devices, which is metallic dampers, and internal energy-dissipation devices – constructed plastic hinges, which is the subject of this thesis, are two main examples of rate-independent devices. Therefore, the review of the provisions of international standards is confined to the regulations of displacement dependent devices.

1.3.1   EN 15129 – Anti-seismic devices

The European Standard, EN15129 – Anti-seismic Devices (European Committee for Standardization, 2018), is the main standard in Europe that regulates the design, production, testing, control, installation, and maintenance of the devices that are used to modify the response of structures under seismic effects. The device types which EN15129 covers are rigid connection devices including permanent connection devices, fuses and shock transmission units, displacement dependent devices, velocity dependent devices, and seismic isolators.

53

Displacement Dependent Devices (DDD) are further divided into two groups, which are Linear Devices (LD) and Nonlinear Devices (NLD). As their names imply, the standard makes the distinction in terms of altercation of the structural system in which the devices are mounted i.e., Nonlinear devices introduce significant nonlinear behavior to the structure while dissipating energy. Whether it is a linear device or a nonlinear device, they are regulated by defining several provisions on performance/design parameters, materials, and testing.

Performance parameters of a DDD are determined as the effective stiffness (K_{eff}) and effective damping (ξ_{eff}) for a linear device. Initial stiffness (K_1) and post-yield or secondary stiffness (K_2) shall also be defined for a nonlinear device. Several acceptance criteria are also defined related to the performance parameters, which are listed as follows.

- A linear device shall exhibit an effective damping (ξ_{eff}) less than 15%., and ratio of the difference between initial stiffness and effective stiffness (K_{eff} - K_1) to the initial stiffness (K_1) shall be less than 0.2.
- The loading phase of a force-displacement relationship shall not exhibit any strength degradation.
- The standard also specifies tolerance limits on performance parameters for the evaluation of testing with any theoretical values in terms of supply, ageing, temperature, and strain rate.
- For nonlinear devices, the following additional provisions are defined.
    - The design displacement of a device shall not exceed the displacement demand determined for a ULS design earthquake (t_r = 475 years).
    - The residual displacement at zero force at the end of an earthquake, determined under SLS design earthquake (t_r =95 years) shall not exceed the maximum of 5% of device capacity displacement and 10 mm.

The standard separates the materials of a DDD into two groups in terms of their functions: Core function material, which defines the seismic behavior of the device and structural function material. Related to the function, the standard guides the assessment of conformity of used materials by referring to the standards related with the material. For instance, if the core function material is steel, the characteristics of the material shall conform EN 10025, EN 10083, or EN 10088, whereas for rubber as a core material, it refers to the provisions introduced in the elastomeric isolator section of the standard.

Mechanical testing of displacement dependent devices is also regulated by the standard by dividing the procedures into two categories: Type testing and factory production control (FPC) testing. It is specified that both material and complete devices shall be subjected to both type tests and FPC tests, under cyclic loading. Several conditions regarding the tests are summarized below.

- Type tests and FPC tests of materials shall be performed by conforming to certifications attested according to European standard, if any. If not, the manufacturer shall establish and perform test procedures that are suitable for evaluating the performance parameters of the DDD.
- Type tests shall be performed whenever the material and/or geometrical properties of a new device change. If the geometrical differences are less than 20%, a new type test need not be performed.
- Type tests shall be performed together with all the designated connections to the structural members.
- If the capacity of a device exceeds the capability of any facility certified according to European Norms, devices can be scaled to suitable sizes and capacities, on the condition that calculations that exhibit that scaling is justified.

FPC tests shall be applied at least 2% of the total supply for a specific case, ensuring that it is not less than one.

1.3.2 ASCE 7 – Minimum Design Loads and Associated Criteria for Buildings and Other Structures

ASCE 7-22 (American Society of Civil Engineers, 2022), the most recent version was taken into effect in 2022, is the main structural engineering standard that is currently used in United States. It is also arguably the most widely used standard in many countries where certain practices are not well-established in a standard format. ASCE 7 is also the standard in the United States that energy-dissipating devices are well-defined in terms of design criteria, performance definition and verification, and testing.

The related chapter in the standard, which is Chapter 18, starts with defining a damper device as the entire system with the device itself, and all the connection members, such as bolts, pins, and plates altogether. A similar approach is also present in EN 15129 in terms of the description of testing. The standard classifies the damper devices into three main groups, again similar to EN 15129, which are displacement dependent devices, velocity dependent devices and force-controlled devices.

The design criteria of damper devices, specified in the standard, are summarized below.

- All the components of the damping system shall be designed according to MCE (t_r = 2475 years) loads. Only the members designated for inelastic behavior shall exceed linear-elastic range. All the other members shall remain elastic under an MCE level seismic action.
- Overstrength factors or material factors shall not be used.
- During the analysis and verification of a structural system with damper device, nonlinear response analysis shall be used.
- The redundancy of the dampers in a structural system shall be ensured. In a structure, if the number of devices in a story is less than four, or if the number of devices located on each side of the center of stiffness of a story is less than

two, then the devices shall have 130% of design displacement of dampers calculated under MCE condition.

The performance of the damper devices is defined and verified by considering the following conditions.

- Low-cycle, large displacement degradation.
- High-cycle, small displacement degradation.
- Adhesion of device parts, which shall remain separate throughout the lifetime, caused by corrosion, degradation, and moisture.
- Exposure to environmental conditions such as temperature, humidity, and reactive or corrosive substances.

Testing of damper devices are well-established in the standard, by classifying the tests as prototype tests and production tests, which is the same as EN 15129. The standard defines the sequence and cycles of the prototype testing in a detailed manner, including the simulation of wind load, seismic load, and temperature variation with increasing displacement values proportional to MCE displacement capacity. Test results are evaluated by considering the following conditions and criteria.

- Force-displacement relationships are recorded during all the procedures. Maximum force and displacement values are determined and resulting dissipated energy, and effective stiffness values are calculated for each cycle.
- For the test that simulates wind load, no yielding or breakage shall be observed.
- For the seismic load test, maximum and minimum forces at zero displacement at each cycle shall differ less than 15% from the average maximum and minimum force value at zero displacement, and also from target design force at zero displacement.
- The condition above shall also be satisfied for the forces at the maximum and minimum displacement values.

- The dissipated energy at each cycle shall differ less than 15% of the average of dissipated energy.

Regarding the production tests, the standard demands that 100% of the produced dampers in a specific project shall be tested at 0.67 times the MCE displacement with a frequency corresponding to 1.5 times the fundamental period of the structure, which the damper devices will be used. The measured values shall remain within the design specifications.

1.4   Objective and Scope

The objective of this study is to develop a plastic hinge device for use in beam- ends where plastic hinge formation is expected according to the strong column-weak beam principle, which is one of the basic principles of seismic design. In addition to confining plastic deformations in the designated regions of beams and dissipating the hysteretic energy stored in the structure during an earthquake excitation, another fundamental feature of these devices is that they are replaceable. Besides the practicality provided by their replaceability after an earthquake, the devices are also compatible with the structural framing system and do not require any changes in the architectural design of the building.

The first consideration during the development of the devices was that the design was made to meet the structural design parameters. In addition, interchangeability was also considered in detailing the device elements.

The scope of the presented thesis study is organized as follows:

1. An experimental setup was designed, produced, and built in the structural laboratory, which would be suitable for the device design parameters and the resulting dimensions which we considered in the prototype design. The forces and displacements to be applied in the experiment were determined by considering the device capacities and it was ensured that the test specimens would attain the targeted performance.

2. In the experiments, it was aimed to advance to the failure point and to observe the maximum rotational capacity and failure mode of each prototype specimen. Based on these drawings, improvements were made in terms of geometry, material, and design. Resultantly, a suitable and optimum form was aimed to be obtained in terms of performance, applicability, and ease of production. During this study, five different prototype concepts/forms were designed and tested before achieving the final prototype form.

3. It was aimed to conduct frame tests of the prototype device with certain performance and to examine its performance at the frame scale. Accordingly, a frame was designed and produced in conformance with the current configuration and capacity of the devices. The considerations at this stage are listed below.

   - Prototype device capacity and geometry
   - Laboratory capacity: Laboratory geometry, force, and displacement application capacity,
   - Adequacy of obtaining displacements and displacements between floors that will plasticize the devices and reach their capacity,
   - High enough capacity of the frame to remain elastic when operating the devices in zones of plasticization.

4. In order to reach the plastic capacity of the devices without reaching the elastic capacity of the frame and to stay away from the force capacity of the experimental setup as much as possible, it was aimed to use an articulated base frame. After this experiment failed to achieve the re-centering target, fixed base frame implementation was started.

5. In the frame where the devices are placed, a two-story frame was designed with the aim that structural elements that are expected to remain in the elastic region after the experiments are ensured, and devices are placed only at the first-story beam ends. In the next experiment, a single-span frame was also tested to reduce the frame force capacity and to reach significantly higher displacement values.

6. To determine the pre- and post-experimental performance of the frames, it was aimed to create analytical models where frame members are modeled with Fiber Section definition for continuous plasticity, and P-Cells are modeled with Zero-Length Members for having lumped plasticity. For this, the OpenSees platform was chosen.

This study consists of five chapters. The titles and brief contents are as follows.

Chapter 1:   Introduction. Problem Statement. Literature Survey. Objective and Scope.

Chapter 2:   Development of the Concept. Introduction of P-Cell.

Chapter 3:   P-Cell Unit Tests. Test methodology and design calculations are introduced. Test setup and loading protocol are presented. The design of each P-Cell formation and performed test results are presented and discussed.

Chapter 4:   Frame Tests. Frames with different P-Cell configurations and geometries are introduced. Design, production, and installation of the frames; also implemented loading protocols and ground motions are presented. Test results are presented and evaluated.

Chapter 5:   Summary. Conclusion.

CHAPTER 2

DEVELOPMENT OF THE CONCEPT AND INTRODUCTION OF P-CELL

Interventions to the structural framing systems for improving seismic response through enhanced energy dissipation can be broadly classified into two categories, external and internal. These two categories can simply be idealized by springs connected in parallel and series arrangements as shown in Figure 2.1 schematically. For all cases, $k_d << k_f$ and $c_d >> c_f$ where k and c are the stiffness and damping coefficients respectively, where f stands for the framing system and d for the energy dissipating devices.
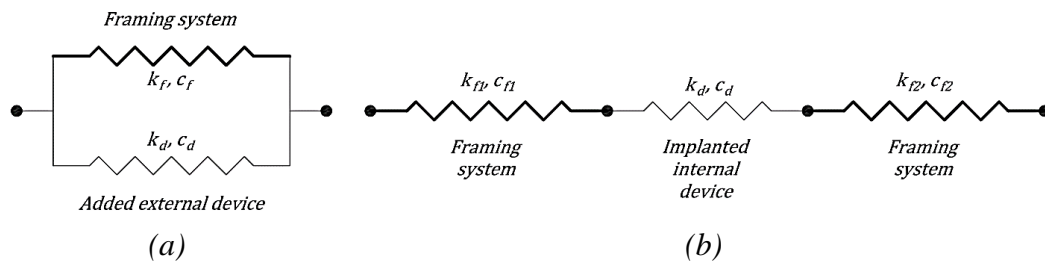
Figure 2.1: Schematic representations of external and internal interventions for enhanced energy dissipation (a) External intervention, (b) internal intervention.

The basic types of external interventions are metallic dampers, friction dampers, fluid viscous dampers, and buckling-restraint braces as discussed above. Their working principle is simple. External devices undergo the same displacements and velocities of the framing system at their connection points. Therefore, their effectiveness in energy dissipation, whether possessing displacement (metallic dampers, friction dampers, and buckling-restraint braces) or velocity (fluid viscous dampers) dependent hysteretic character, depends on the magnitude of displacements and velocities that the main framing system undergoes. Accordingly,

external devices are not significantly effective in rigid systems such as reinforced concrete frame-wall systems, but more effective in flexible steel framing systems. Another point that should be noted is the additional resisting internal forces developed by the external devices. They eventually increase stiffness and damping of the framing system. Hence, additional internal forces develop in the framing system at the connection points of the external devices. Natural period of the framing system also decreases which usually leads to attracting larger seismic forces during earthquake excitation. Finally, external devices are formidably visible. They challenge architectural functions negatively, which makes them quite undesirable in residential buildings.

Internal interventions are mostly realized by weakening of a critical element, or a critical component of the framing system, hence allowing the formation of larger deformations (displacement, rotations, and strains) at that location. Hence, an energy dissipating device implanted at that location can effectively dissipate larger amounts of energy, owing to significantly larger deformations. It is logical to choose the weakening regions as those where the deformations are already large as a consequence of the structural system characteristics, such as the stories with maximum interstory drift, the ends of flexural members with maximum rotation and material fibers with maximum extension. Hence, deformation control is a critical issue for internal interventions. Weakening of a critical region leads to reduced stiffness (Figure 2.1.b), accordingly larger deformations under earthquake excitation. On the other hand, an implanted, i.e., an internal energy dissipating device does not challenge the architectural features of the building system. Ideally, they are an integral part of the framing system.

It is worth of mentioning here that the most popular seismic intervention system developed so far, namely seismic base isolation, falls into the internal intervention category in view of Figure 2.1, although it gives the false impression of external intervention. A weakened region in terms of a weakened story is introduced between the building frame and the foundation that allows large displacements or interstory drifts. Then, isolation devices dissipate significant amounts of energy through either

shear deformation or friction in accordance with these large displacements. The lengthening of the building lateral period due to the low lateral stiffness of weakened story underneath is of course another major factor contributing to the reduction of attracted seismic forces during earthquake excitation.

The concept of plastic hinge cell (P-Cell) introduced in this thesis study is based on an internal steel intervention device, which is in the same category with the "Beam-Column Connection Devices" discussed in Section 1.2.6 above. It provides full connection of a beam-end to a column face at a beam-column joint with full vertical and lateral shear capacity larger than the flexural capacity related demand, but with a reduced flexural capacity compared to the demands from linear elastic response analyses. Hence, a P-Cell imitates a constructed plastic hinge which is formed in a frame or a frame-wall system under severe earthquake excitation in view of the capacity design principles (Figure 2.2). Reduced flexural capacity is directly associated with the response reduction factor R employed heuristically in conventional seismic design.

P-Cell is intended as a replaceable component. When all P-Cell components that undergo plastic deformations (components #2 in Figure 2.2) are removed from the frame after a severe earthquake and converted to zero-moment hinges temporarily, the frame is expected to recover most of its permanent deformations theoretically. Some deformation may remain due to the rotational friction resistance of the central pin, #4 in Figure 2.2.
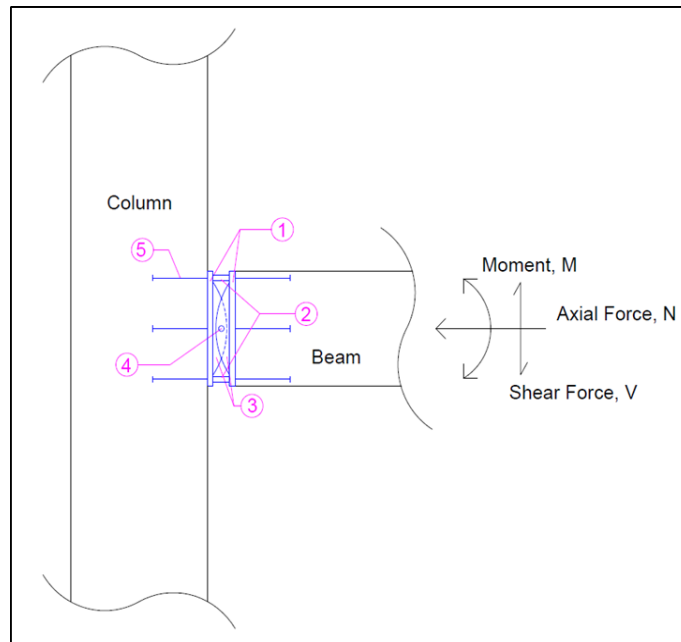
Figure 2.2: Schematic representation of a typical P-Cell implanted at a beam-
column joint

Implementation of P-Cell in a framing system ideally suits to modular precast systems such as precast concrete and steel structures. Its implementation to RC monolithic frames is clearly possible but requires further studies for anchoring of the devices into the beam ends and column faces and allowing construction joints along the boundaries of concrete slabs.

P-Cell concept is elaborated in the following Chapters through component tests, frame tests and analytical predictions.

CHAPTER 3

LABORATORY TESTS OF P-CELLS

The concept, mechanism, properties and the literature on external and internal energy dissipation devices have been discussed in the previous chapters in an orderly fashion with the approach of chronology, and similarity to the subject of this study. Chapter 2 further discussed and introduced the concept of an internal intervention device to framing systems, with the objective of imitating a plastic hinge mechanism that develop at the ends of ductile frame members, mainly the beams.

This chapter consists of the presentations on the development of P-Cells proposed as a novel internal energy dissipation device through a set of component tests where the types and configurations differ in terms of performance limits, geometries and materials used in design and production. The component tests are grouped by considering mainly the significant revisions in their configurations and working mechanisms, while main groups are further divided into versions according to relatively minor geometrical and production-related modifications. P-Cell types and their subgroups are presented in Table 3.1 with a brief description of the differences between them. Type PT1 is the basic type, which is then evolved to the other types mainly for preventing premature failures during cyclic rotational response, accordingly for improving the rotation capacity. The introduction of the tested P-Cell types, design information, test set up, test results and discussions of test results are presented for each P-Cell type separately in the following sections.

Table 3.1: P-Cell Type Matrix

Test	Type	T/C Component
1	PT1	Hollow Section
2	PT2A	Hollow Section, Tapered
3	PT2B	Hollow Section, Tapered, Replaceable
4	PT3	I-Section Profile
5	PT4	H-Section Profile, Buckling-Restraint

3.1 Test Setup, Test Methodology and Instrumentation

The section introduces the testing of P-Cell units by describing the geometrical and mechanical properties of the test setup, method of application of loads and displacements, and the capacity of load application mechanism in relation with the design capacities of the tested prototypes. The tests of P-Cells units presented in this Chapter of the thesis were performed at the Structural Mechanics Laboratory of METU Civil Engineering Department.

As introduced in Chapter 2, P-Cells are developed with the aim of working as an internal beam-column connection device that imitates the formation of monolithic plastic hinges at the end of a beam. In other words, the behavior of a P-Cell during a reversed cyclic loading is governed and determined by its nonlinear moment-rotation relationship whereas their behavior in axial and shear are linear elastic. The design and performance parameters of a P-Cell are mainly yielding and maximum values of moment and rotation capacities. Therefore, any P-Cell unit test is conducted by applying moment or rotation to the P-Cell, directly or indirectly. The P-Cell test set-up (Figure 3.1) was conceived with this rationale.
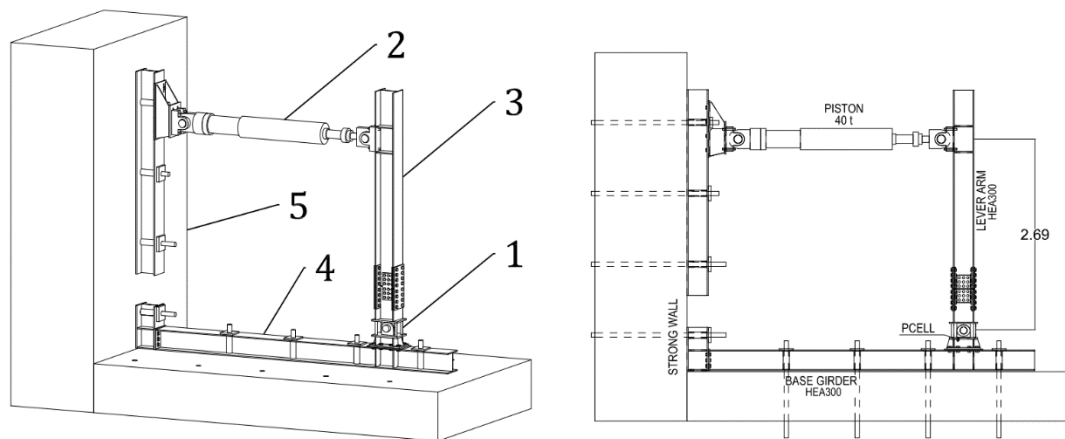
Figure 3.1: Schematic 3D and 2D elevation views of P-Cell test setup

The P-Cell test setup, which is schematically presented in Figure 3.1, is composed of the following main components.

1. *P-Cell unit*

2. *Piston*

   It is a servo actuator, which is used to apply lateral displacement at the top of the setup, with a maximum load capacity of 400 kN.

3. *Lever arm*

   It is used to transfer the lateral displacement applied at the top via the piston to the P-Cell unit as rotation, which is connected to the base of test setup. Applied displacement at the top of lever arm creates rotational motion on the P-Cell, around the central pin of the P-Cell unit.

4. *Base girder*

   It functions as a fixed-end condition at the base of P-Cell unit and the test setup. It is connected to the reinforced concrete strong floor of the laboratory via high-strength M60 bolts, which resists shear forces and tensile forces that due to sliding and uplift actions as a result of the application of lateral displacement.

5. *Strong wall*

   It is used to provide a very rigid support for both the piston and the base girder in order to prevent any movement of the members of test setup and loss of force flow on the test setup.

It is suitable to point out the compatibility between the capacities of elements of the test setup, mainly the P-Cell unit, the piston, and the lever arm. The geometrical and material properties of the lever arm is selected during the design phase as HEA300 profile structural steel with a steel class of S275. These properties indicate that the elastic and plastic bending moment resistance of the lever arm is 346 kN.m and 380 kN.m, respectively. The maximum design moment capacity of the P-Cell components, as will be detailed in the following sections, is expected between 180-200 kN.m. Similar moment capacities were observed during different unit tests, with a particular test where a maximum moment of 250 kN.m was reached. Nevertheless, it may be concluded that the observed maximum moment values remained well below the elastic moment capacity of the lever arm, indicating that the test setup remained in the linear elastic range, as expected.

On the other hand, it is mentioned above that the maximum force capacity of the piston is 400 kN, and the height of the lever arm, or centerline-to-centerline distance between the piston and the P-Cell unit, is 2.69 m. Therefore, the maximum moment that can develop on a P-Cell unit is 1055 kN.m, shown by the simple calculation given below.
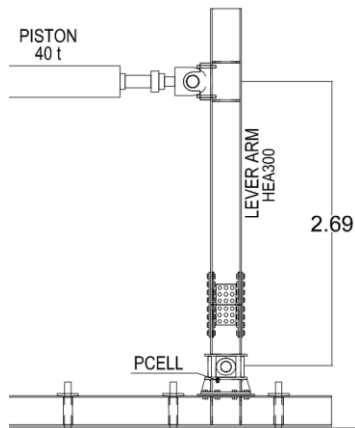
$$F_P = 40 \times 9.81 = 392.4 \ kN$$

$$d_{Arm} = 2.69 \ m$$

$$M_{Cap.} = F_P \times d_{Arm}$$
$$= 392.4 \times 2.69$$

$$M_{Cap.} = 1055.6 \ kN.m$$
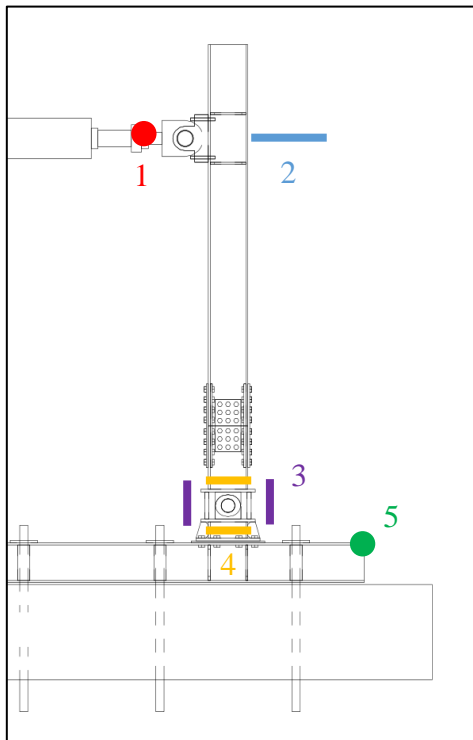
Instrumentation of P-Cell Unit

Figure 3.2: Locations of instruments of P-Cell test setup

Earlier in this section, the methodology of P-Cell unit tests was defined, also by introducing the test setup developed in the laboratory. The instrumentation of test setup is also presented in Figure 3.2 and Table 3.2. The main instruments that are used in the setup are (1) load cell, which records the force that is calculated in response to imposed displacement, and (3) four LVDTs, which are placed at four corners of P-Cell unit. Those two types of instrument are used to calculate the moment indirectly applied to P-Cell and the rotation observed on the P-Cell, respectively. Relevant calculation method for moment and rotation are visualized in Figure 3.4.

Table 3.2: List of instruments which are used during P-Cell tests

| No	Type	Location	Quantity	Feature
1	Load cell	Piston	1	Recording the force resulting from applied displacement
2	300 mm LVDT	Top of lever arm	1	Validating applied displacement at top of lever arm
3	50 mm LVDT	Corners of P-Cell	4	Calculating P-Cell rotation through geometry
4	10 mm LVDT	Top and bottom of P-Cell	2	Recording relative lateral displacement on P-Cell
5	30 mm LVDT	End of base girder	2	Recording possible sliding and uplift of the base girder

(a)

(b)

(c)
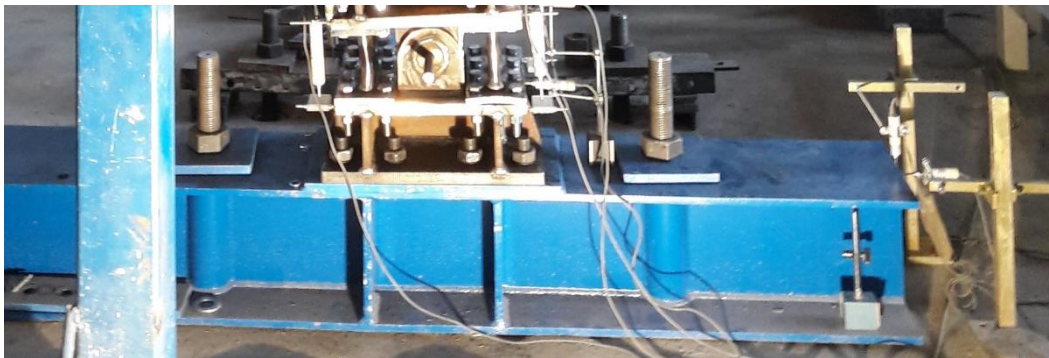
(d)

Figure 3.3: Instrumentation of prototype test setup: (a) 300 mm LVDT at the piston level, (b-c) LVDTs at the four corners of P-Cell unit, (d) LVDTs at the top and bottom of P-Cell and at the base girder

3.2 Design Calculations of a P-Cell Unit

It is mentioned in the previous section that the behavior and performance of a P-Cell is determined in terms of its moment-rotation relationships under load reversals, which is obviously nonlinear. That is, a P-Cell behaves in the linear elastic range without exhibiting any permanent deformation and energy dissipation. However, when the linear elastic moment capacity is exceeded, it starts to behave in the inelastic range by exhibiting plastic deformations in its dedicated components. The yield point, which practically determines and governs the behavior of a P-Cell is expressed in terms of the yield moment M_y, yield rotation θ_y, and rotational stiffness, k_θ. Rotation response develops around a central pin, where the shear force in the pin is transformed into rotational moment via the semi circular drums having a shear span of $h/2$ (Figure 3.4). The design calculations of a P-Cell are presented below with a schematic sketch indicating the geometry and force diagram of a P-Cell first, and then the formulation of design calculations.
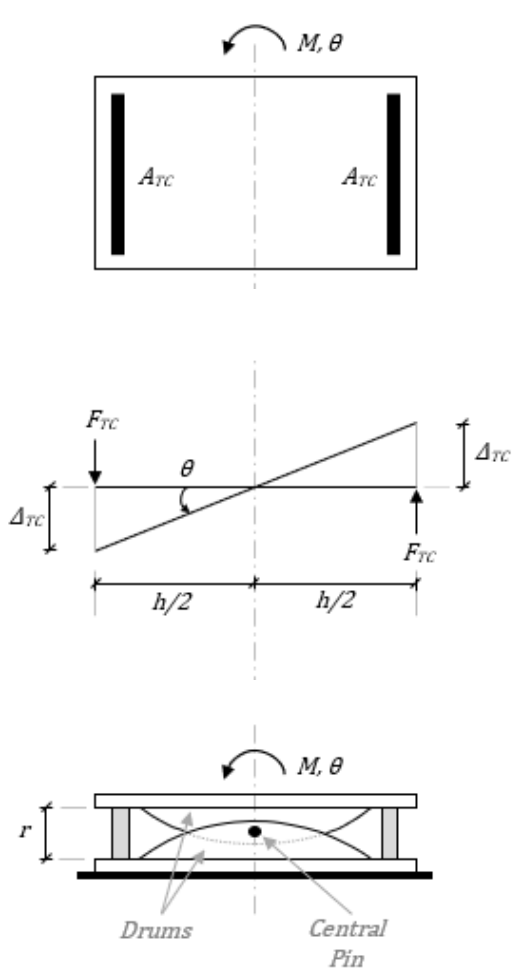
Top view of a P-Cell and illustration of T/C components

M: Bending moment acting on the P-Cell

θ: Rotation of the P-Cell

A_{TC}: Total cross-sectional area of the T/C components in each side

Deformation diagram of a P-Cell at a rotated position

F_{TC}: Total tensile or compressive force on the T/C components in each side, at the rotated position

Δ_{TC}: Axial deformation of the T/C components at the rotated position

h: Distance between the centerlines of T/C component (moment arm)

Side view of a P-Cell at the undeformed position

r: Clear lenght of T/C bar

Figure 3.4: Force and deformation mechanism of a P-Cell

The moment that develops on a P-Cell at any instance in the linear elastic range is calculated simply with the following steps.

$$M = A_{TC} \times \sigma_{TC} \times h \quad ; \quad \sigma_{TC} = E_{TC} \times \varepsilon_{TC}$$

$$M = A_{TC} \times E_{TC} \times \varepsilon_{TC} \times h \tag{1}$$

In Equation (1), E_{TC} is the elastic modulus of the material of T/C component and ε_{TC} is the strain developed at the T/C component.

The rotation of a P-Cell at any instant is calculated with the following equation.

$$\theta = \frac{\Delta_{TC}}{h/2} \quad ; \quad \Delta_{TC} = \varepsilon_{TC} \times r$$

or,

$$\theta = \frac{2\varepsilon_{TC}r}{h} \tag{2}$$

The rotational stiffness of a P-Cell, afterwards, is calculated via Equation (3) by combining Equations (1) and (2).

$$k_\theta = \frac{M}{\theta} = \frac{A_{TC}E_{TC}h^2}{2r} \tag{3}$$

The equations introduced above are valid for any loading step during the rotational motion of a P-Cell that eventually develops a moment-rotation response, as long as the response remains within the linear elastic range. Considering the P-Cell design, yield moment and yield rotation pair are determined for incorporating the P-Cell into the system of structural members. Hence, the same equations can be used for expressing the yielding state, by using the yield subscript *y*. Consequently, yield moment M_y, yield rotation θ_y, and initial rotational stiffness $k_{\theta i}$ are determined with Equation (4), Equation (5), and Equation (6), respectively.

$$M_y = A_{TC} \times f_{y,TC} \times h \quad ; \quad f_{y,TC} = E_{TC} \times \varepsilon_{y,TC}$$

$$M_y = A_{TC} \times E_{TC} \times \varepsilon_{y,TC} \times h \tag{4}$$

$$\theta_y = \frac{2\varepsilon_{y,TC}r}{h} \tag{5}$$

$$k_{\theta i} = \frac{M_y}{\theta_y} \tag{6}$$

These equations are simply derived from the first principles of mechanics. Such simplicity is an advantage in design.

3.3   PT1: P-Cell with Hollow-Section T/C Bars

This section introduces the P-Cell type PT1, which is the first configuration of the P-Cell units that were developed during the initial phase of the development of P-Cells. Test #1 was performed on PT1, the first P-Cell unit that was developed during the laboratory testing phase of the PhD study.

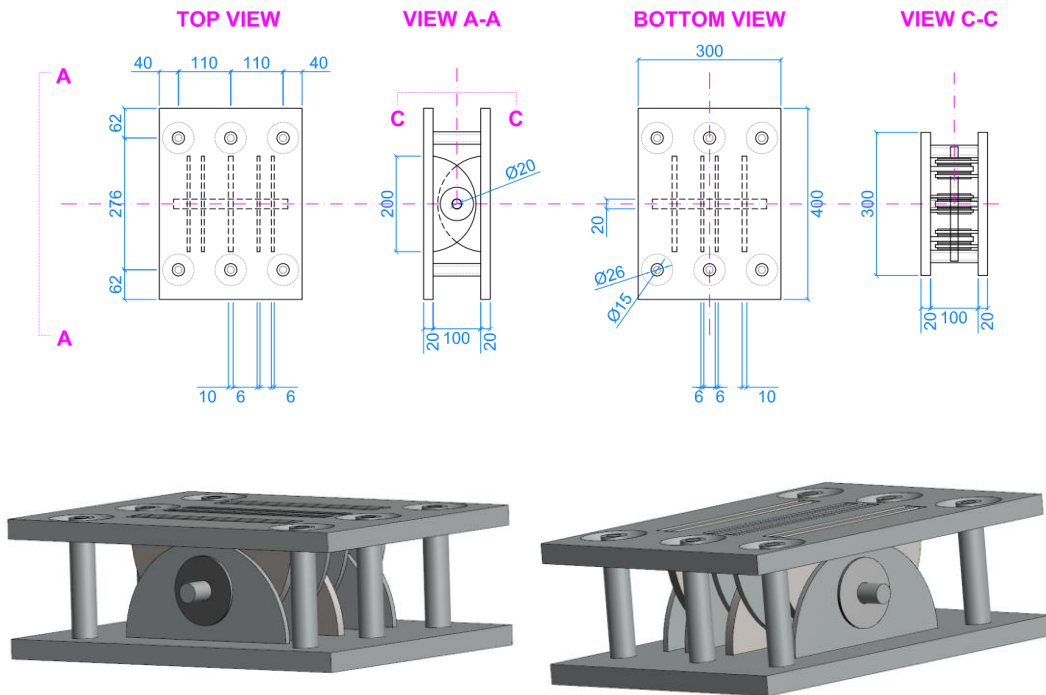The geometric configuration of PT1 and its components are given in Figure 3.5 below.

Figure 3.5: 2D and 3D drawings of PT1. Dimensions in mm.

3.3.1   Design Calculations of PT1

The design formulation of a typical P-Cell was introduced in Section 3.2. In this section, the formulation is specialized to determine the design parameters of PT1.

Relevant geometrical and material properties are also presented in between the design calculation steps given below.

The design phase of P-Cell type PT1 includes the determination of geometrical and material properties. Geometrical properties are already presented, however several points may be further emphasized.

P-Cell type PT1 is comprised of two 20-mm thick backing plates, whose dimensions suit the beam section size, designed with HEA300 steel profile. T/C bars were also placed in a way that the centerlines of T/C bars coincided with the centerline of flanges of H-section hence the tensile and compressive forces would be transferred without any eccentricity. The number of T/C bars were selected considering redundancy in case of rupture during the extreme stages of loading. The material class of T/C bars were selected to have the desired yield and ultimate moment capacities expected during the tests. In the light of the discussion above, the parameters related to the design formulation and the results are presented below.

The outer and inner diameter of the hollow section T/C bars were 26 mm and 15 mm, respectively. The total and clear length of the bars was 100 mm, where three bars were used at each side of PT1.

$$A_{TC} = n_{TC} \times \frac{\pi}{4} \times (D_o^2 - D_i^2) = 3 \times \frac{\pi}{4} \times (26^2 - 15^2)$$
$$= 1062.6 \ mm^2$$

The steel material of T/C bars were selected as S355, having a minimum yield strength of 355 MPa. The coupon test results gave the following mean mechanical properties of the T/C bars.

$$f_{y,TC} = 376.4 \ MPa, \quad \varepsilon_{y,TC} = 0.001656, \quad E_{TC} = 227247 \ MPa$$

As a result, the design parameters of PT1 were calculated as follows.

$$M_y = A_{TC} \times f_{y,TC} \times h = 1062.6 \times 376.4 \times 276$$

$$\boldsymbol{M_y = 110.4 \ kN.m}$$

$$\theta_y = \frac{2\varepsilon_{y,TC}r}{h} = (2 \times 0.001604 \times 100)/276$$

$$\boldsymbol{\theta_y = 0.0012 \ rad}$$

$$k_{\theta i} = \frac{M_y}{\theta_y} = \frac{110.4}{0.0012}$$

$$\boldsymbol{k_{\theta i} = 91972 \ kN.m/rad}$$

Elastic Buckling Check of T/C Bars under Compression

The Euler buckling load of a vertical member with a double fixed-end condition under axial compression is calculated with the following formula.

$$P_{cr} = \frac{4 \times \pi^2 \times E_{TC} \times I_{TC}}{r^2}$$

The second moment of area of a single T/C bar is calculated below.

$$I_{TC} = \frac{\pi}{4} \times (R_o^4 - R_i^4) = \frac{\pi}{4} \times (13^4 - 7.5^4) = 19,947 \ mm^4$$

Then, Euler buckling load of a single T/C bar was determined as below.

$$P_{cr} = \frac{4 \times \pi^2 \times E_{TC} \times I_{TC}}{r^2} = \frac{4 \times \pi^2 \times 227247 \times 19947}{100^2} = 17,895 \ kN$$

The axial compressive force on a single T/C bar at the instant when the component PT1 was at the yield point is calculated below with an inverse procedure.

$$M_y = n_{TC} \times F_y \times h$$

$$M_y = 3 \times F_y \times 0.276 = 110.4 \ kN.m$$

$$F_y = 133 \ kN$$

The yield capacity is also equal to $A_{TC} \times f_{y,TC}$ in confirmation. Note that the axial yielding capacity of a single T/C bar, i.e., 133 kN, is far less than the buckling capacity, less than 1%. Hence, T/C bars do not buckle before yielding in compression.

3.3.2   PT1 Tests

View of test setup and PT1, and instrumentation are presented in Figure 3.6 and displacement protocol that was used during the test is presented in Figure 3.7. Moment-rotation relationship obtained during the test and observed deformations are given in Figure 3.8 and Figure 3.9, respectively. Permanent deformations and damages on the prototype are given in Figure 3.10.
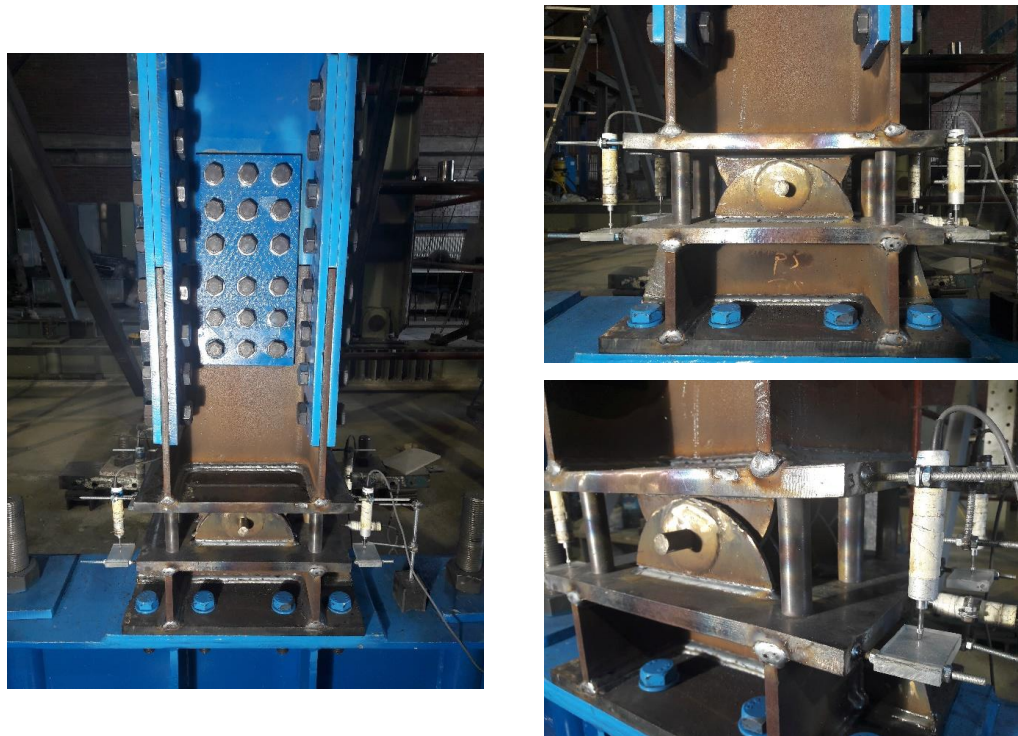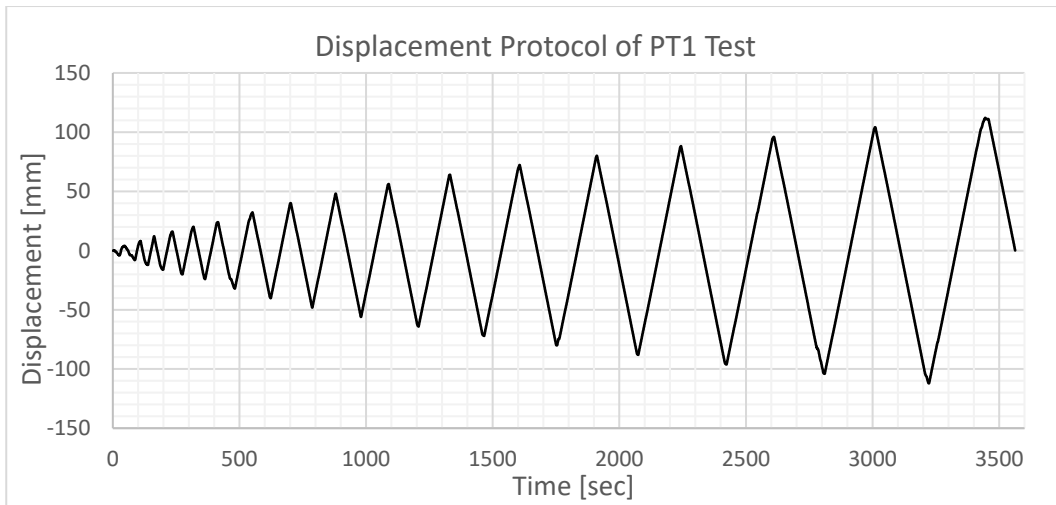

Figure 3.6: View and instrumentation of PT1
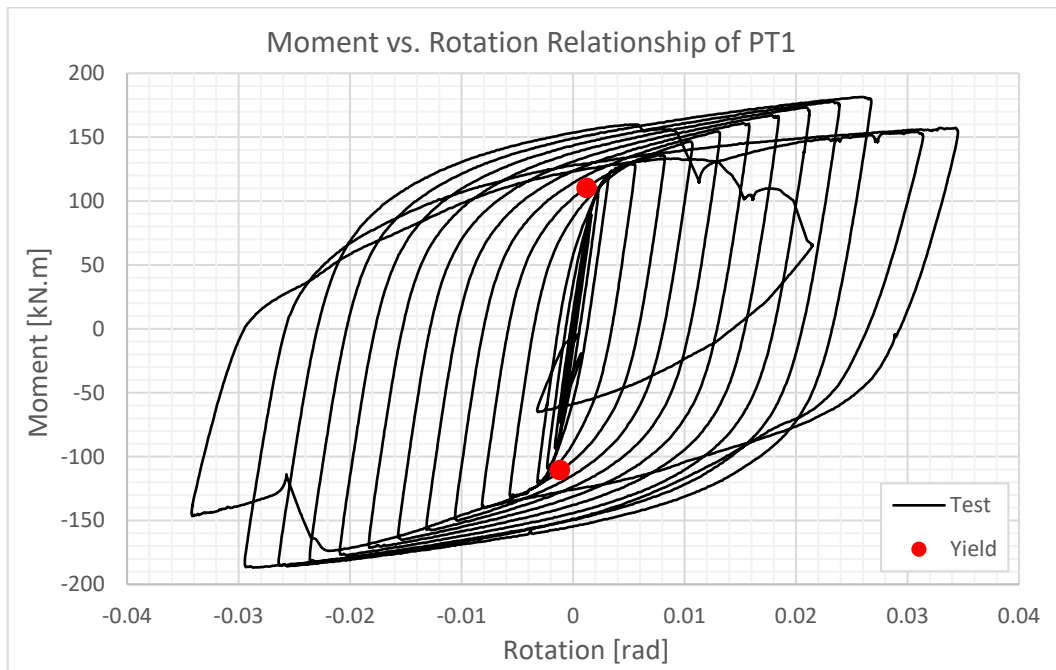
Figure 3.7: Displacement protocol of PT1 test
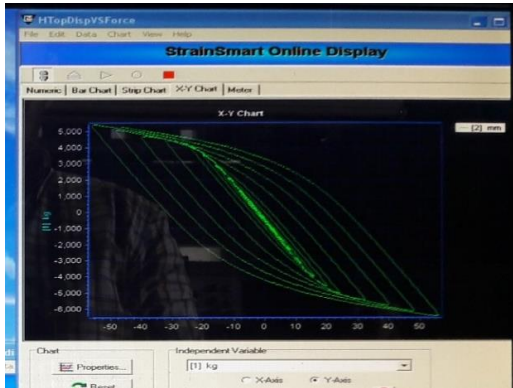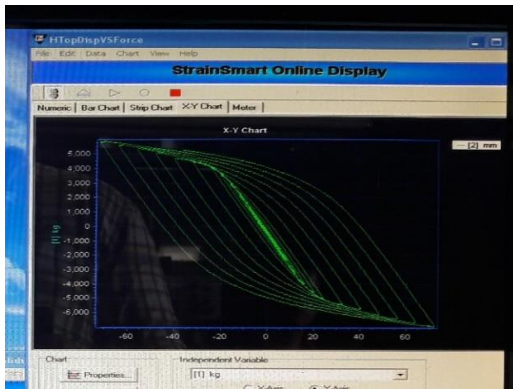

Figure 3.8: Moment-rotation relationship obtained during PT1 Test

Top Displacement: 56 mm   **P-Cell Rotation: 0.0132 rad**

Top Displacement: 72 mm   **P-Cell Rotation: 0.0184 rad**

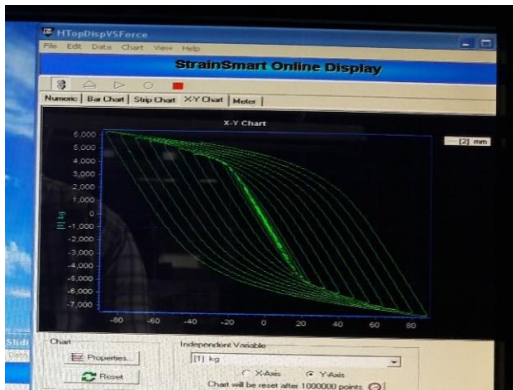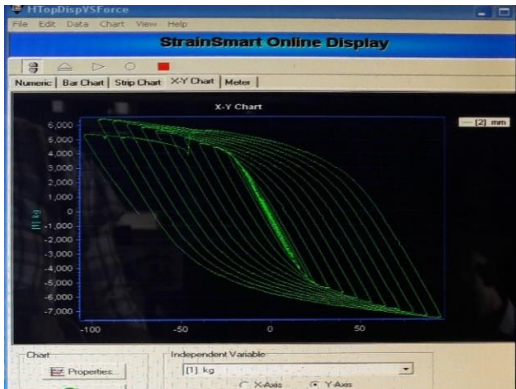Top Displacement: 88 mm   **P-Cell Rotation: 0.0239 rad**

Figure 3.9: Observed deformations on PT1 during Test #1 at different top displacement levels

Top Displacement: 100 mm   **P-Cell Rotation: 0.0268 rad**

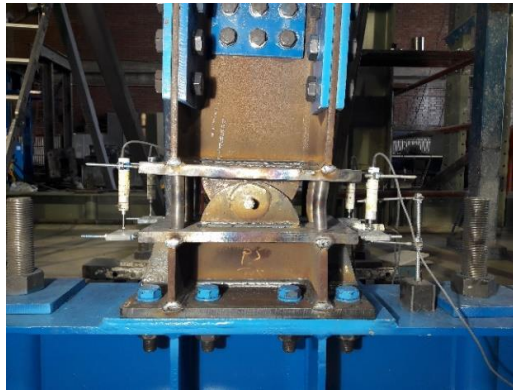Top Displacement: 112 mm   **P-Cell Rotation: 0.0345 rad**
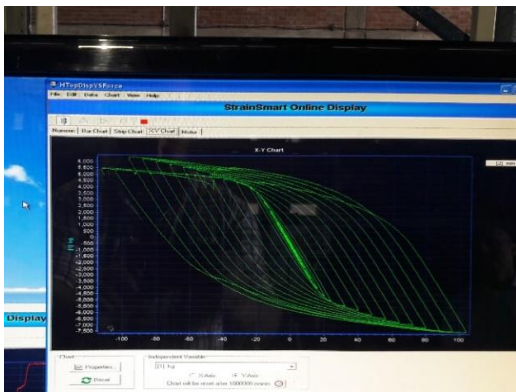

Figure 3.9 (cont'd)

Figure 3.10: Permanent deformations and rupture of T/C bars after Test #1

Regarding the experimental moment-rotation relationship in Figure 3.8, theoretical yield moment is obtained fairly accurately, however theoretical yield curvature seems less than the experimental value. One reason can be the low cycle fatigue effect. This point is reached by 4 number of full cycles during the test. Further, the ratio of the observed ultimate moment capacity (186.6 kN.m) to the theoretical yield moment is about 1.69, which is the apparent overstrength. This ratio should be taken into account in the capacity design of the connecting members.

Test #1, which was performed on PT1, revealed that welding is one of the most critical features that should be paid great attention in the design of the P-Cell. The failure of the specimen at approximately 0.03 radians was a result of premature welding rupture at the bar ends. The welding region at T/C bar ends are not only subjected to tension but bending as well, which increases the tensile stresses on the welding material significantly.

The results of PT1 suggested the revision of T/C bar designs so that the welding regions will be subjected to lower stresses, and they remain as far away from the maximum plastic deformation regions (designated as the mid-sections) as possible. It was then decided that tapered section T/C bars should be designed so that yielding, plastic behavior and a probable rupture would occur at the mid sections which are away from the welding zones at the bar ends. A tapered section at the bar ends also increases the welding area, hence reduces tensile stresses on the welds.

3.4   PT2A: P-Cell with Hollow Section, Tapered T/C Bars

PT2A is the prototype having the first major revision in terms of design, manufacturing, and behavior under reversed cyclic loading. Geometric properties of PT2A are shown in Figure 3.11.
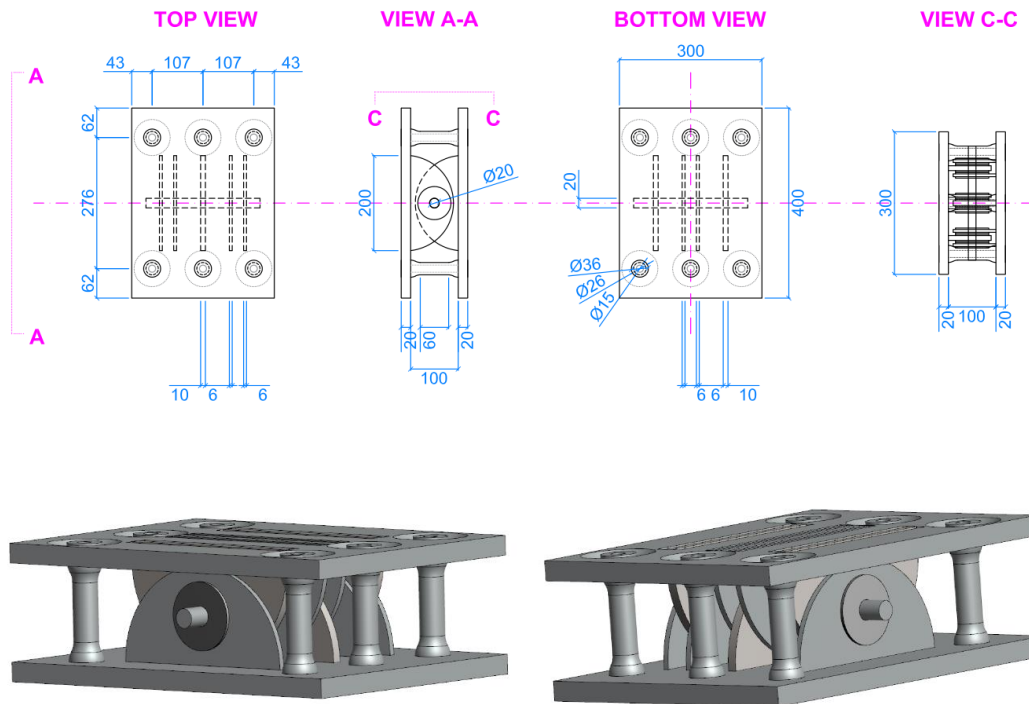
Figure 3.11: 2D and 3D views of PT2A. Dimensions in mm.

3.4.1 Design Calculations of PT2A

The design of PT2A follows the same procedure introduced in Section 3.2. Besides, the geometrical parameter is the same as PT1, apart from T/C bars, which determines the performance and behavior of the P-Cell unit. Therefore, the design calculations of PT2a are presented in this section with all the steps, some of them are repeated for convenience.

P-Cell type PT2A is comprised of two 20-mm thick backing plates, whose dimensions suit the beam section size, designed with HEA300 steel profile. T/C bars were also placed in a way that the centerlines of T/C bars coincided with the centerline of flanges of H-section so that the tensile and compressive forces would be transferred without any eccentricity. The number of T/C bars were selected

considering redundancy in case of rupture during the advanced stages of testing. The material class of T/C bars were selected to have the desired yield and ultimate moment capacities expected during the tests. In the light of the discussion above, the parameters related to the design formulation and the results are given below.

The outer and inner diameter of the hollow section tapered T/C bars in the middle region, where the deformation is designated to occur, were 26 mm and 15 mm, respectively. The total length of the bars was 100 mm whereas the clear length of the bars between the curvatures of tapers at both ends was 60 mm, in which the deformation under compressive and tensile forces was expected to happen. Three bars were used at each side of PT2A, in the same manner as PT1.

$$A_{TC} = n_{TC} \times \frac{\pi}{4} \times (D_o^2 - D_i^2) = 3 \times \frac{\pi}{4} \times (26^2 - 15^2)$$
$$= 1062.6 \ mm^2$$

The steel class of the T/C bars remained as S355. The coupon test results gave the following mean mechanical properties of the T/C bars.

$$f_{y,TC} = 379.5 \ MPa, \quad \varepsilon_{y,TC} = 0.001791, \quad E_{TC} = 211860 \ MPa$$

As a result, the design parameters of PT2a were calculated as follows.

$$M_y = A_{TC} \times f_{y,TC} \times h = 1062.6 \times 379.5 \times 276$$
$$\boldsymbol{M_y = 111.3 \ kN.m}$$

$$\theta_y = \frac{2\varepsilon_{y,TC}r}{h} = (2 \times 0.001791 \times 60)/276$$
$$\boldsymbol{\theta_y = 0.00078 \ rad}$$

$$k_{\theta i} = \frac{M_y}{\theta_y} = \frac{111.3}{0.00078}$$
$$\boldsymbol{k_{\theta i} = 142908 \ kN.m/rad}$$

Elastic Buckling Check of T/C Bars under Compression

The Euler buckling load of a vertical member with a double fixed-end condition under axial compression is calculated with the following formula.

$$P_{cr} = \frac{4 \times \pi^2 \times E_{TC} \times I_{TC}}{r^2}$$

The second moment of area of a single T/C bar is calculated below.

$$I_{TC} = \frac{\pi}{4} \times (R_o^4 - R_i^4) = \frac{\pi}{4} \times (13^4 - 7.5^4) = 19947 \; mm^4$$

Then, Euler buckling load of a single T/C bar was determined as below.

$$P_{cr} = \frac{4 \times \pi^2 \times E_{TC} \times I_{TC}}{r^2} = \frac{4 \times \pi^2 \times 211860 \times 19947}{60^2} = 46342 \; kN$$

The axial compressive force on a single T/C bar at the instant when the component PT2a was at the yield point is calculated below.

$$M_y = n_{TC} \times F_y \times h = 111.3 \; kN.m$$

$$M_y = 3 \times F_y \times 0.276 = 111.3 \; kN.m$$

$$F_y = 134 \; kN$$

Note that the axial yielding capacity of a single T/C bar is 134 kN, which is far less than the buckling capacity, less than 0.5%. Hence, T/C bars do not buckle before yielding in compression.

3.4.2   PT2A Test

View of test setup with PT2A, and instrumentation are presented in Figure 3.12, and displacement protocol used during the test is given in Figure 3.13. Moment-rotation relationship obtained during the PT2A Test and observed deformations are given in

Figure 3.14 and Figure 3.15, respectively. Permanent deformations and damages on the P-Cell component are shown in Figure 3.16.
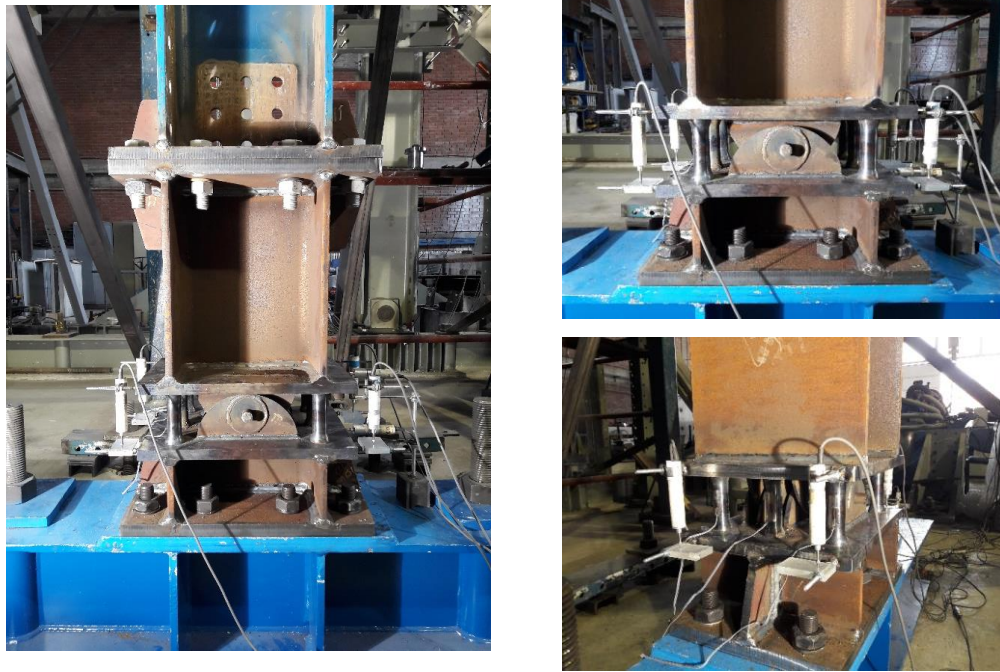

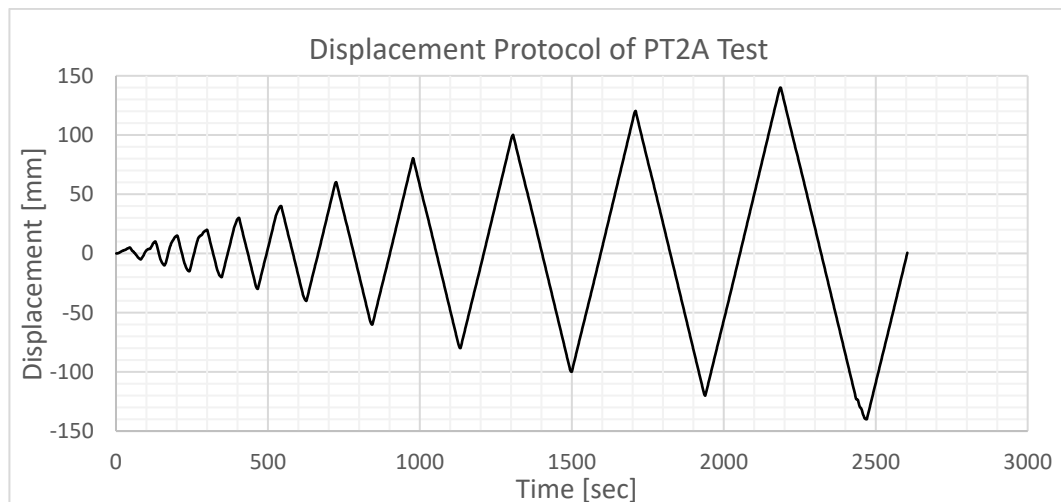Figure 3.12: View and instrumentation of PT2A
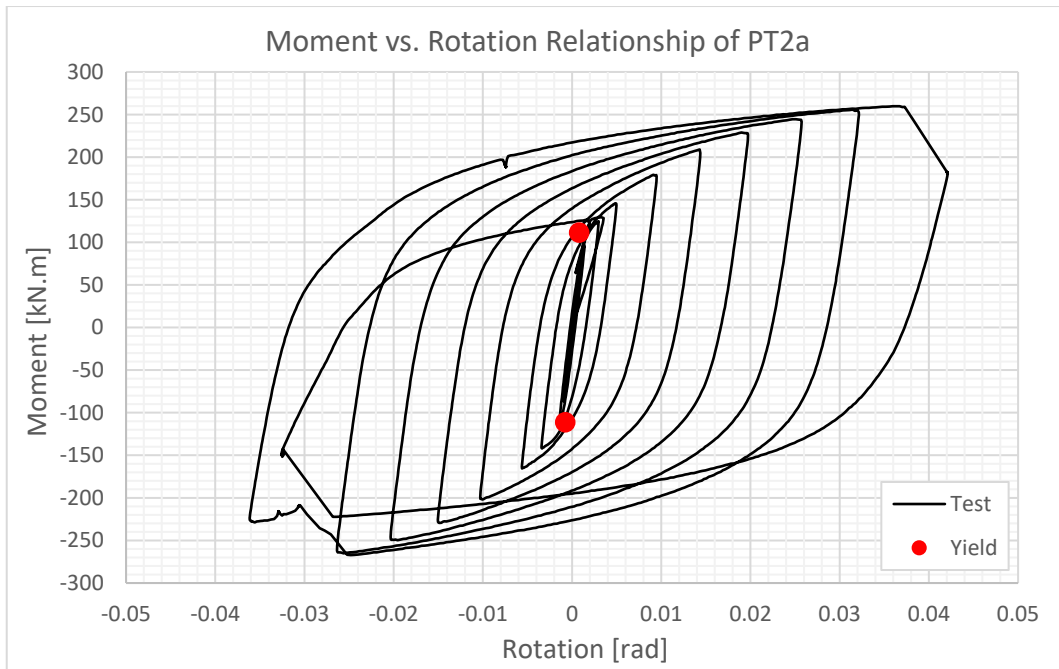

Figure 3.13: Displacement protocol of PT2A test

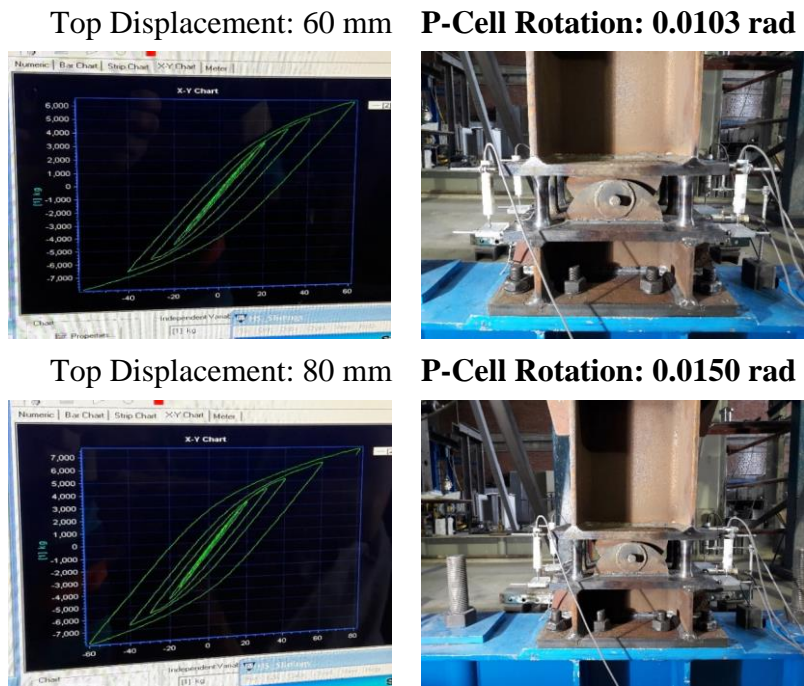Figure 3.14: Moment-rotation relationship obtained during PT2A test

Top Displacement: 60 mm **P-Cell Rotation: 0.0103 rad**

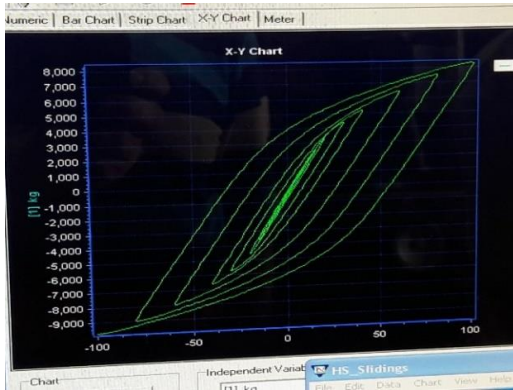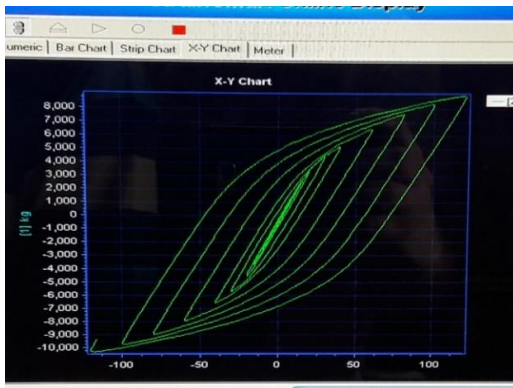Top Displacement: 80 mm **P-Cell Rotation: 0.0150 rad**

Figure 3.15: Observed deformations during PT2A Test at different top
displacement levels

Top Displacement: 100 mm **P-Cell Rotation: 0.0203 rad**

Top Displacement: 120 mm **P-Cell Rotation: 0.0263 rad**

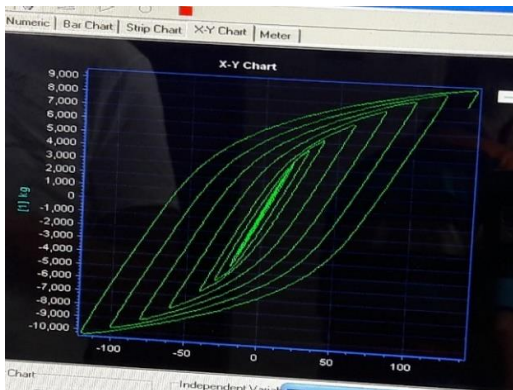Top Displacement: 140 mm **P-Cell Rotation: 0.0361 rad**

Figure 3.15 (cont'd)

Figure 3.16: Permanent deformations and damages after PT2A Test

It was observed that ruptures as a result of exceeding the strain capacity of steel T/C bars (and rotation capacity of P-Cell) occurred at the desired locations of P-Cells. As seen in Figure 3.16, ruptures occurred at the mid-sections of T/C bars in both directions. However, moment-rotation relationship in Figure 3.14 revealed that there was no significant increase in the rotation capacity of the P-Cells even though T/C bars exhibited the desired plastic behavior. Non-synchronized yielding of the T/C bars leading to torsional rotation along the P-Cell section is the main reason for limited increase in rotation capacity. The ratio of the observed ultimate moment capacity (267.2 kN.m) to the theoretical yield moment is about 2.4, which is the overstrength that was observed 50% higher than that of PT1.

3.5   PT2B: P-Cell with Hollow Section, Tapered, Replaceable T/C Bars

Test #3 was performed on PT2B, on which the second major revision of the development of P-Cell was implemented. The main revision was that the region on the P-Cell where T/C bars connect to the backing plates and work under reversed cyclic loading was completely changed, while the main reason for this change was to achieve a replaceable T/C bar arrangement. That replaceable system includes T/C bars welded to the adapter plates and in turn connected to backing plates with bolts via adapter plates. The geometry of the drums was also significantly changed since

88

the adapter plates that are used in replaceable T/C bars occupied a larger space, as compared with sole T/C bar configurations. Therefore, the width of drums was decreased by %30. Relevant information on PT2B is given in Figure 3.17 and PT2B Test information, results and observations are subsequently presented.
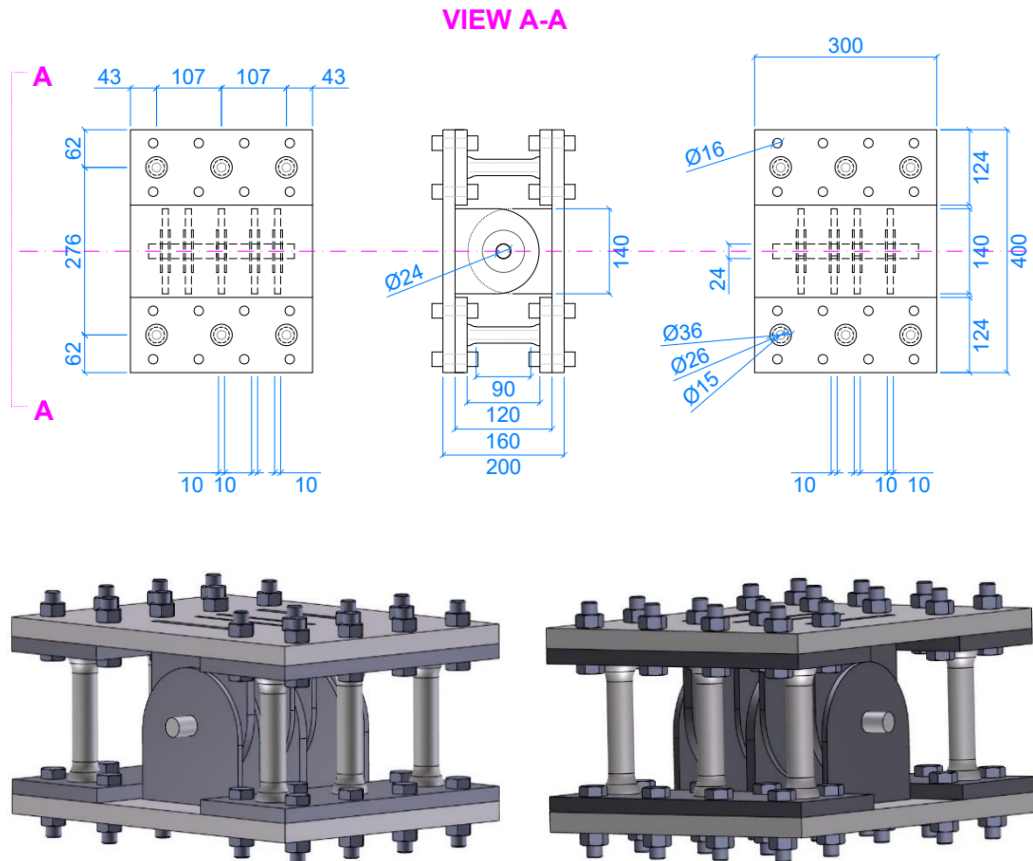

Figure 3.17: 2D and 3D drawings of PT2B. Dimensions in mm.

3.5.1 Design Calculations of PT2B

The outer and inner diameter of the hollow section T/C bars were 26 mm and 15 mm, respectively. The clear length of the bars, which has a total length of 120 mm, was 90 mm, where three bars were used at each side of PT2A.

$$A_{TC} = n_{TC} \times \frac{\pi}{4} \times (D_o^2 - D_i^2) = 3 \times \frac{\pi}{4} \times (26^2 - 15^2)$$
$$= 1062.6 \; mm^2$$

T/C bars were manufactured from the same steel as used in the manufacturing of the T/C bars of PT2a. Therefore, the mechanical properties of the T/C bars were identical to the T/C bars of PT2a. The values are presented in the following steps for convenience.

$$f_{y,TC} = 379.5 \; MPa, \quad \varepsilon_{y,TC} = 0.001791, \quad E_{TC} = 211860 \; MPa$$

As a result, the design parameters of PT2a were calculated as follows.

$$M_y = A_{TC} \times f_{y,TC} \times h = 1062.6 \times 379.5 \times 276$$
$$\boldsymbol{M_y = 111.3 \; kN.m}$$

$$\theta_y = \frac{2\varepsilon_{y,TC} r}{h} = (2 \times 0.001791 \times 90)/276$$
$$\boldsymbol{\theta_y = 0.00117 \; rad}$$

$$k_{\theta i} = \frac{M_y}{\theta_y} = \frac{111.3}{0.00117}$$
$$\boldsymbol{k_{\theta i} = 95272 \; kN.m/rad}$$

Elastic Buckling Check of T/C Bars under Compression

The Euler buckling load of a vertical member with a double fixed-end condition under axial compression is calculated with the following formula.

$$P_{cr} = \frac{4 \times \pi^2 \times E_{TC} \times I_{TC}}{r^2}$$

The second moment of area of a single T/C bar is calculated below.

$$I_{TC} = \frac{\pi}{4} \times (R_o^4 - R_i^4) = \frac{\pi}{4} \times (13^4 - 7.5^4) = 19947 \; mm^4$$

Then, Euler buckling load of a single T/C bar was determined as below.

$$P_{cr} = \frac{4 \times \pi^2 \times E_{TC} \times I_{TC}}{r^2} = \frac{4 \times \pi^2 \times 211860 \times 19947}{90^2} = 20597 \; kN$$

The axial compressive force on a single T/C bar at the instant when the component PT2b was at the yield point is calculated below.

$$M_y = n_{TC} \times F_y \times h = 111.3 \; kN.m$$

$$M_y = 3 \times F_y \times 0.276 = 111.3 \; kN.m$$

$$F_y = 134 \; kN$$

Note that the axial yielding capacity of a single T/C bar is 134 kN, which is far less than the buckling capacity, less than 1%. Hence, T/C bars do not buckle before yielding in compression.

3.5.2   PT2B Test

View of test setup with PT2B, and instrumentation are presented in Figure 3.18, while displacement protocol that was used during PT2B test is given in Figure 3.19. Moment-rotation relationships obtained during the PT2B Test, and observed deformations are presented in Figure 3.20 and Figure 3.21, respectively. Permanent deformations and damages on the prototype are shown in Figure 3.22.
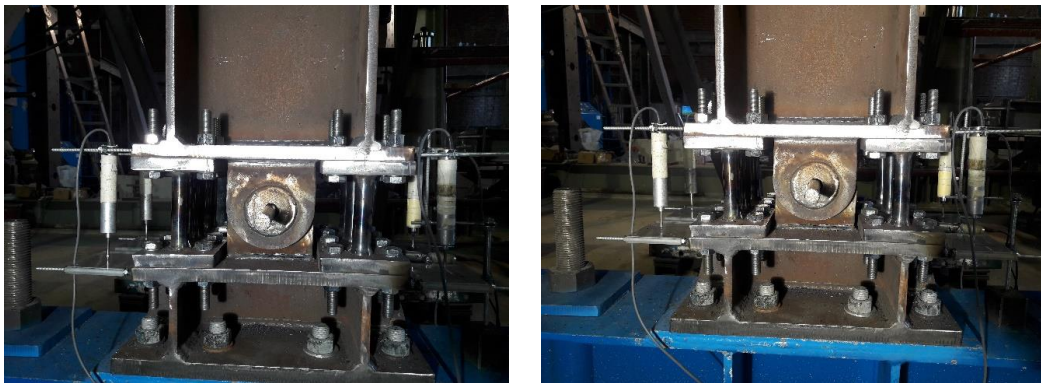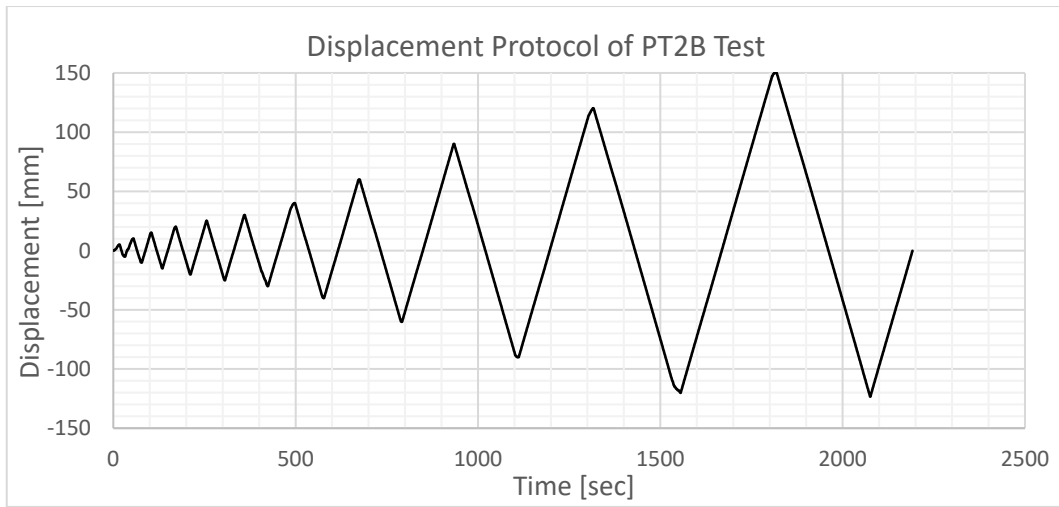

Figure 3.18: View and instrumentation of PT2B test
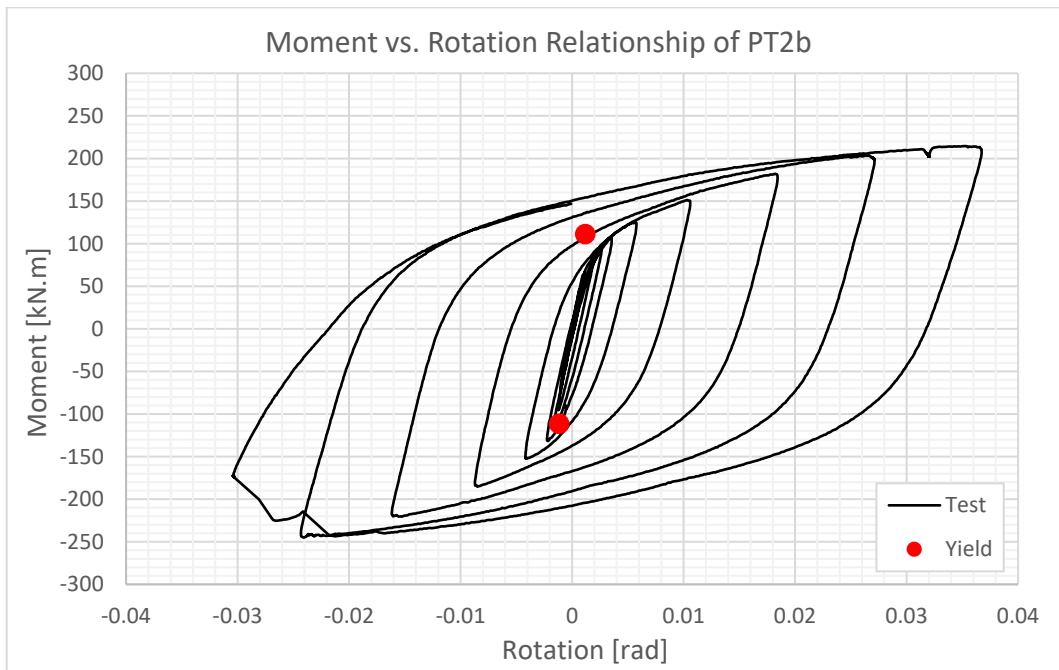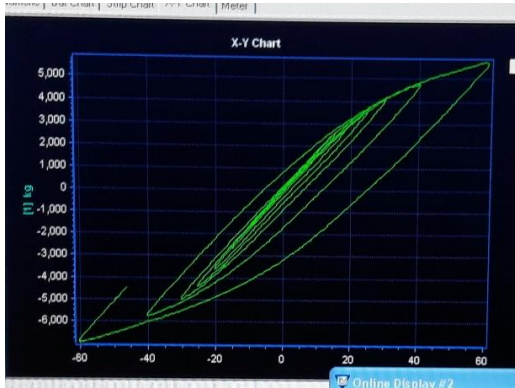
Figure 3.19: Displacement protocol of PT2B test

Figure 3.20: Moment-rotation relationship obtained during the PT2B Test

Top Displacement: 60 mm **P-Cell Rotation: 0.0106 rad**

Top Displacement: 90 mm **P-Cell Rotation: 0.0184 rad**
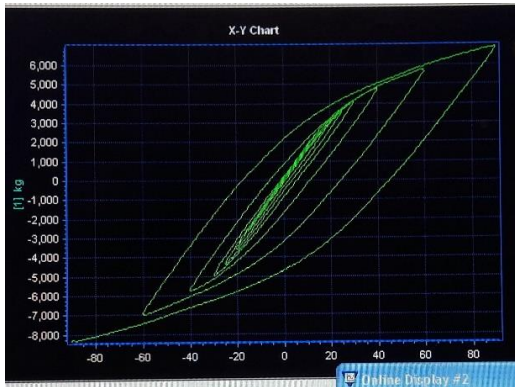
Top Displacement: 120 mm **P-Cell Rotation: 0.0271 rad**

Figure 3.21: Observed deformations during PT2B Test at different top displacement levels

Top Displacement: 150 mm   **P-Cell Rotation: 0.0367 rad**

Figure 3.21 (cont'd)

Figure 3.22: Permanent deformations and damages after PT2B Test

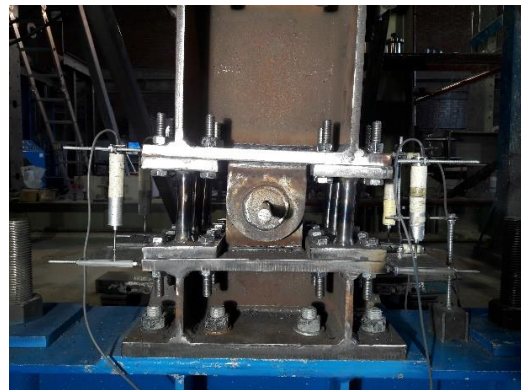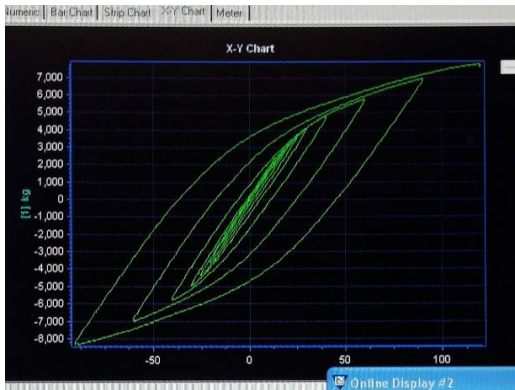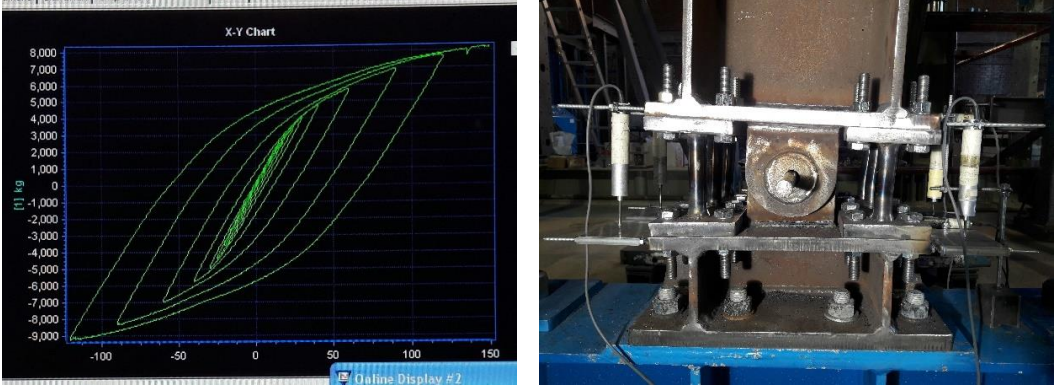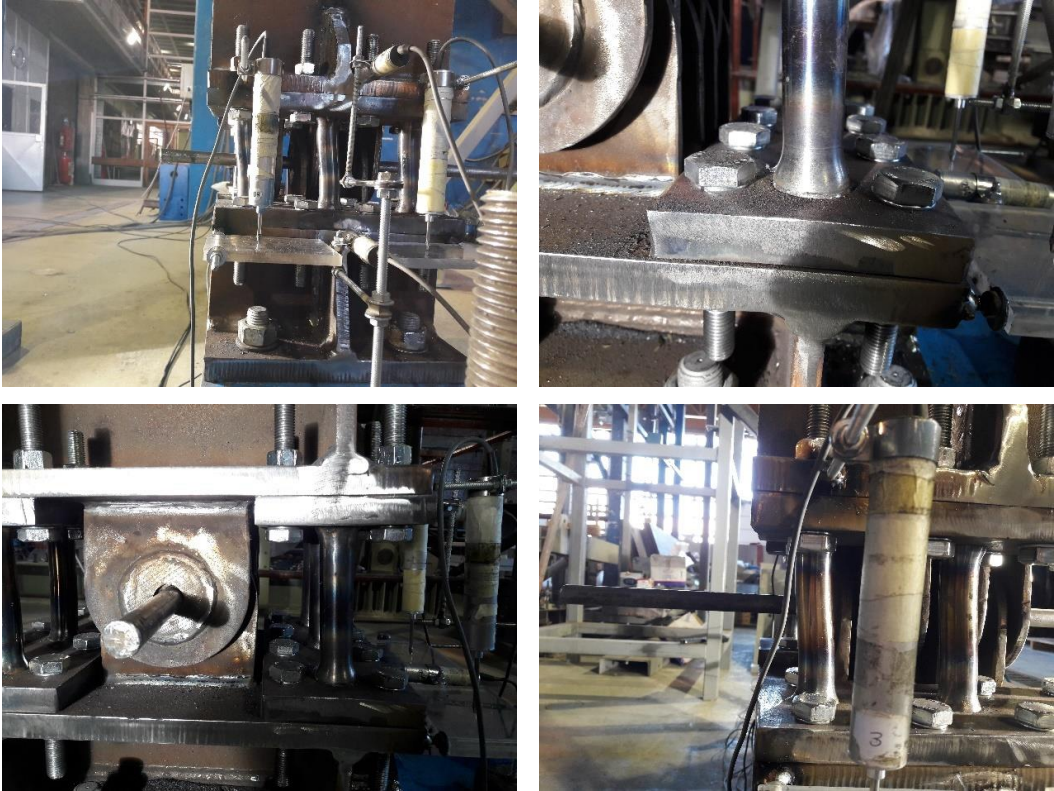The results of the PT2B Test and the behavior of P-Cell during the test revealed that PT2B also has a torsional behavior problem. Figure 3.20 shows that the rotation capacity can attain a value close to 0.036 rad, which is a considerably high design value. However, during high rotation demands, such as beyond 0.02 rad, P-Cells started to exhibit torsion about the axis normal to backing plates and perpendicular to the axis of rotation, and T/C bars were subjected to biaxial double-curvature bending while they are under compression. The described behavior can be observed clearly in Figure 3.23. This situation caused T/C bars to dissipate some of their strain capacities and rupture slightly earlier than expected. Rupture occurred at the weld regions of T/C bars in PT2B Test can be seen in Figure 3.22. The rupture did not occur at the desired location, which is the middle region of T/C bars, and the rotations did not reach the desired values.

Figure 3.23: Observed torsional behavior on PT2B

The results obtained from Test #3 performed on PT2B state that while the concept of replaceable T/C members supplying considerable rotation capacity to the P-Cell is achieved, observed torsional behavior issue prevents the P-Cell from exhibiting desired rotation levels and performance targets, and causes a source of unpredictable failure level.

3.6   PT3: P-Cell with an I-Section as the T/C Component

Section 3.5 where the design and testing of PT2B was presented, has been concluded by presenting the torsional behavior observed during the rotation reversals, especially beyond the rotations of 0.02 rad. In addition to the observed rotation capacities around 0.036 rad, which is less than the performance objective of a P-Cell, this torsional behavior, resulting deformations and probable loss of capacity created a handicap in the performance of such a device. Therefore, it was aimed at preventing the torsional behavior in the following P-Cell type, as well as increasing its rotation capacity. For that purpose, the configuration of the plastic energy dissipating T/C components in the P-Cell changed completely so that they would introduce sufficient lateral, and therefore, torsional stiffness during load reversals. To this end, PT3 was developed as the first P-Cell prototype having I- or H-section steel profiles as the energy dissipating T/C components.

There are several considerations for the selection and dimensioning of steel profiles, as summarized below.

1. It was not desired to change the general dimensions of P-Cell, mainly its outer height and plate dimensions since P-Cell dimension changes would cause a change in the test setup that would require extra (and unnecessary) workmanship and material procurement.

2. It was decided to keep the total cross section area of T/C members fixed to deal with the same compression and tension capacity for having similar moment capacity at the advanced stages of prototype tests.

3. The availability of readily manufactured steel members in the open market was considered, in order not to waste unnecessary time obtaining the materials.

The next two sections consist of the calculations of lateral and torsional stiffness during the selection of T/C components and subsequently the design calculations of PT3.

3.6.1 Stiffness Check with an I-Section as a T/C Component

The arrangement of IPE section in the P-Cell as a T/C component, and its cross sectional dimensions are presented in Figure 3.24.

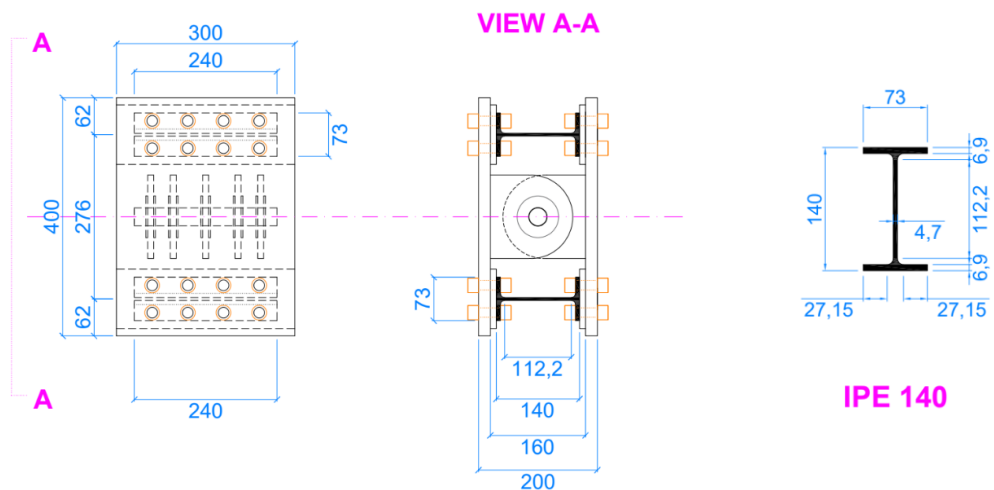Figure 3.24: Dimensions of IPE140 in mm.

The lateral stiffness of T/C components, which is introduced to the P-Cell, is determined by considering its web section in its strong axis, and the clear length of its web, where all the related dimensions are presented in Figure 3.24.

The second moment of area of a T/C component by considering the strong axis of web section of IPE 140 is calculated below.

$$I_{TC} = \frac{1}{12} bL^3$$

In this equation, b corresponds to the web thickness of IPE 140 section, whereas L corresponds to the length of T/C component, which are 4.7 mm and 240 mm, respectively.

$$I_{TC} = \frac{1}{12} bh^3 = \frac{1}{12} \times 4.7 \times 240^3 = 5.414e^6 mm^4$$

$$E = 210,000 MPa$$

$$EI_{TC} = 210,000 \times 5.414e^6 = 1.137e^{12} N. mm^2$$

$$k_{TC} = \frac{12EI}{h_{TC}^3} = \frac{12 \times 1.137e^{12}}{112.2^3} = 9,659,179 N/mm$$

Total lateral stiffness introduced by T/C components

$$k_{TC,Total} = 2 \times k_{TC} = 2 \times 9,659,179$$
$$k_{Total} = 19,318,358 \ N/mm$$

The torsional stiffness of P-Cell introduced by T/C components

$$k_{\theta\theta} = 2 \times k_{TC} \times \left(\frac{d_{Bar}}{2}\right)^2$$
$$k_{\theta\theta} = 2 \times 9,659,179 \times (276/2)^2$$
$$k_{\theta\theta} = 2.666e^9 \ N. mm/rad$$
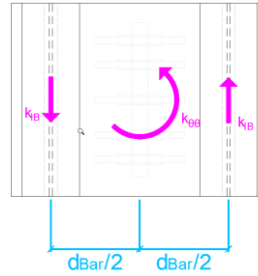
3.6.2 Design Calculations of PT3

The previous section, where the lateral and torsional stiffness of IPE 140 members as T/C components were determined, also presented the primary dimensions of T/C components. The dimensions of PT3 are also presented in the next section, in Figure 3.25.

The cross-sectional dimensions of T/C components were 4.7x240 mm whereas the clear length of the component between the flanges of the IPE 140, where the deformation was expected, is 112.2 mm. In each side of the PT3, one T/C component was used.

$$A_{TC} = n_{TC} \times = 1 \times (4.7 \times 240) = 1128 \; mm^2$$

The steel class of the T/C bars were selected as S275 therefore the following mechanical properties were considered in the design of PT3.

$$f_{y,TC} = 275 \; MPa, \quad \varepsilon_{y,TC} = 0.00131, \quad E_{TC} = 210000 \; MPa$$

As a result, the design parameters of PT3 were calculated as follows.

$$M_y = A_{TC} \times f_{y,TC} \times h = 1128 \times 275 \times 276$$
$$\boldsymbol{M_y = 85.6 \; kN.m}$$

$$\theta_y = \frac{2\varepsilon_{y,TC}r}{h} = (2 \times 0.00131 \times 112.2)/276$$
$$\boldsymbol{\theta_y = 0.00106 \; rad}$$

$$k_{\theta i} = \frac{M_y}{\theta_y} = \frac{85.6}{0.00106}$$
$$\boldsymbol{k_{\theta i} = 80413 \; kN.m/rad}$$

Elastic Buckling Check of T/C Component under Compression

Elastic buckling check of T/C component of PT3 under compression is done by considering the web of T/C component exhibit a thin plate behavior, rather than column behavior observed in PT1, PT2A and PT2B. Therefore, it is accepted that biaxial stresses occur both in the direction of loading and orthogonal direction, whereas strain occurs only in the direction of loading. Consequently, the Euler

buckling load of a wide, thin plate with a double fixed-end condition under axial compression is calculated with the following formula. (Rees, 2009)

$$P_{cr} = \frac{4 \times \pi^2 \times E_{TC} \times I_{TC}}{(1 - v^2) \times r^2}$$

The Poisson's ratio, denoted as v in the Euler buckling load equation above, is taken as 0.3 for mild steel material.

The second moment of area of a T/C component is calculated below. Note that it is determined by considering the behavior is governed by its weak axis.

$$I_{TC} = \frac{1}{12} bh^3 = \frac{1}{12} \times 240 \times 4.7^3 = 2,076.5 mm^4$$

Then, Euler buckling load of a T/C component was determined as below.

$$P_{cr} = \frac{4 \times \pi^2 \times E_{TC} \times I_{TC}}{(1 - v^2) \times r^2} = \frac{4 \times \pi^2 \times 210000 \times 2076.5}{(1 - 0.3^2) \times 112.2^2} = 1502.7\ kN$$

The axial compressive force on a T/C component at the instant when the component PT3 was at the yield point is calculated below.

$$M_y = n_{TC} \times F_y \times h = 85.6\ kN.m$$

$$M_y = 1 \times F_y \times 0.276 = 85.6\ kN.m$$

$$F_y = 310.2\ kN$$

Note that the elastic buckling load is 1502.7 kN whereas the axial yielding capacity of one T/C component is 310.2 kN, which is approximately 21% of the buckling load. Hence, it was concluded that T/C components do not buckle before yielding in compression.

3.6.3   PT3 Test

2D drawings of PT3, view of test setup, and instrumentation are presented in Figure 3.25 and Figure 3.26, respectively. Displacement protocol utilized during the test is presented in Figure 3.27. Moment-rotation relationship obtained during the PT3 Test, and the observed deformations are given in Figure 3.28 and Figure 3.29, respectively. Permanent deformations and damages on the prototype are shown in Figure 3.30.
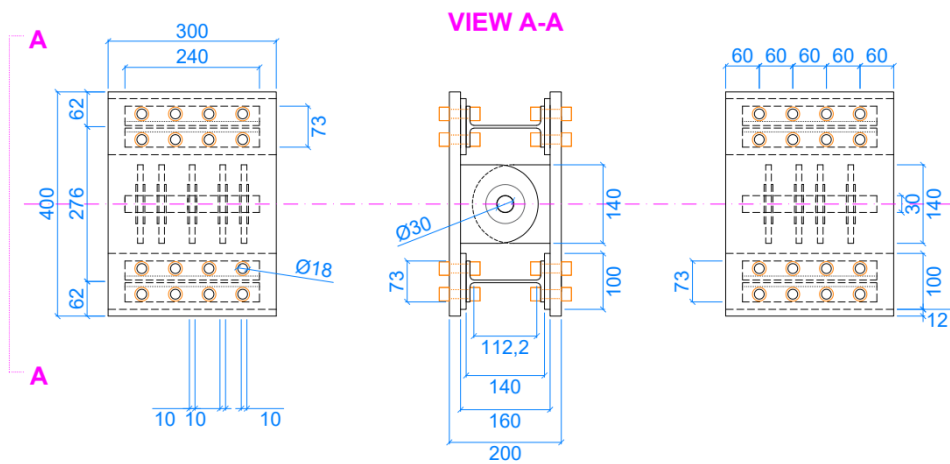

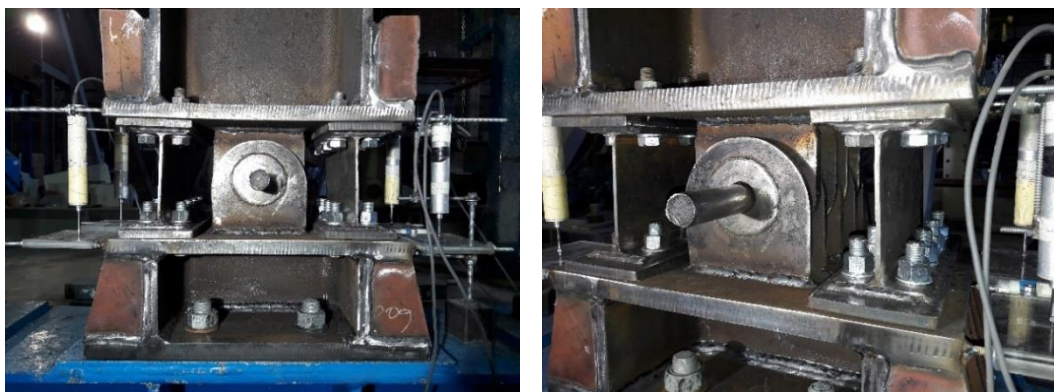Figure 3.25: 2D drawings of PT3. Dimensions in mm.

Figure 3.26: General view and instrumentation of PT3
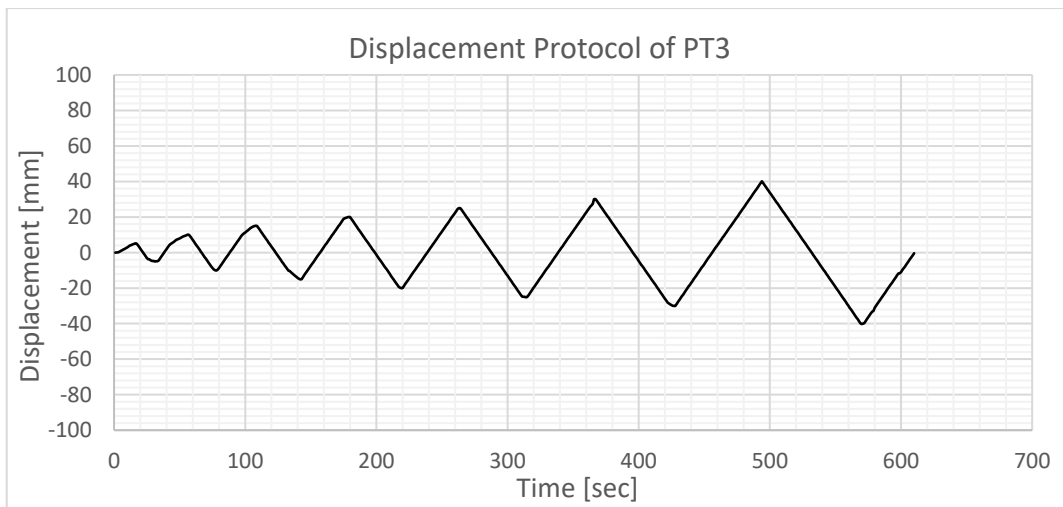
Figure 3.27: Displacement protocol of PT3 test
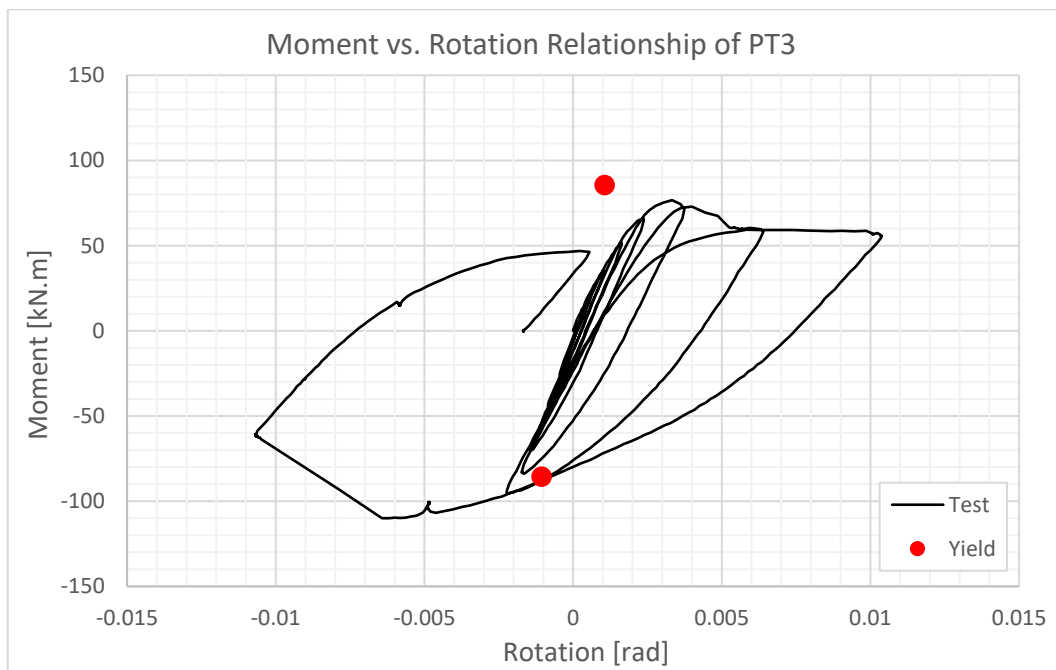
Figure 3.28: Moment-rotation relation obtained during the PT3 Test

Top Displacement: 20 mm **P-Cell Rotation: 0.0024 rad**

Top Displacement: 30 mm **P-Cell Rotation: 0.0064 rad**

Top Displacement: 40 mm **P-Cell Rotation: 0.0137 rad**
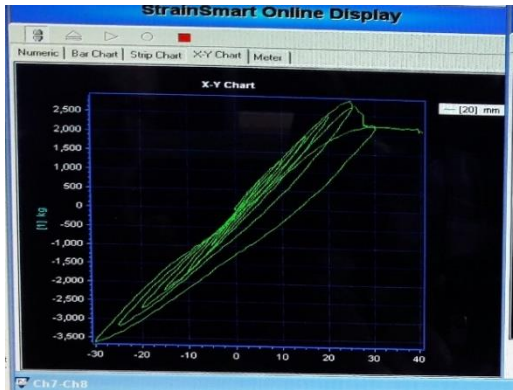
Figure 3.29: Observed deformations during PT3 Test at different top displacement levels

Figure 3.30: Permanent deformations and damages after PT3 Test

It was stated in the calculations that T/C components manufactured from I-section steel profile members have much greater lateral stiffness capacity that increases torsional stiffness of P-Cell sig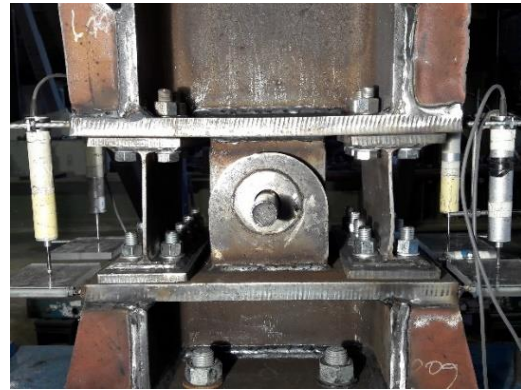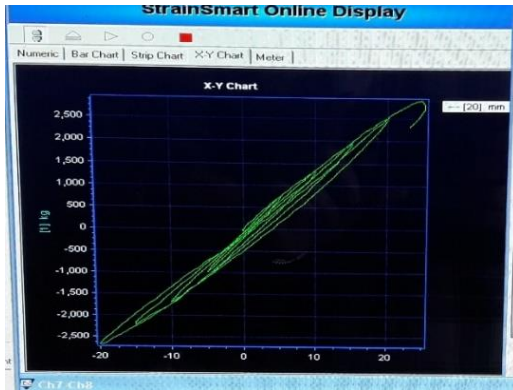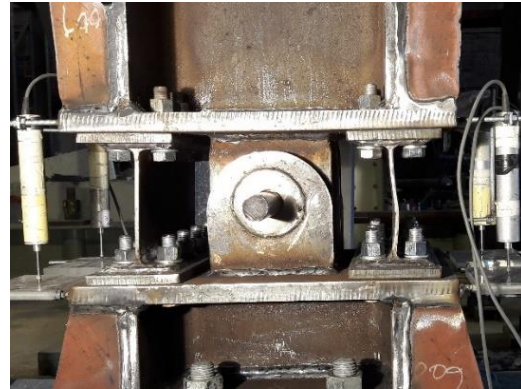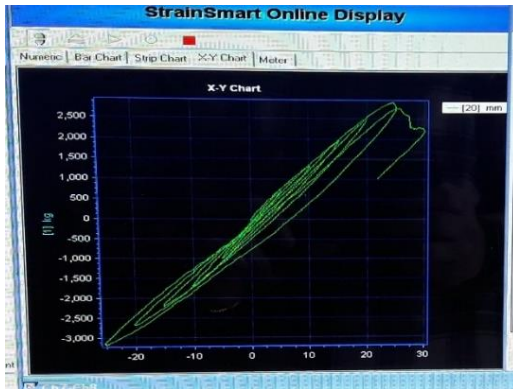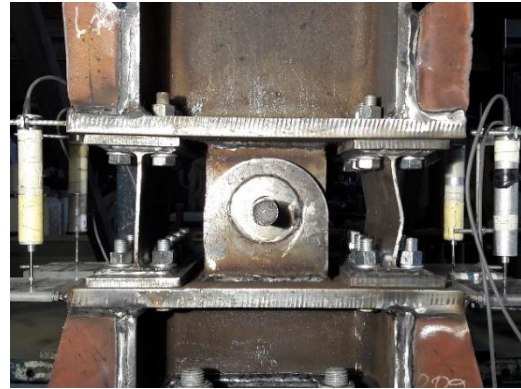nificantly. The first test was performed on a prototype having a light and adequate T/C component (IPE140) having the same tensile force capacity as the previous members. However, it was observed during the test that the components buckled prematurely. Buckling occurred just after the point where post-yield behavior started in the previous tests, possibly exceeding inelastic buckling load. At this point, the test was stopped since there would be no capacity to dissipate energy by deforming under tensile-compressive forces.

After the test, it was evident that if any steel profile were used as a T/C component, it would be inevitable to take precautions against inelastic buckling at the advanced stages of reversed cyclic loading. It was determined after discussions and study that the most suitable and easy-to apply solution for preventing buckling would be placing buckling-restraint plates (BRP) at both faces of the web of I- or H-section steel members/profiles.

3.7 PT4: P-Cell with Buckling-Restrained H-Section as the T/C Component

PT4 is the final P-Cell unit that was developed and tested in the scope of the thesis study. As discussed in the previous section, the unit is the P-Cell with T/C components having buckling-restrained plates at both ends of the components. Each T/C component is connected to the end plates of the connecting member-ends via an adapter plate as shown in Figure 3.32. The design calculations and checks of the P-Cell unit and T/C components are presented in the subsequent sections. The test results and discussions follow afterwards.

3.7.1 Stiffness Check with an H-Section as the T/C Component

The arrangement of HEA 140 section to the P-Cell as a T/C component, and cross sectional dimensions are presented in Figure 3.31.
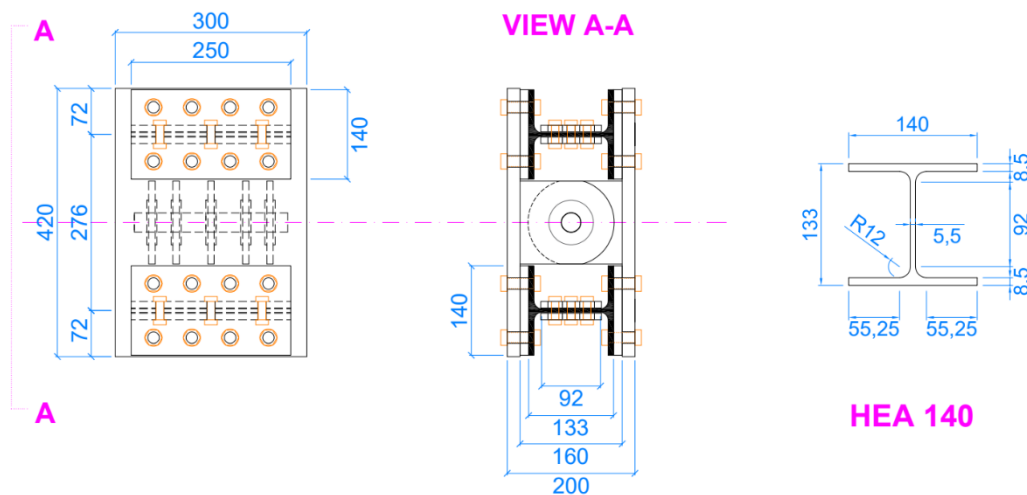
Figure 3.31: Dimensions of HEA 140

The lateral stiffness of T/C components, which is introduced to the P-Cell, is determined by considering its web section along its strong axis, and the clear length of its web, where all the related dimensions are presented in Figure 3.31.

The second moment of area of a T/C component by considering the strong axis of web section of HEA 140 is calculated below.

$$I_{TC} = \frac{1}{12} bL^3$$

In this equation, b corresponds to the web thickness of HEA 140 section, whereas L corresponds to the length of T/C component, which are 5.5 mm and 250 mm, respectively.

$$I_{TC} = \frac{1}{12} bh^3 = \frac{1}{12} \times 5.5 \times 250^3 = 7.161e^6 mm^4$$

$$E = 210,000 MPa$$

$$EI_{TC} = 210,000 \times 7.161e^6 = 1.504e^{12} N.mm^2$$

$$k_{TC} = \frac{12EI}{h_{TC}^3} = \frac{12 \times 1.504e^{12}}{92^3} = 23,176,002 \ N/mm$$

Total lateral stiffness introduced by the T/C components

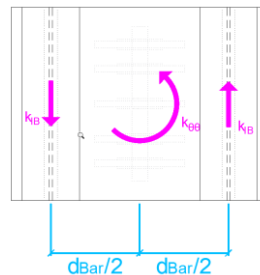$$k_{TC,Total} = 2 \times k_{TC} = 2 \times 23,176,002$$
$$k_{Total} = 46,352,005 \ N/mm$$

The torsional stiffness of P-Cell introduced by T/C components

$$k_{\theta\theta} = 2 \times k_{TC} \times \left(\frac{d_{Bar}}{2}\right)^2$$
$$k_{\theta\theta} = 2 \times 23,176,002 \times (276/2)^2$$
$$k_{\theta\theta} = 6.397e^9 \ N.mm/rad$$

106

3.7.2 Design Calculations of PT4

The previous section, where the lateral and torsional stiffness of HEA 140 members as T/C components were determined, also presented the primary dimensions of T/C components. Besides that, all the dimensions of PT4 are also presented in the next section, in Figure 3.32.

The cross-sectional dimensions of T/C components were 5.5x250 mm whereas the clear length of the component between the flanges of the HEA 140, where the deformation was expected, is 92 mm. In each side of the PT4, one T/C component was used.

$$A_{TC} = n_{TC} \times = 1 \times (5.5 \times 250) = 1375 \ mm^2$$

The steel material of the T/C bars were selected as S275 therefore the following mechanical properties were considered in the design of PT4.

$$f_{y,TC} = 275 \ MPa, \quad \varepsilon_{y,TC} = 0.00131, \quad E_{TC} = 210000 \ MPa$$

As a result, the design parameters of PT4 were calculated as follows.

$$M_y = A_{TC} \times f_{y,TC} \times h = 1375 \times 275 \times 276$$
$$\boldsymbol{M_y = 104.4 \ kN.m}$$

$$\theta_y = \frac{2\varepsilon_{y,TC}r}{h} = (2 \times 0.00131 \times 92)/276$$
$$\boldsymbol{\theta_y = 0.00087 \ rad}$$

$$k_{\theta i} = \frac{M_y}{\theta_y} = \frac{104.4}{0.00087}$$
$$\boldsymbol{k_{\theta i} = 119543 \ kN.m/rad}$$

Elastic Buckling Check of T/C Component under Compression

The method of elastic buckling check was presented in Section 3.6.2. Here, the Euler buckling load of a wide, thin plate with a double fixed-end condition under axial compression is calculated with the same following formula. (Rees, 2009)

$$P_{cr} = \frac{4 \times \pi^2 \times E_{TC} \times I_{TC}}{(1 - v^2) \times r^2}$$

The Poisson's ratio, denoted as v in the Euler buckling load equation above, is taken as 0.3 for mild steel material.

The second moment of area of a T/C component is calculated below. Note that it is determined by considering the behavior is governed by its weak flexural axis.

$$I_{TC} = \frac{1}{12} bh^3 = \frac{1}{12} \times 250 \times 5.5^3 = 3466.1 \; mm^4$$

Then, Euler buckling load of a T/C component was determined as below.

$$P_{cr} = \frac{4 \times \pi^2 \times E_{TC} \times I_{TC}}{(1 - v^2) \times r^2} = \frac{4 \times \pi^2 \times 210000 \times 3466.1}{(1 - 0.3^2) \times 92^2} = 3730.9 \; kN$$

The axial compressive force on a T/C component at the instant when the component PT3 was at the yield point is calculated below.

$$M_y = n_{TC} \times F_y \times h = 104.4 \; kN.m$$

$$M_y = 1 \times F_y \times 0.276 = 104.4 \; kN.m$$

$$F_y = 378.1 \; kN$$

Note that the elastic buckling load is 3730.9 kN whereas the axial yielding capacity of one T/C component is 378.1 kN, which indicates that it is approximately 11% of the buckling load. Hence, it was concluded that T/C components do not buckle before yielding in compression.

3.7.3   PT4 Test

2D drawings of PT4 is presented in Figure 3.32. Production, test setup of PT4, and instrumentation are presented in Figure 3.33, whereas the displacement protocol that was used during the test is given in Figure 3.34. Moment-rotation relationship obtained during the test and observed deformations are given in Figure 3.35 and Figure 3.36, respectively. Permanent deformations and damages on the prototype are given in Figure 3.37.
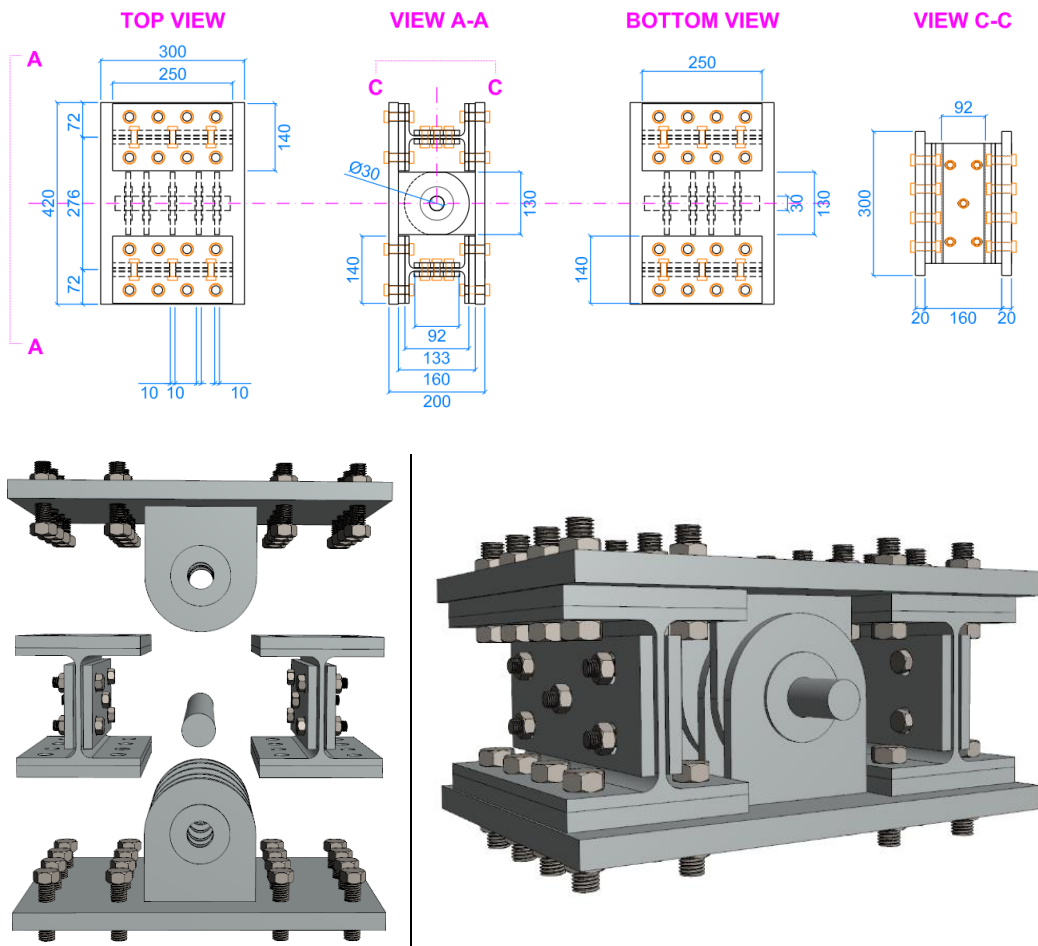
Figure 3.32: 2D and 3D drawings of PT4. Dimension in mm.
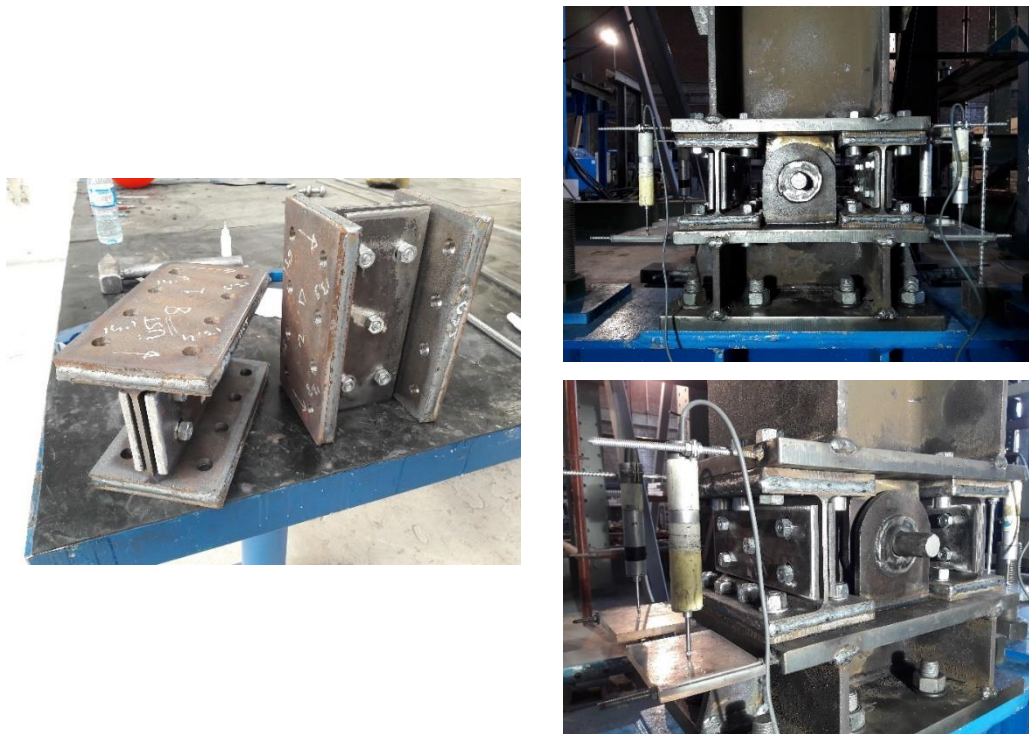
Figure 3.33: Production, view, and instrumentation of PT4 before the test
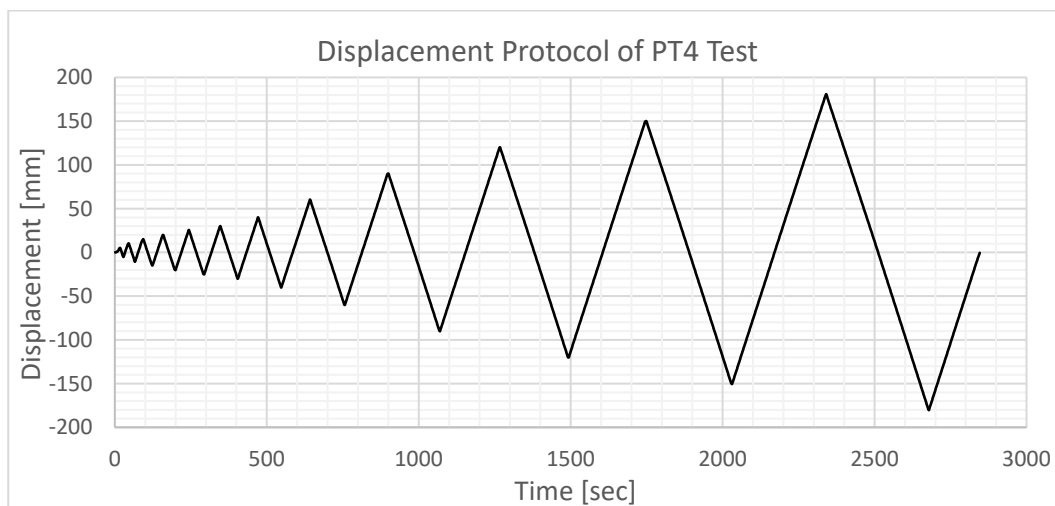
Figure 3.34: Displacement protocol of PT4 test
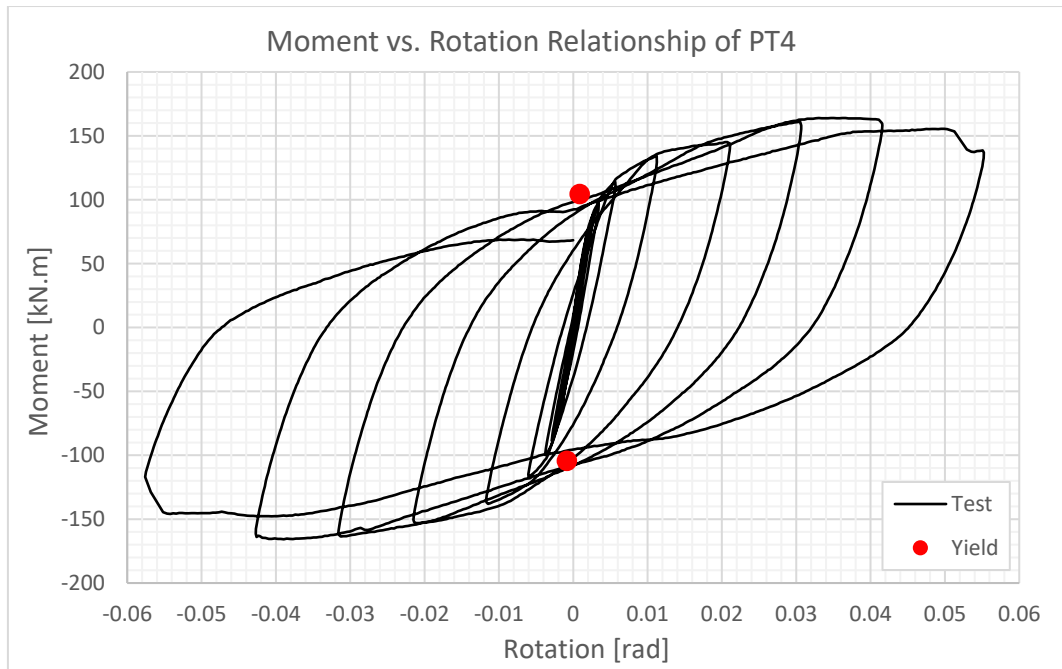
Figure 3.35: Moment-rotation relation obtained during the PT4 Test

Top Displacement: 60 mm	**P-Cell Rotation: 0.0112 rad**

Top Displacement: 90 mm	**P-Cell Rotation: 0.0211 rad**
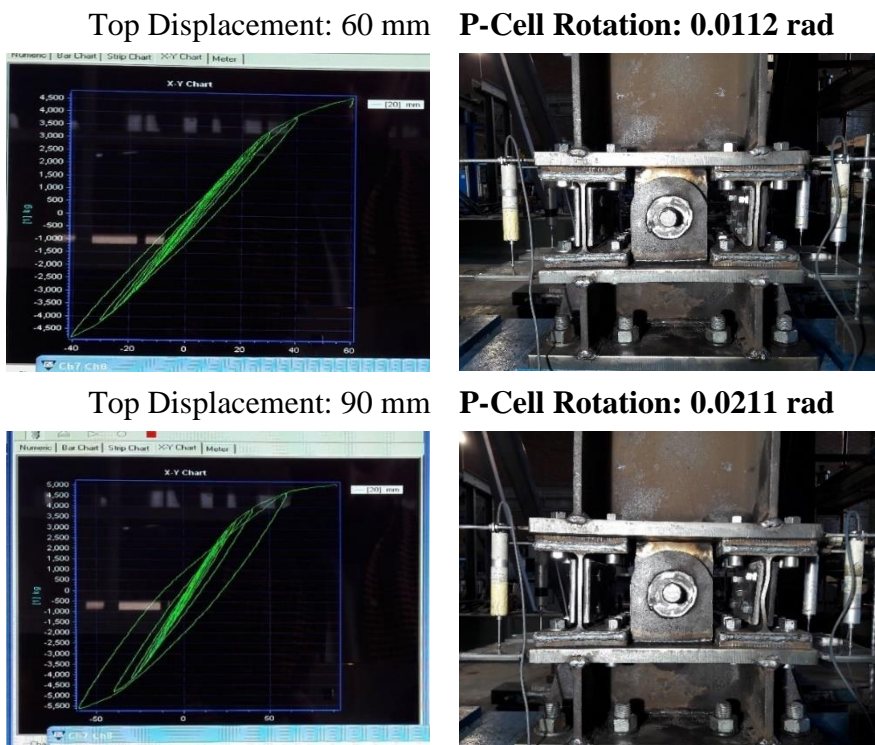
Figure 3.36: Observed deformations during PT4 Test at different top displacement and rotation levels

Top Displacement: 120 mm   **P-Cell Rotation: 0.0307 rad**

Top Displacement: 150 mm   **P-Cell Rotation: 0.0427 rad**
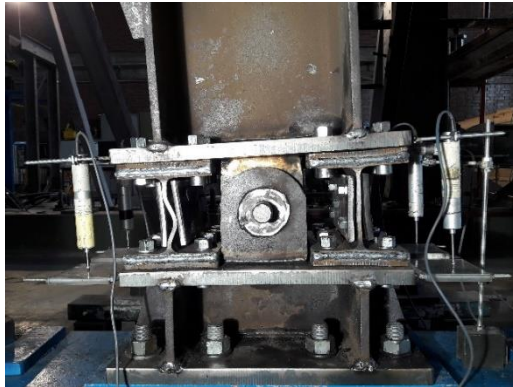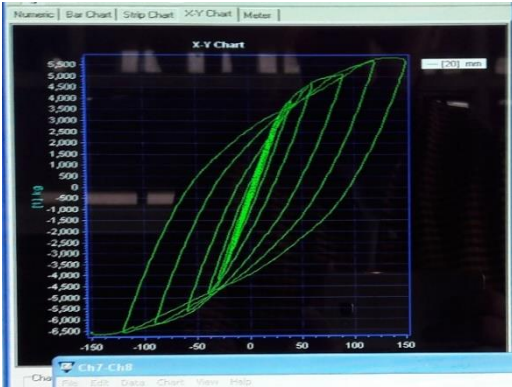
Top Displacement: 180 mm   **P-Cell Rotation: 0.0576 rad**
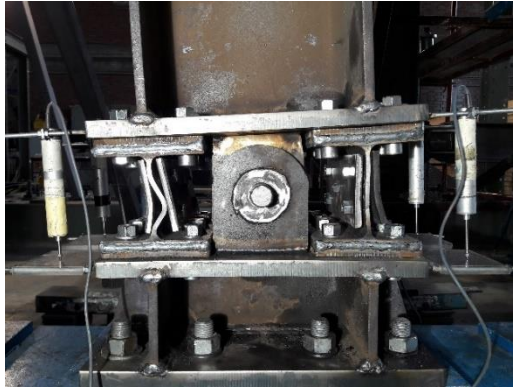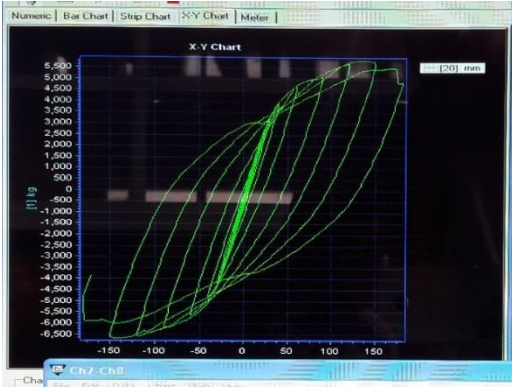
Figure 3.36 (cont'd)

Figure 3.37: Permanent deformations and damages after PT4 Test

Information on the results of the component test, observed damages and observations reveal that high rotational demands were achieved along with the expected damages and failure states of the improved P-Cell (rupture along the length of the web of H-section at almost the middle regions). Both hysteresis curve in Figure 3.35 and observations during the test, which are presented in Figure 3.36 clearly show that PT4 reached rotation capacities exceeding 0.055 radians. Moment-rotation curve given in Figure 3.35 also reveals a symmetrical behavior throughout reversed cyclic loading, which is an indication of an effective prevention of buckling under compressive forces.

The moment-rotation relation observed during the tests shown in Figure 3.35 indicates that although the yield moment is predicted accurately, yield rotation is under predicted. An apparent reason is the bending flexibility of backing plates that

are not considered in the rotational stiffness calculation of PT4. Flexural deformation of the backing plate, particularly the one on the tension (right) side, can be observed in Figure 3.36 and Figure 3.37. The same moment-rotation relation gives the information that the ultimate moment capacity was 166 kN.m, which indicates that the observed overstrength was around 1.6.

Consequently, PT4 was accepted as the ultimate design selection in which desired moment and rotation capacities were achieved at the end of prototype test process of the study. It was also decided that in the following frame test process in our study, PT4 would be utilized as the effective P-Cell.

Table 3.3: Summary of P-Cell Types, Components and Performed Tests

Component	Test	Revisions
PT1	1	-
PT2A	2	- T/C bars were re-designed as tapered to have outer diameter of 36 mm at both ends and 27 mm in the middle region. It was aimed that yielding and subsequent rupture would occur near/at the middle section.
PT2B	3	- T/C bar locations were completely revised so that the bars can be replaced after any event. T/C bars were welded to 20-mm thick adapter plates from outer surface (again), which were connected to backing plates by bolts. - Dimensions of drums were changed to adapt to adapter plate dimensions.

Table 3.3 (cont'd)

PT3	4	- It was considered that the main cause of torsional behavior observed during Test #3 on PT2B was that lateral stiffnesses of hollow section, tapered T/C bars was low that they cannot prevent such behavior. Therefore, two main options were considered to apply for the next prototype test: adding extra members (i.e., stiffener) to prevent torsion or changing current T/C bars in favor of members having much higher lateral stiffness. - The decision was to use I- or H-section steel members in the direction of T/C bars. In the first try, IPE140 steel profile member was selected as T/C members. - In order to increase flexural stiffness of the flanges against tensile forces additional plates were welded to the flanges of IPE140.
PT4	5	- It was observed that IPE140 profile was not suitable as a T/C member, with its insufficient web thickness that led to inelastic buckling, and it did not reach target rotation demands. - To prevent buckling failure, HEA140 steel profile with higher web thickness was selected as T/C member. Also, 10-mm-thick buckling restraint plates (BRP) were bolted to both faces of web of T/C member using slotted holes drilled on the web.

3.8   Analytical Modeling of P-Cell Design PT4

Section 3.7 consists of the design and test results of the ultimate version of the P-Cell, labeled as PT4. It is already discussed that PT4 has the desired moment and rotation capacities as well as a symmetrical behavior and effective prevention of buckling of T/C members under compressive forces.

This section includes the prediction and calibration of behavior of PT4 under reversed cyclic loading. The modeling process leads to having a dependable analytical model/representation of the P-Cell unit with adequate strength, energy dissipation capacity and loading-unloading paths. For that purpose, OpenSees

software platform was utilized, which was also used for the modeling of test frames that comprises the second phase of the study. In OpenSees, several readily available hysteretic material models have well-defined multi-linear force-deformation (in this case, moment-rotation) relationship. However, it is important to perform nonlinear dynamic analysis and obtain hysteretic curves under dynamic loading protocols to determine the behavior.

To this end, the analytical model of prototype test setup and PT4 was created in OpenSees platform. The exact geometrical and material properties of the setup, which is already presented in Figure 3.1 was reflected to the analytical model. Besides, loading protocol in terms of displacement-time history, which is given in Figure 3.34, was also applied in the analytical model of test setup at the top of lever arm of the analytical model.

The simple 2D model of the setup was created with two nonlinear frame elements having nonlinear steel force-deformation relation of structural steel with section HEA300, and a rotation spring having, again, nonlinear bi-linear force-deformation (moment-rotation) relation representing the behavior of PT4, placed between those two nonlinear steel members. Incremental cyclic displacement-time history, given in Figure 3.34 was imposed at the node defined at the level of piston in the analysis.

Hysteretic uniaxial material model Steel02, which is Giuffré-Menegotto-Pinto Model with Isotropic Strain Hardening, was used to represent the nonlinear behavior of P-Cell. The representation of the material model is presented in Figure 3.38, with the modeling parameters that are defined to constitute the model. There are three main parameters of the material model: Yield strength, initial elastic tangent, and strain hardening ratio. The parameters are presented in Table 3.4 and corresponding values determined for PT4 are given in the same table.
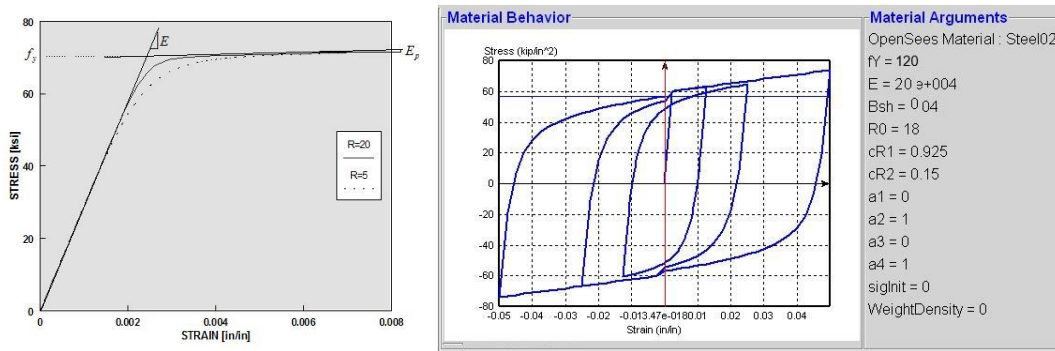
Figure 3.38: Representation of hysteretic uniaxial material model Steel02 in OpenSees

Table 3.4: Modeling parameters of PT4 used in analytical model

Parameter	Abbr.	Value
Yield strength/moment	M_y	120 kN.m
Yield rotation	θ_y	0.004 rad
Initial elastic tangent	E	30,000 (*)
Strain-hardening ratio	B	0.05

(*) It is determined and expressed as the ratio of yield moment, M_y, to yield rotation, θ_y, observed during the prototype tests.

Besides those main parameters presented in Table 3.4, there are several complementary parameters to control the transition from elastic to plastic branches, and isotropic hardening. Controlling the complementary parameters in order to calibrate and better predict the hysteretic behavior of PT4 obtained during prototype testing led to a suitable and accurate modeling of PT4. The moment-rotation relationship obtained during the test and performed analysis are presented comparatively in Figure 3.39.
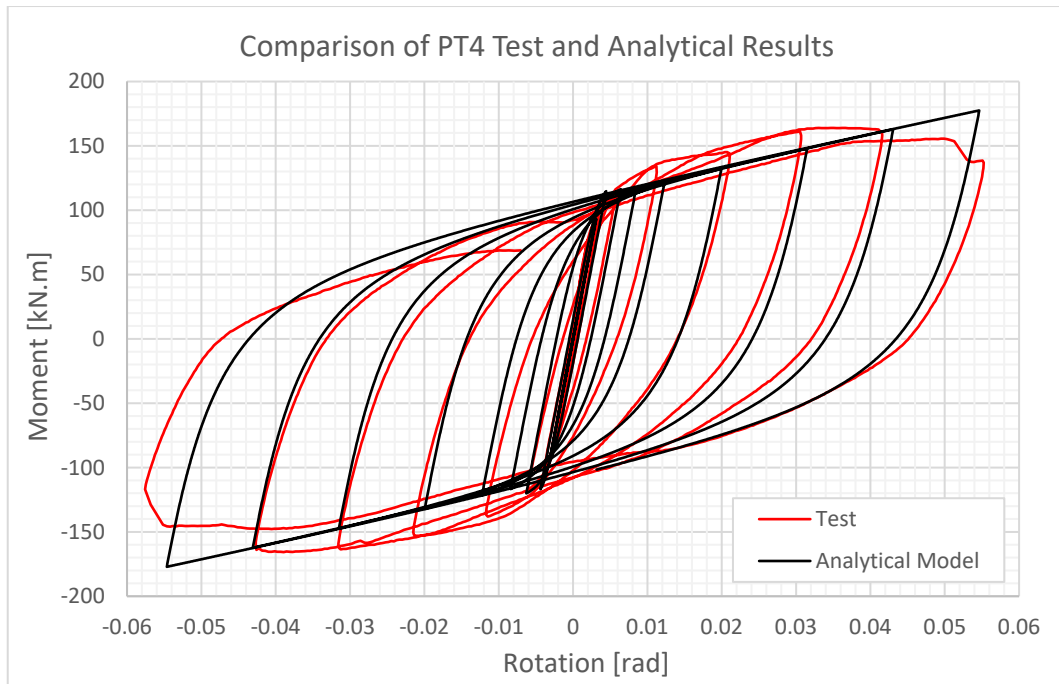
Figure 3.39: Comparison of test and analytical model results of PT4

Figure 3.39 demonstrates that the analytical model of PT4 defined with the hysteretic model in Figure 3.38 and with parameters given in Table 3.4 are in very good agreement with the hysteretic moment-rotation relation obtained from PT4 test, presented also in Figure 3.35. After this modeling process, it was determined that analytical model representation is accurate to be used in the analytical modeling and nonlinear analyses of frame tests.

CHAPTER 4

FRAME TESTS WITH P-CELLS

Chapter 3 has introduced the design and testing methodology of P-Cells and elaborated on the development of P-Cells with different designs, configurations, and performance under reversed cyclic loading. At the end of laboratory tests on P-Cell units, the final configuration and design of P-Cell was obtained, which is labeled as PT4. The unit was comprised of backing plates, drums, central pins, and most importantly T/C components with buckling restrained plates, which governs the performance of the P-Cell unit.

This chapter comprises of the introduction of test frames and the results obtained for four different frame tests. A brief information about the tests is presented in Table 4.1, where the frame tests differ in terms of the condition of fixity at the base, number of bays of the frame, number of P-Cells installed at the frame and the loading type.

Table 4.1: Frame test matrix

Test	Bays	Frame Configuration	P-Cell Configuration	Loading Type
1	2	Pin-base	4 at the 1st St. Beam ends	Reversed cyclic
2	2	Fixed-base	4 at the 1st St. Beam ends	Reversed cyclic
3	2	Fixed-base	2 at the 1st St. Beam ends	Reversed cyclic
4	1	Fixed-base	2 at the 1st St. Beam ends	Pseudo-dynamic
5	1	Fixed-base	2 at the 1st St. Beam ends	Reversed cyclic

4.1 The Test Frame

This section introduces the test frame, which was constructed to test and evaluate the behavior and performance of P-Cells. It is a frame structure equipped with P-Cells, tested either under incrementally reversed cyclic loading or through pseudo-dynamic loading under a ground motion record. 2D elevation view and 3D drawing of the test frame is presented in Figure 4.1. Several detail views of the frame, particularly regarding the P-Cells and column bases are shown in Figure 4.2. The rationale for developing the test frame, its manufacturing and installment, and instrumentation of the frame are presented afterwards. It should also be noted that the design and detailing of the test frames are significantly changed throughout the study program, which is given in Table 4.1, in terms of end conditions, number of bays and P-Cell configuration. The test frame is presented in this section only schematically, while the design of each frame is specifically given in their sections.
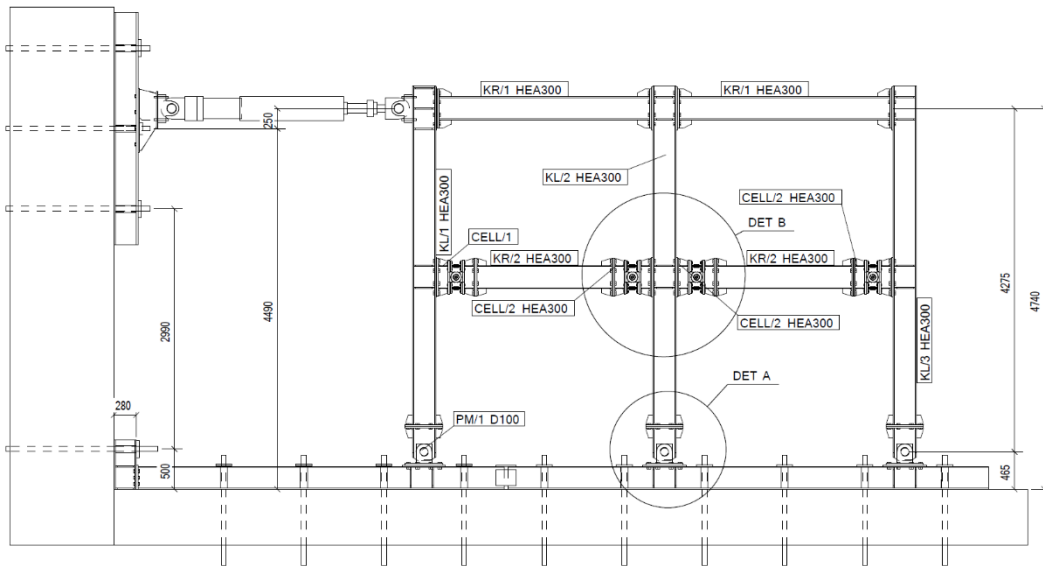

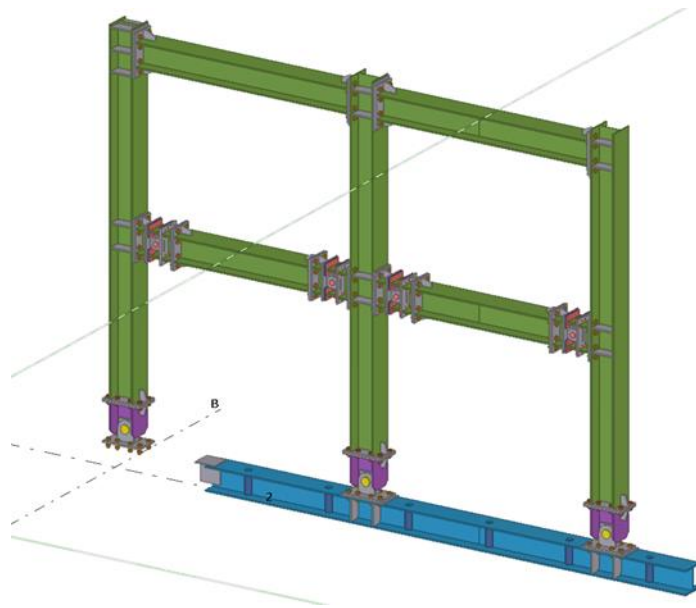Figure 4.1: 2D elevation view and 3D drawing of the test frame. Dimensions in mm.
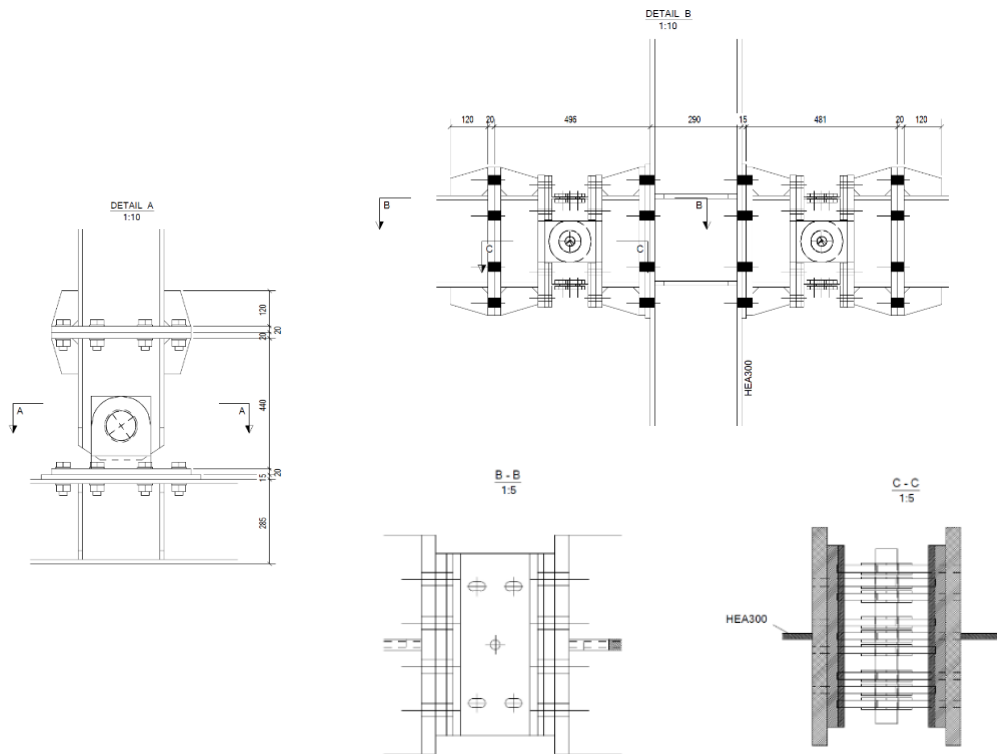
Figure 4.1 (cont'd)

Figure 4.2: Detail views of the test frame. Dimensions in mm.

It was specified during the design of test frame that P-Cells at the ends of 1st story beams would exhibit yielding behavior before any other member of the frame. For this purpose, 1st story beam sections having higher plastic flexural capacity than the P-Cell ultimate moment capacity were selected in order to ensure that they remain elastic during the test.

At this point, with the reasoning that the frame test is considered as a proof of concept, several constraints and assumptions were considered in terms of time and costs, during the design and production of P-Cells and frame members. They are listed below.

- The test setup for P-Cell units was designed and produced in a way that does not exhibit any post-yield behavior at the target rotation demands of at least 0.05 rad. As a result of this design criteria, P-Cell unit test setup was designed to be produced from HEA 300 section steel profiles having a plastic moment capacity of 380 kN.m, which is about twice the ultimate capacity of the P-Cells. Also, in order to ensure perfectly concentric tension-compression force application on the T/C components of P-Cells during reversed cyclic motion during unit tests, flanges of HEA 300 section members of test setup and T/C components of P-Cells were arranged to be concentric. This situation required P-Cells and connecting frame/setup members to be compatible with each other.

- It would require performing 1:1 scale unit test on the P-Cells before frame test that would later be installed to the test frame; in order to obtain P-Cell moment-rotation relation that would be used in predicting frame test results before test and perform advanced analyses on the frames. Reliable and successful P-Cell results obtained from the latest P-Cell unit, PT4, led us not to change the P-Cell design and not to repeat the entire P-Cell manufacturing, test setup revision, etc. and continue with the existing P-Cell design.

- P-Cell frame member sections and dimensions were determined considering the existing P-Cell dimensions and type test setup. Then a simple analytical

model of the 2-story test frame was constructed and yielding behavior of P-Cells and frame members was analyzed. Finally, the design presented in Figure 4.1 and Figure 4.2 was decided.

Manufacturing of the Test Frame

After the analysis, design and selection of test frame members were completed, steel frame was detailed for manufacturing. Manufacturing and installation of the frame was also simulated in the software and the shop drawings were created after the simulation and detailing. Afterwards, frame members were manufactured, and installed in the Structural Mechanics Laboratory of METU Civil Engineering Department. Photos from production processes are presented in Figure 4.3 and photos after their installation at the laboratory are presented in Figure 4.4.

Figure 4.3: Production of P-Cells and frame members

Figure 4.4: Test frame FT1 after the installation at the laboratory

Instrumentation of the Test Frame

The test frame, which is introduced in this section is instrumented as defined and presented in Figure 4.5 and Table 4.2. As can be investigated here, there are several types of instruments, which are used for different purposes. Load cell (1) and 500-mm-LVDTs (2) are utilized to record and validate the global response of the test frame, such as applied story forces and displacements. Besides, four sets of 50-mm-LVDTs (3) that are used for each P-Cell are used to calculate the rotations on them, using geometry. Sixteen strain gauges (4) are used at several member ends of the frame, in order to observe the level of deformation throughout the tests. The locations of the strain gauges are determined as a result of a preliminary pushover analysis, which reveals the hinging hierarchy as well as the capacity of the frame system. Three tiltmeters (5) are also used on each column to record the column base rotations. Lastly, the stability of the base beam is observed through two LVDTs (6).
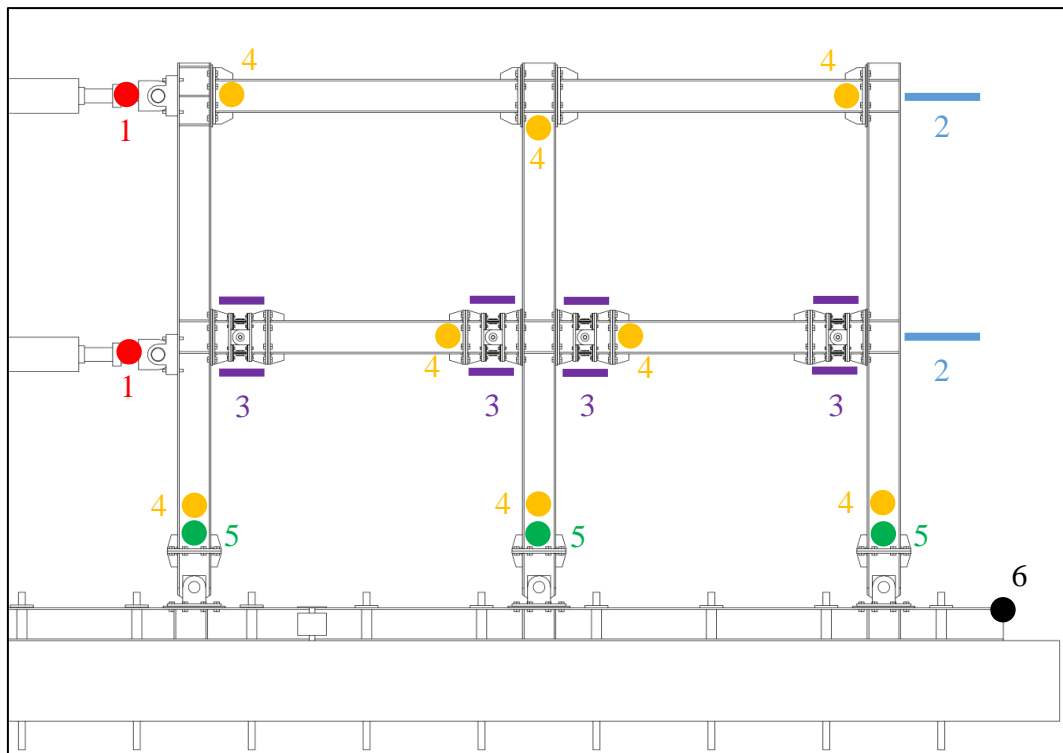

Figure 4.5: Locations of instruments on the test frame

Table 4.2: List of instruments which are used on the test frame

| No	Type	Location	Quantity	Function
1	Load cell	Pistons	2	Recording the story forces resulting from applied displacement
2	500 mm LVDT	Story levels	2	Recording and validating applied and calculated displacement
3	50 mm LVDT	Corners of all P-Cells	16	Calculating P-Cell rotation through geometry
4	Strain gauges	Member ends	16	Recording and observing strains at selected member ends
5	Tiltmeter	Column bases	3	Recording column base rotations
6	20 mm LVDT	End of base girder	2	Recording possible sliding and uplift on the base girder

(a)

(b)

(c)

(d)
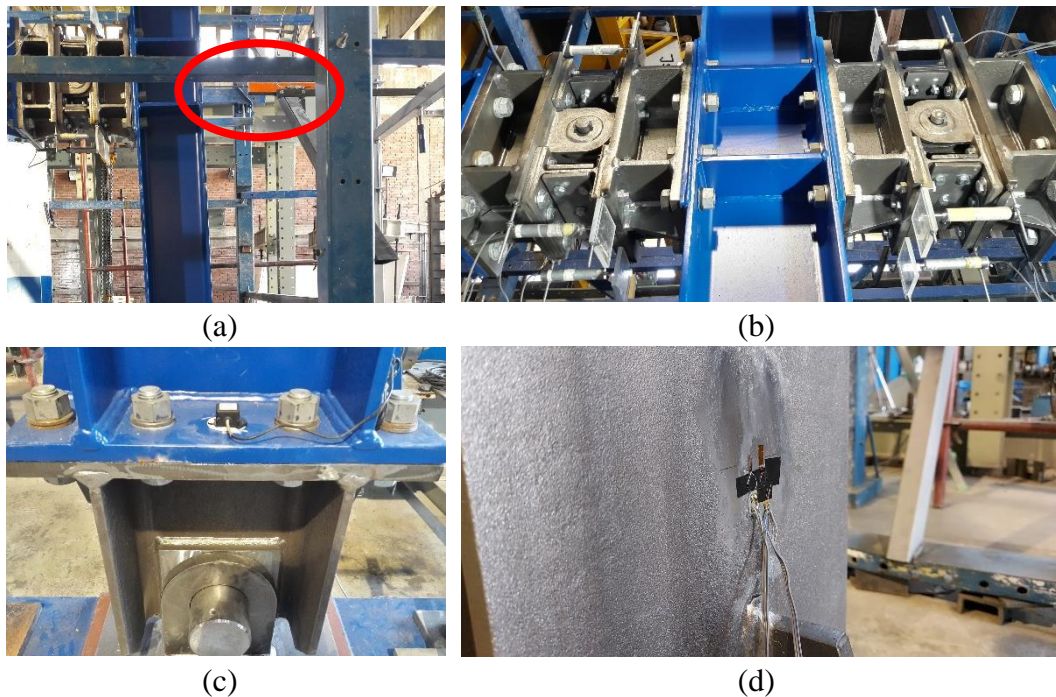
Figure 4.6: Instrumentation of test frame: (a) 500-mm LVDTs (in red circle), (b) 50-mm LVDTs on P-Cells, (c) Tiltmeter at column base, (d) Strain gauge at column base

4.2 FT1: Two-Bay, Pin-Based Frame with Four P-Cells

FT1 is the first frame test that was tested in the scope of this study. The general framework was already presented in Table 4.1 and Section 4.1, and as inferred from the information, FT1 was the only frame that was constructed with pin ended columns at the base. The other common features are summarized as being a 2-story, 2-bay steel frame, at which P-Cells were installed at both ends of 1st story beams. The test was performed under incremental reversed cyclic loading protocol, which is presented in Figure 4.7. The displacement values in the protocol were imposed at the second story and the story loads calculated by the actuators were applied to the frame in an inversed triangular shape, i.e. the ratio of first to second story load was 1:2. Story displacements, P-Cell rotations, column base hinge rotations and strains at the 2nd story beam ends and column top ends, which were expected to essentially remain elastic, were continuously recorded during the test under that loading. Additionally, base shear force was recorded as total lateral force recorded from the piston load cells, considering static equilibrium.
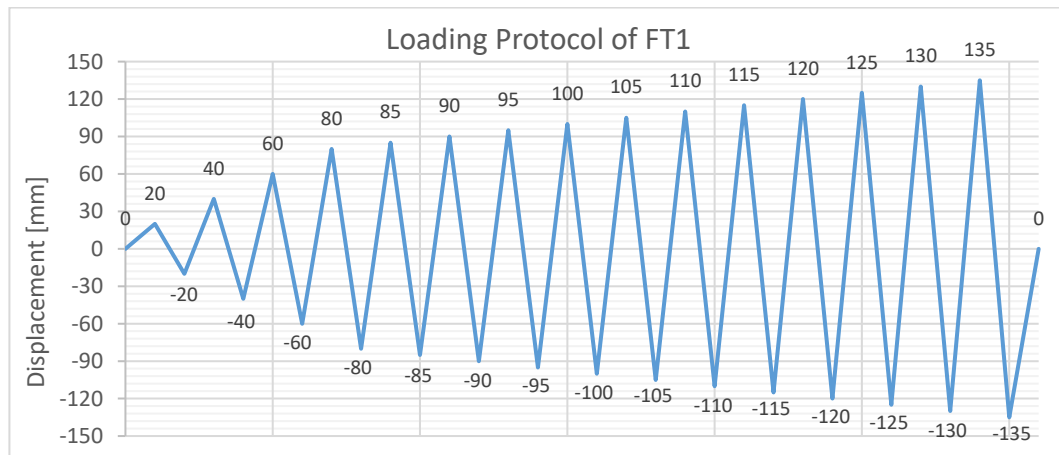

Figure 4.7: Displacement-imposed loading protocol of FT1 test where the target displacements are applied at the 2nd story

The relationship between the recorded parameters is presented in this section from Figure 4.8 to Figure 4.11 with the graphs listed below.

1. Story displacements vs. base shear force
2. P-Cell rotations vs. base shear force
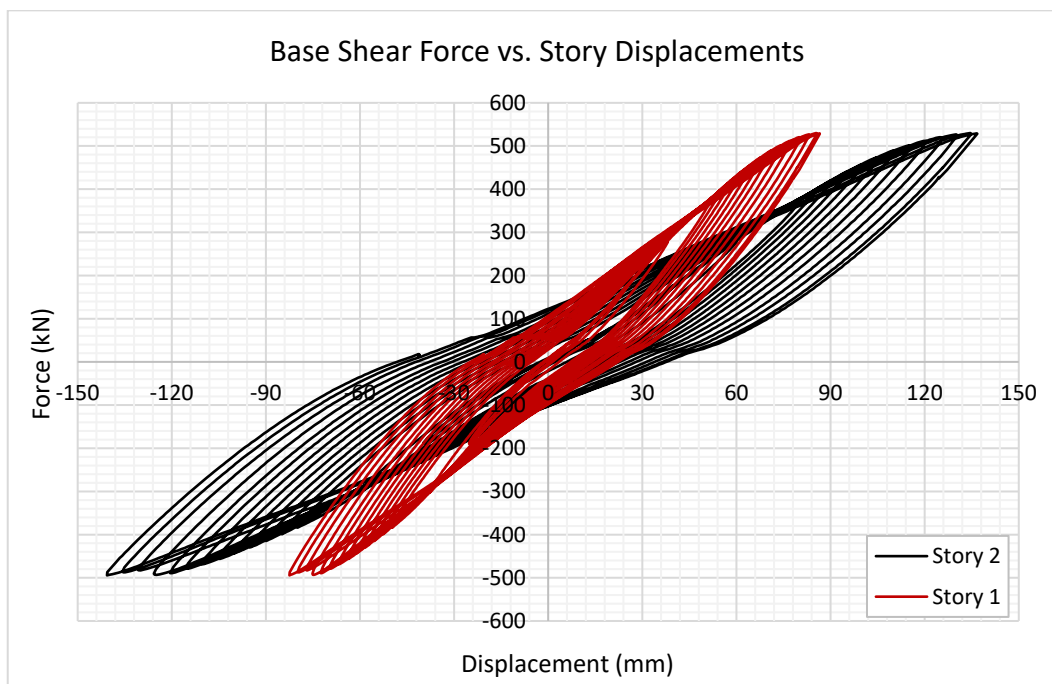3. Column base rotations vs. base shear force

Figure 4.8: Base shear force – Story displacement relationship obtained during the FT1 test
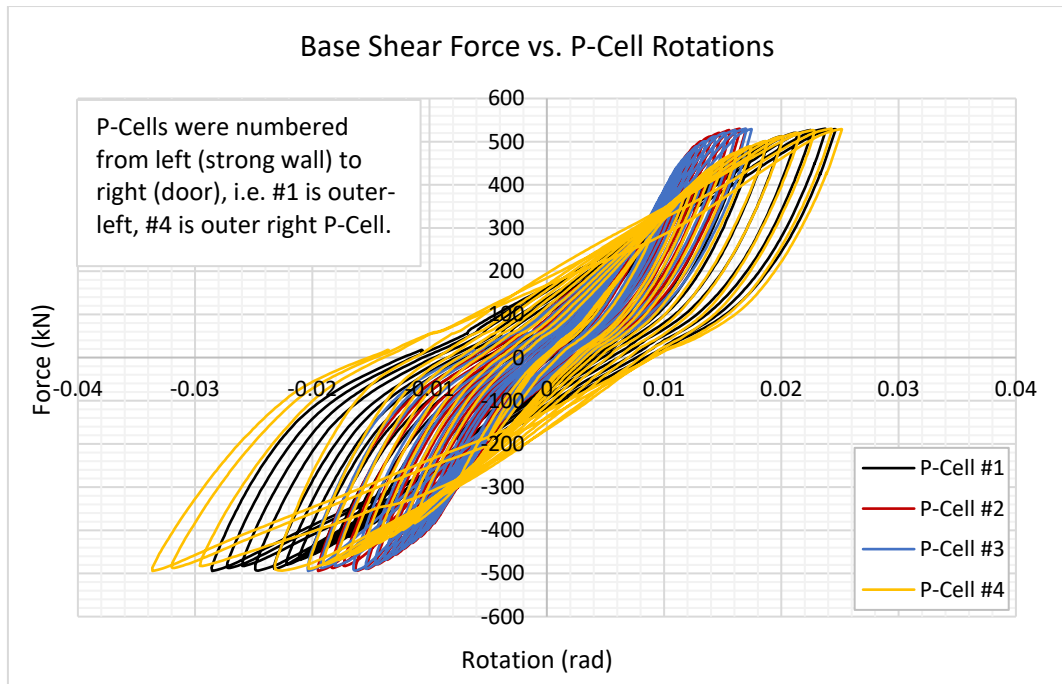
Figure 4.9: Base shear force – P-Cell rotation relationship obtained during FT1 test
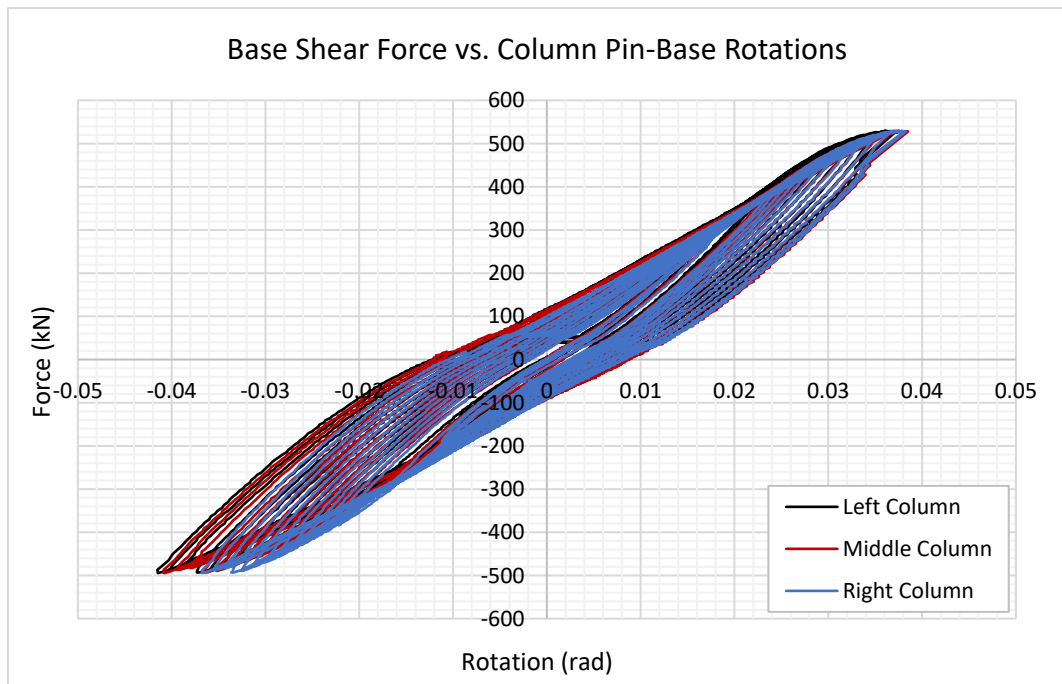

Figure 4.10: Base shear force – Column pin base rotation relationship obtained during FT1 test

Base shear force vs. Story displacement relationship presented in Figure 4.8 demonstrates that nonlinear frame behavior started after a top displacement of approximately 60 mm, corresponding to a drift ratio of 1.35%. Base shear force vs. P-Cell rotations presented in Figure 4.9 indicates that outer P-Cells, identified as P-Cell #1 and #4, exhibited higher rotations as compared to the inner P-Cells, which is an expected behavior in this frame. The deformations presented in Figure 4.12 were also in accordance with the numerical results recorded during the test, i.e., higher deformation levels were always observed in outer P-Cells. More notably, P-Cell #4 having a slightly higher rotation value than P-Cell #1, exhibited a rupture at the maximum displacement step of reversed cyclic loading, corresponding to approximately 0.034 rad of rotation. Considering the results and observations of the P-Cell unit test PT4, the situation was rather unexpected. The behavior may be attributed to fatigue, which may result from the high number of cycles applied during the test.

The relationship also indicates that maximum rotations observed at the end of the test was around 0.03 rad. Considering that the target rotation capacity of a P-Cell is at least 0.04 rad, it can be concluded that the outer P-Cells reached 75% of their rotational capacities. Figure 4.10 also shows that column base rotations reached 0.04 rad.

Strain data recorded at the 2nd story beam-ends and column ends are also presented in Figure 4.11. The steel material class that the frame members are produced is S275, hence the yield strength is approximately 280 MPa. This indicates that frame members have a yield strain of approximately 0.0014. In the light of this material information, it can be commented that 2nd story column top-end almost reached yielding at the end of the test. This situation also shows that the test was concluded within desired capacity limits.
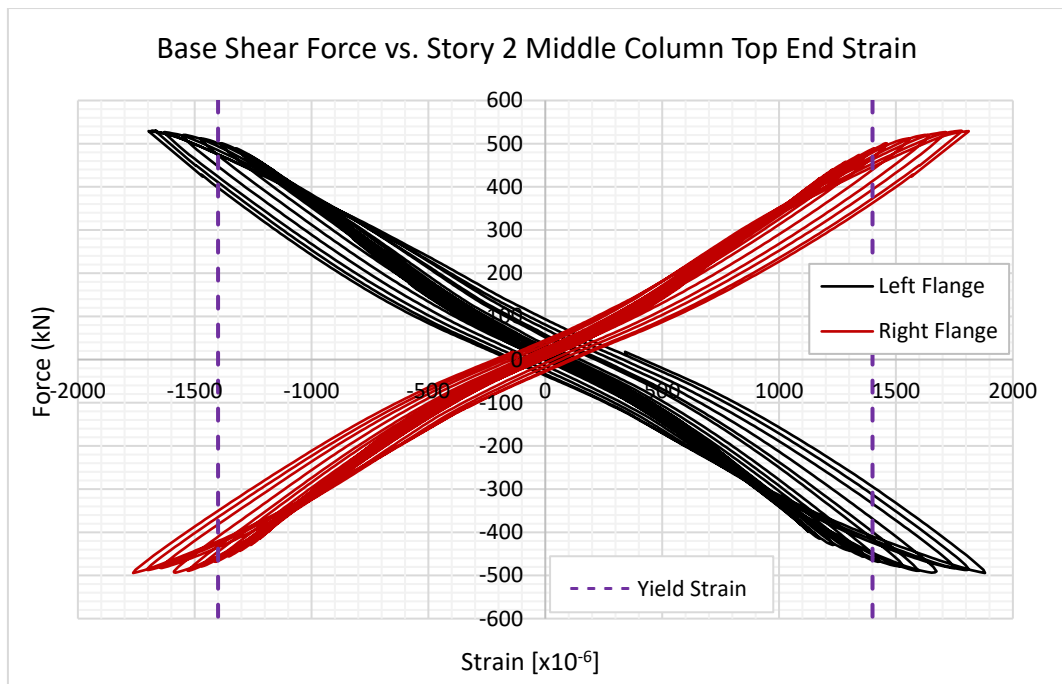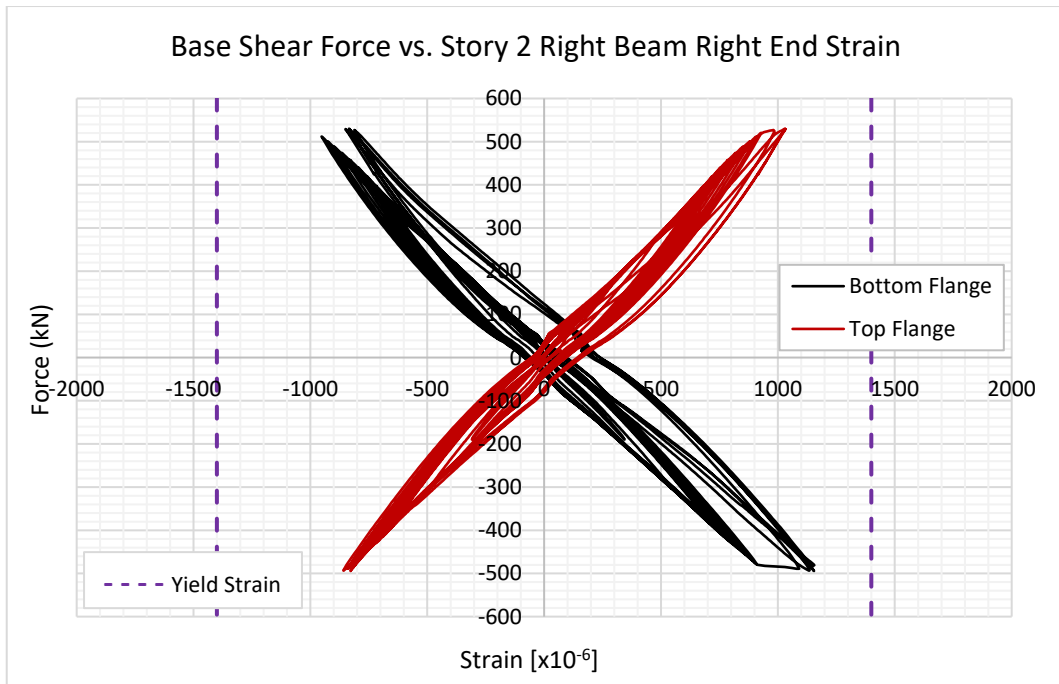
(a)
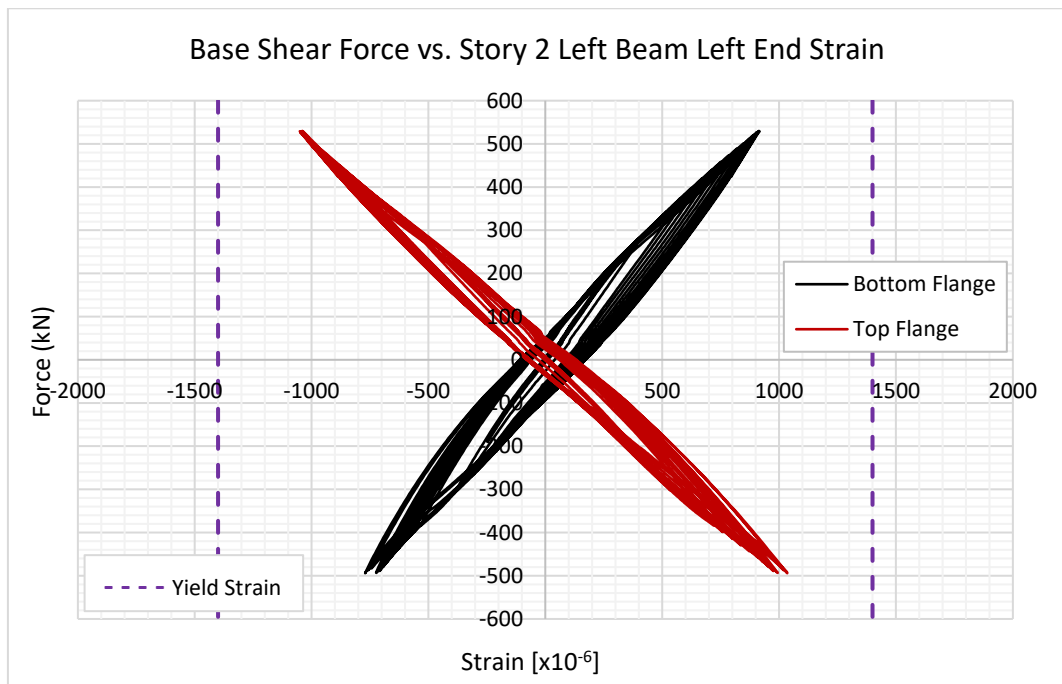
(b)

Figure 4.11: (a) Base shear force – 2nd story mid column top end strain, (b, c) Base shear force – 2nd story beam ends strain relationships obtained during FT1 test
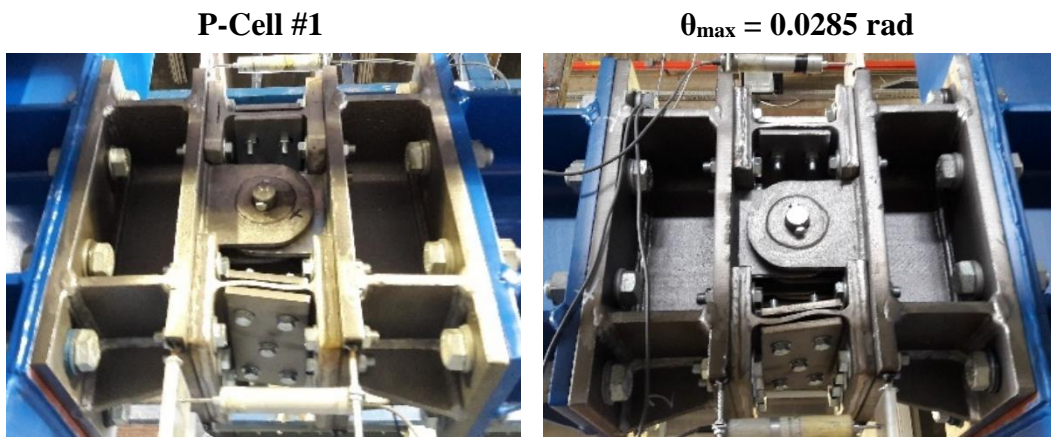
(c)

Figure 4.11 (cont'd)

P-Cell #1   **θ$_{max}$ = 0.0285 rad**

Figure 4.12: Observed deformations and maximum rotations at P-Cells at the end of FT1 test

P-Cell #2 and #3 $\theta_{max} = 0.0204$ rad

P-Cell #4 $\theta_{max} = 0.0336$ rad
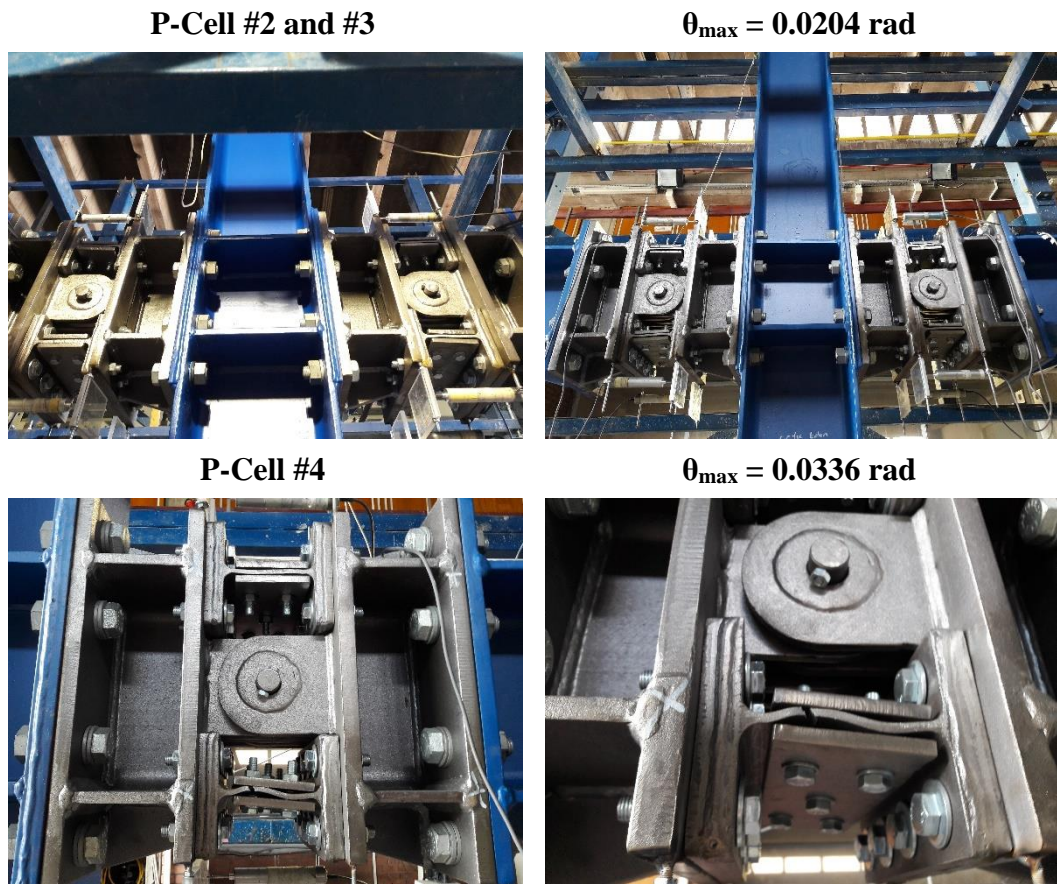
Figure 4.12 (cont'd)

4.3 FT2: Two-Bay, Fixed-Base Frame with Four P-Cells

During FT1 test, it was experienced that the pistons of the actuator system that were used to impose displacement and loads had an actual capacity of 360 kN, even if the nominal value was higher. While an inverted triangular load pattern was applied during the test, the total base shear load capacity reached was around 540 kN. Therefore, it was evaluated that a uniform load pattern with the ratio of first to second story load as 1:1 shall be used to achieve higher total force capacities on the frame and higher rotations on the P-Cells. Besides, as given in Table 4.1, FT2 frame was

constructed as fixed base; it means that the total force demand would be higher as compared with FT1 frame. The elevation view of the FT2 is presented in Figure 4.13.

FT2 test was performed under incremental reversed cyclic loading protocol presented in Figure 4.14 with uniform load profile during the entire test. Story displacements, P-Cell rotations, column base rotations, strains at the column bases and strains at the 2nd story beam ends and mid column top were continuously recorded during the test under this loading. Additionally, base shear force was recorded as the sum of lateral forces recorded from piston load cells, considering static equilibrium.
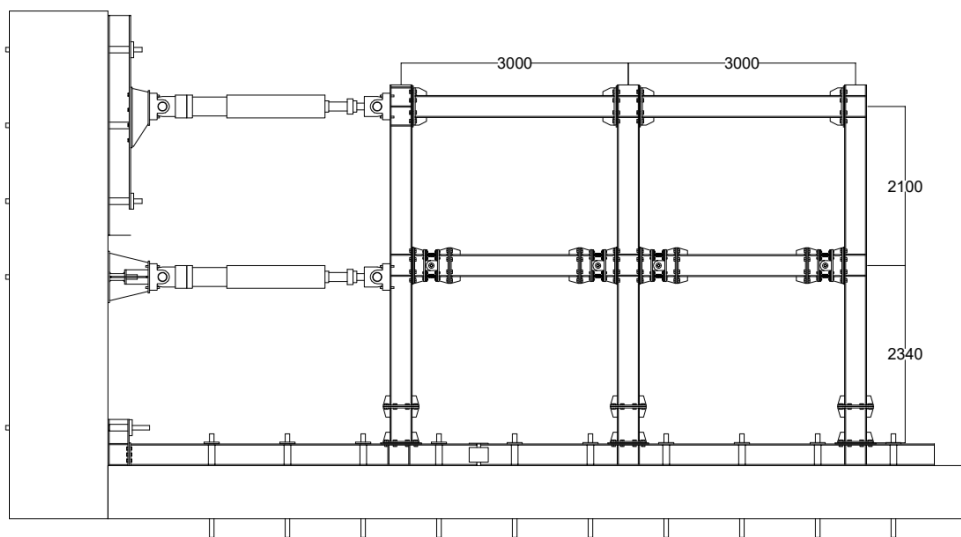
Figure 4.13: Elevation view of FT2 frame. Dimensions in mm.

Relation between those recorded parameters is presented in this section from Figure 4.15 to Figure 4.18 with the graphs listed below.

1. Story displacements vs. base shear force
2. P-Cell rotations vs. base shear force
3. Column base rotations vs. base shear force
4. Column base strains vs. base shear force

Figure 4.14: Displacement-imposed loading protocol of FT2 test applied at the 2nd story

Figure 4.15: Base shear force – Story displacement relationships obtained during FT2 test

Figure 4.16: Base shear force – P-Cell rotation relationships obtained during FT2 test

Figure 4.17: Base shear force – Column base rotation relationships obtained during FT2 test
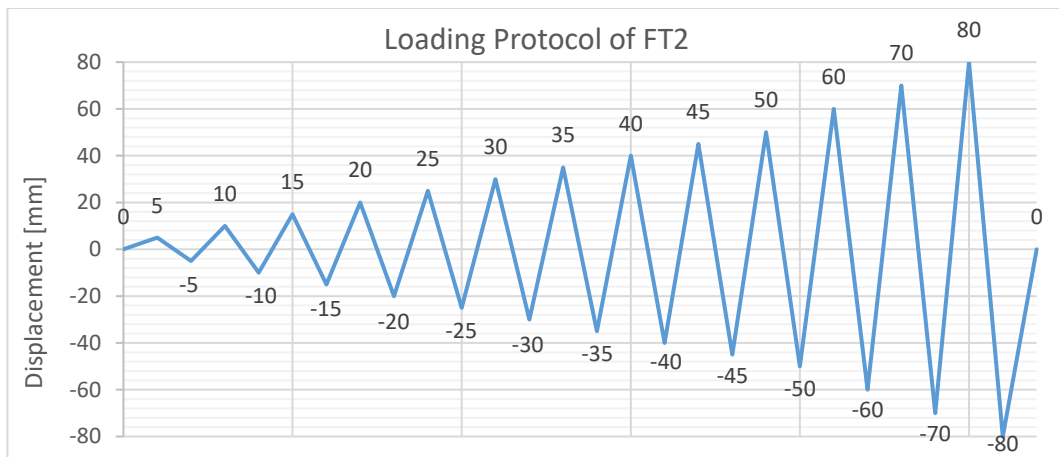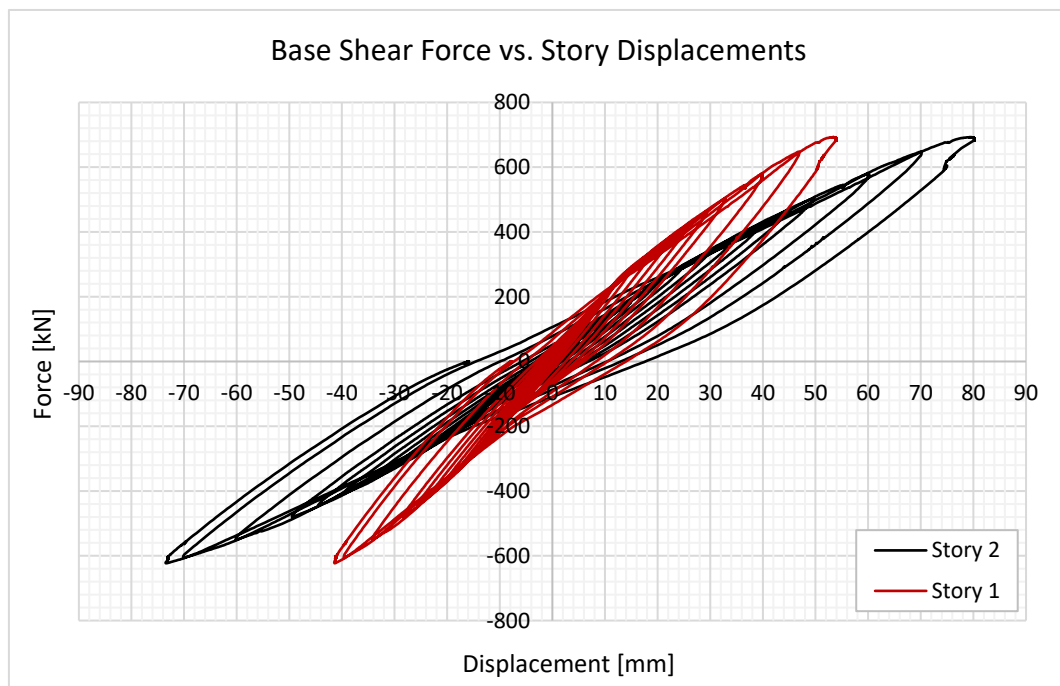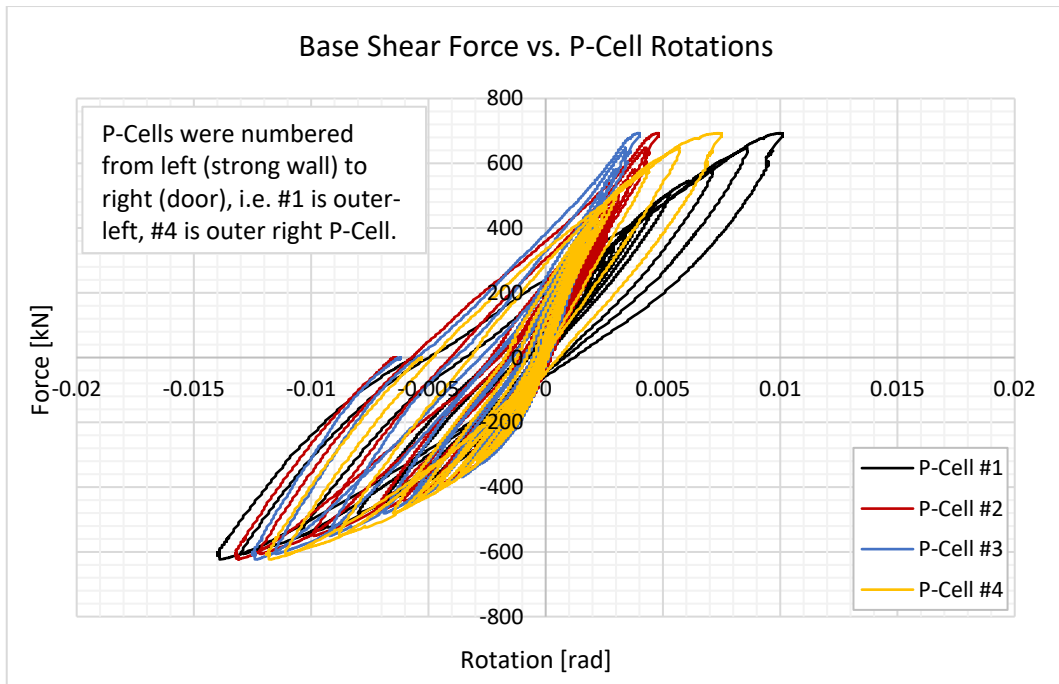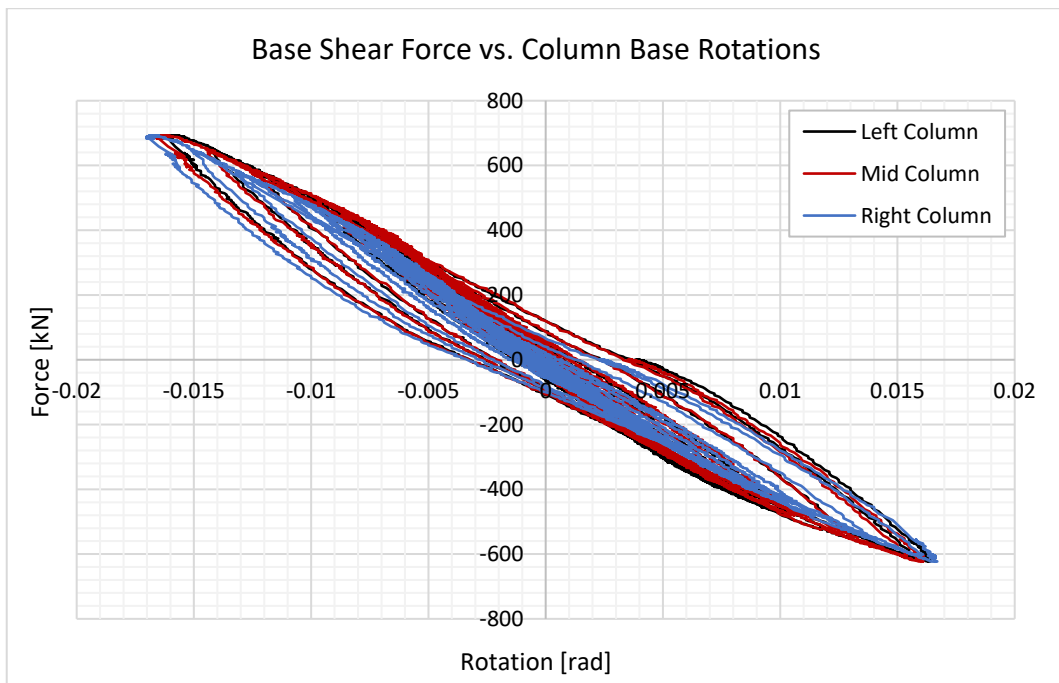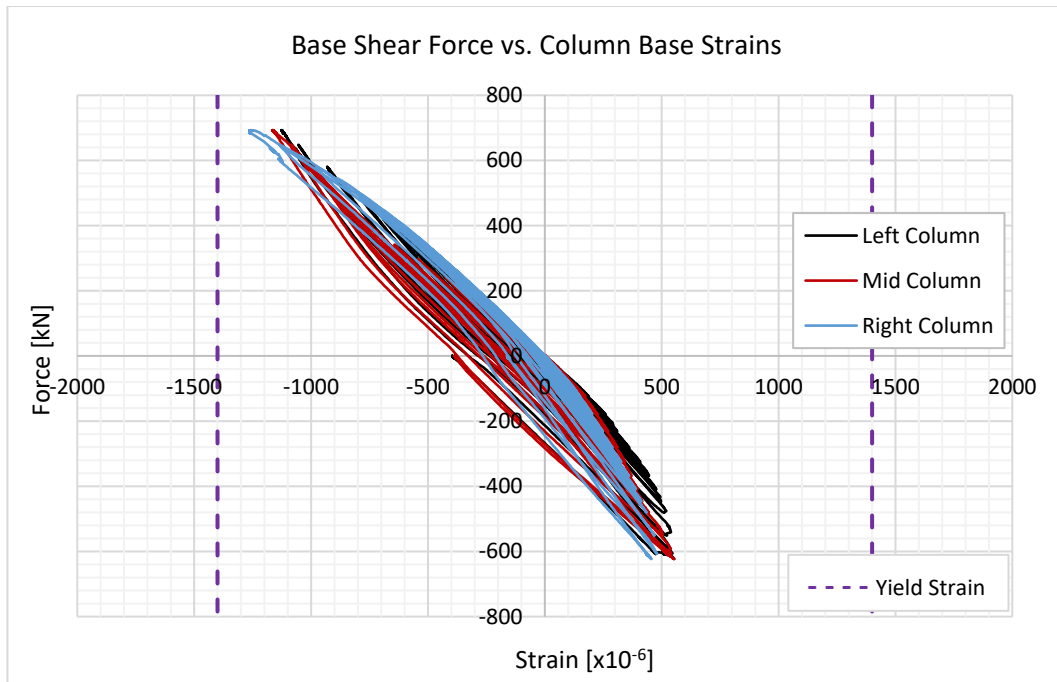
Figure 4.18: Base shear force – Column base strain relationships obtained during FT2 test

The most important observation from FT2 test was that the frame did not exhibit significant yielding and post-elastic behavior. P-Cells have yielded, and some initial deformations were observed in P-Cell #4 but observed rotation values did not point to significant plastic rotation values, as compared with previous pin-base frame test and especially prototype tests. In parallel to the recorded P-Cell rotation values throughout the test, no significant deformations at the P-Cell T/C components occurred.

Strain data recorded at the 2nd story beam ends and column end are also presented in Figure 4.19. The steel material class that the frame members are produced is S275, such that yield strength is approximately 280 MPa. This indicates that frame members have a yield strain of approximately 0.0014. In the light of this material information, it can be commented that 2nd story column top end almost reached yield point at the end of the test. However, column bases did not yield and remained in the elastic range.
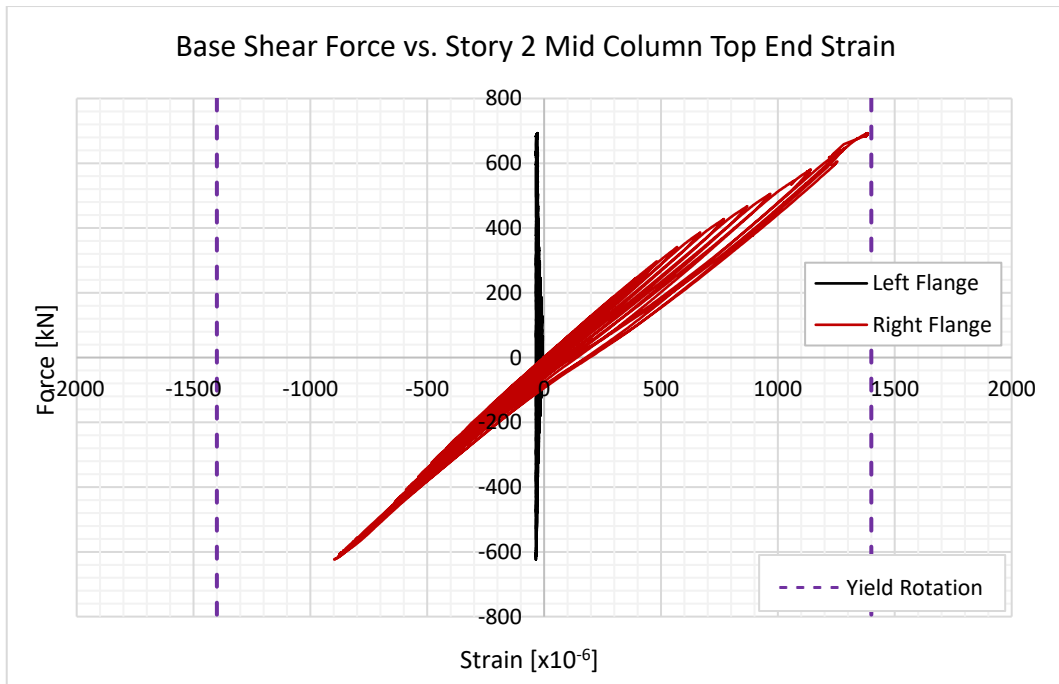
(a)
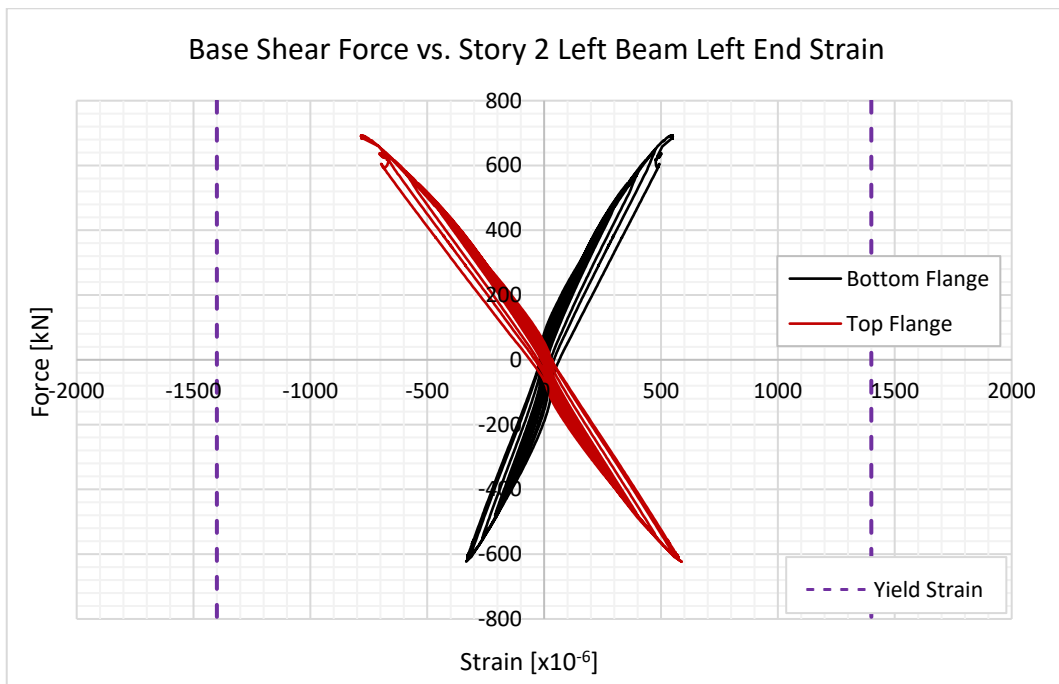
(b)

Figure 4.19: (a) Base shear force – 2nd story mid column top end, (b, c) Base shear force – 2nd story beam ends strain relationships obtained during FT2 test

138

Base Shear Force vs. Story 2 Right Beam Right End Strain
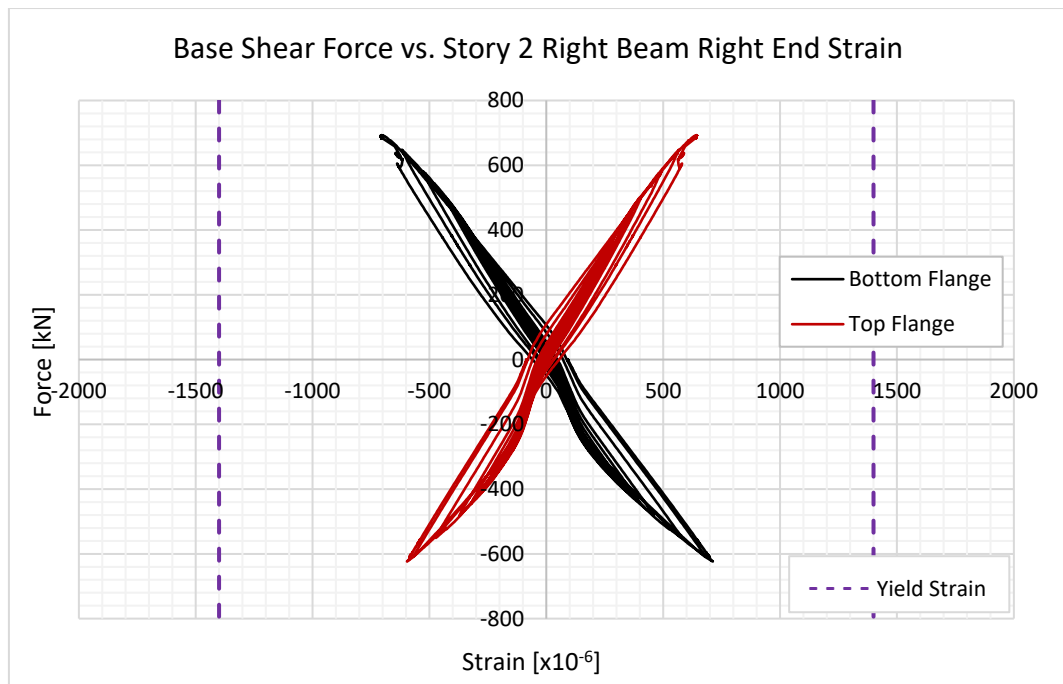
(c)

Figure 4.19 (cont'd)

4.4   Analyses on the Analytical Models of FT1 and FT2

This section presents the analytical results of FT1, for which the experimental results were already presented, and FT2. The same calibrated analytical model, with the available P-Cell analytical model, has been used for the preliminary capacity analysis of the fixed-base frame. The analysis was performed to predict and determine the yielding sequence of the frame and its total force capacity.

The force capacity of the testing system of the laboratory was of high importance since the force capacity of pistons was limited at the laboratory, which was theoretically 400 kN, but practically 350 kN in pushing and 320 kN in pulling directions. It was considered that total applied force capacity would be sufficient to make P-Cells yield and push the frame toward story displacement levels that P-Cells go well beyond their yield rotation limits. It was also considered that the frame

members would not go beyond their elastic deformation limits, stay in the elastic range, and would help the frame to re-center itself after the removal of yielded P-Cells.

In the light of those considerations, different force profiles were used in the analysis and expected behavior of the frame has been determined in terms of force capacity-top displacement relation and yielding sequence of the P-Cells and frame members. Summary of analysis results are presented in Figure 4.20, with the comparison of the capacity of previous pin-base frame, FT1.
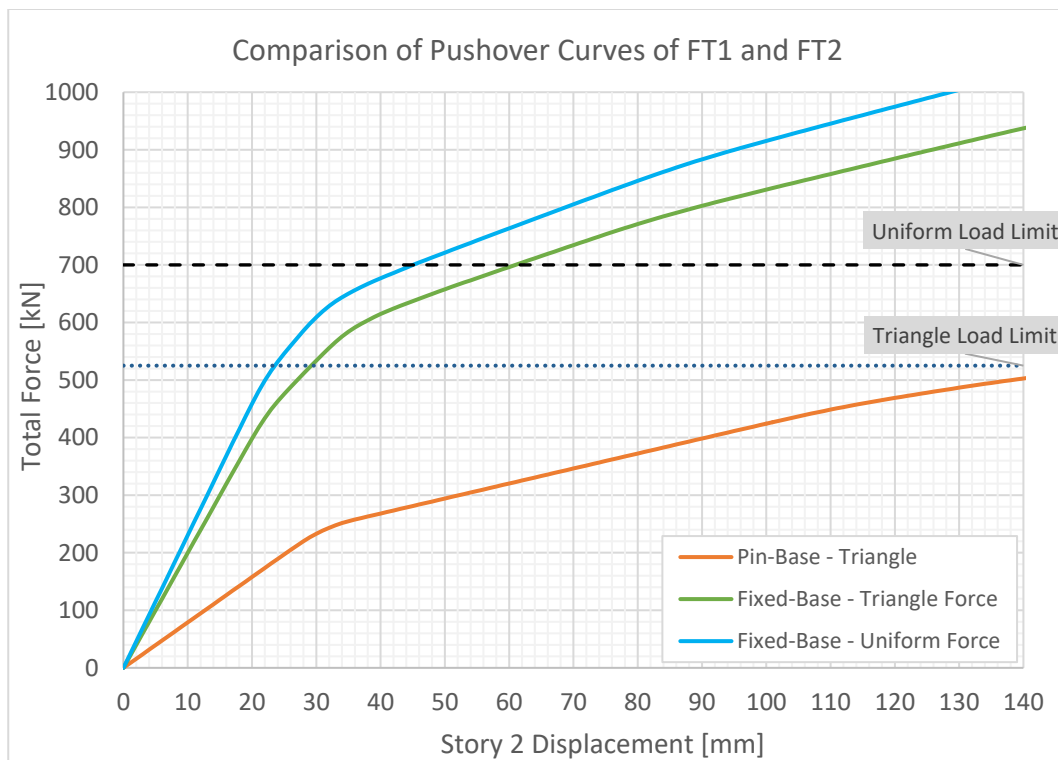

Figure 4.20: Pushover analysis result of the analytical models of FT1 and FT2, and comparison with backbone of FT1 test result

The most prominent observation obtained from Figure 4.20 is that when inverted triangle force profile is applied, total force capacity would be around 525 kN (Story 2: 350 kN + Story 1: 175 kN) and green curve will pair with "Triangle Load Limit" on the curve, and force capacity will be reached just after P-Cells yield. However, if the uniform force profile is applied, total force capacity will be around 700 kN (2*350 kN) and considerably higher top displacements would be applied after the yielding of P-Cells. Consequently, it was decided that uniform load profile will be applied during the frame test, with the expectation of reaching a top displacement of 50 mm at the total force capacity.

4.5   FT3: Two-Bay, Fixed-Base Frame with Two P-Cells

FT2 test was performed on the frame having four P-Cells placed at all ends of the beams at the 1st story of the frame, as presented in the previous Section 4.3. The most important observation made on the behavior of the frame and results of FT2 was that P-Cells did not exhibit significant post-yield behavior, as compared to FT1 test and especially the type tests on P-Cells, which were the subject of Chapter 3. The main reason for not reaching the rotation and energy dissipation capacity of P-Cells was that the force capacities of the pistons, which were used for the application of displacement reversals were exhausted in all the tests.

It was observed during PT4 test, that the P-Cells having a maximum rotation capacity of 0.055 rad exhibited a maximum rotation of approximately 0.035 rad on FT1. However, during the FT2 test, maximum P-Cell rotations remained at 0.014 rad before the force capacity of the pistons was exhausted.

In considerations on how significant plastic rotations may be obtained on the P-Cells under the same circumstances, i.e., the same test setup, frame and loading capacities, it was decided to reduce the number of P-Cells installed at the 1st story beams. As we know, a P-Cell consists of one central pin that is placed at the intersection of drums and two T/C components at its sides that exhibit plastic deformation under

tensile and compressive force reversals. Without its T/C components, a P-Cell behaves like a linear pin connection during reversed cyclic motion of the frame. This geometrical difference can be observed in Figure 4.21. The elevation view of the FT3 frame is also presented in Figure 4.22.

(a)   (b)

Figure 4.21: A P-Cell (a) with T/C components and (b) without T/C components, used as pin
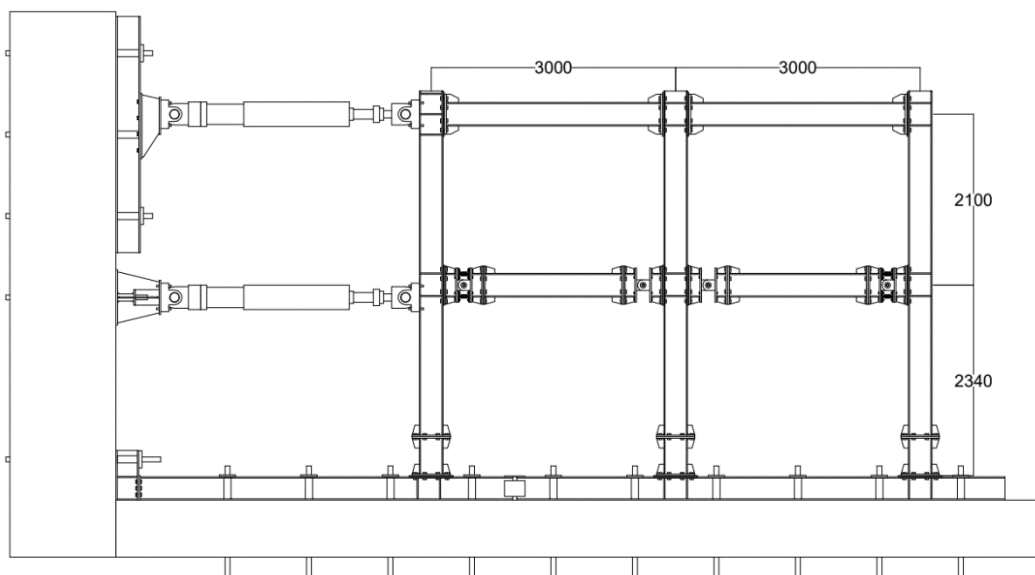

Figure 4.22: Elevation view of FT3 frame. Dimensions in mm.

By utilizing this formation, T/C components were mounted on the P-Cells on the outer ends of the first story (Figure 4.21a), and inner beam ends (Figure 4.21b) were left as pin-ended. In this way, it was aimed to achieve P-Cell rotations higher than the magnitudes observed in FT1 and FT2. Please note that P-Cells that were installed at the outer ends of the 1st story level were invariably named as P-Cell #1 and #4, for convenience.

FT3 Test

The test was performed under incremental reversed cyclic loading protocol presented in Figure 4.23 with uniform load profile during the entire test. Story displacements, P-Cell rotations, column base rotations, strains at the column bases and strains at the 2nd story beam ends and mid column top, which were expected to remain elastic, were continuously recorded during the test under that loading. Additionally, base shear force was recorded as the sum of lateral forces recorded from piston load cells, considering static equilibrium.
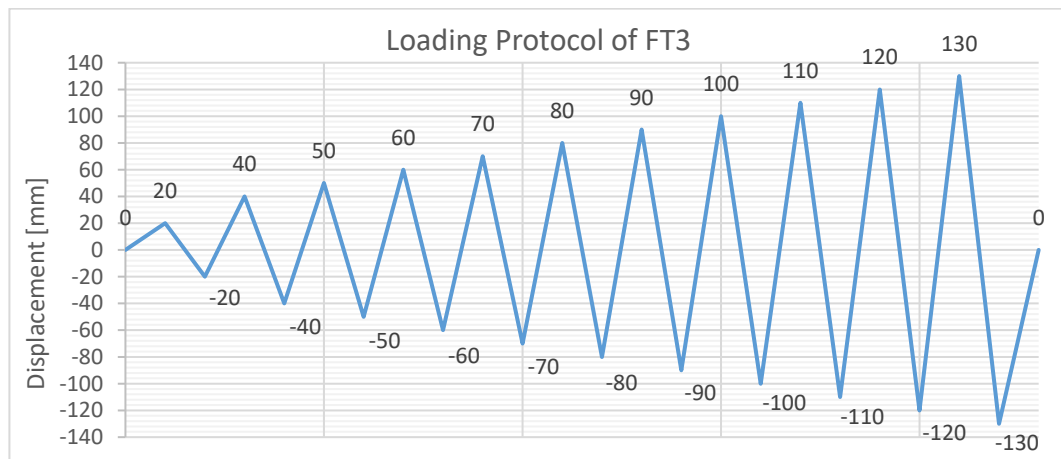
Figure 4.23: Displacement-imposed loading protocol of FT3 test, applied at the 2nd story level

Relation between those recorded parameters is presented in this section from Figure 4.24 to Figure 4.27 with the graphs listed below.

1. Story displacements vs. base shear force
2. P-Cell rotations vs. base shear force
3. Column base rotations vs. base shear force
4. Column base strains vs. base shear force
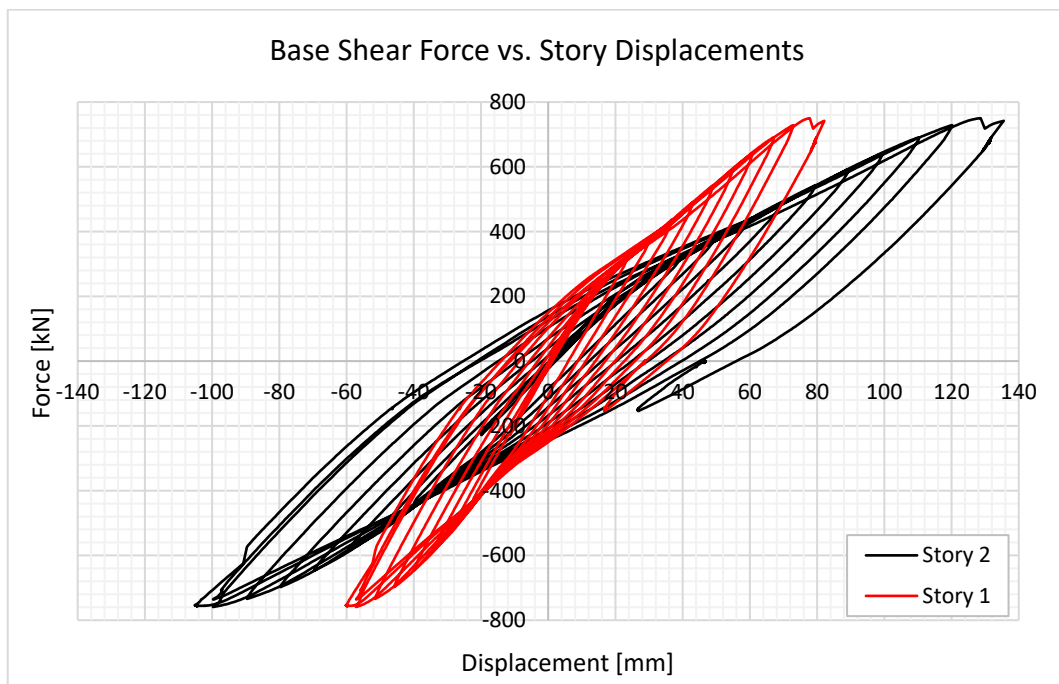
Figure 4.24: Base shear force – Story displacement relationships obtained during FT3 test

Figure 4.25: Base shear force – P-Cell rotation relationships obtained during FT3 test
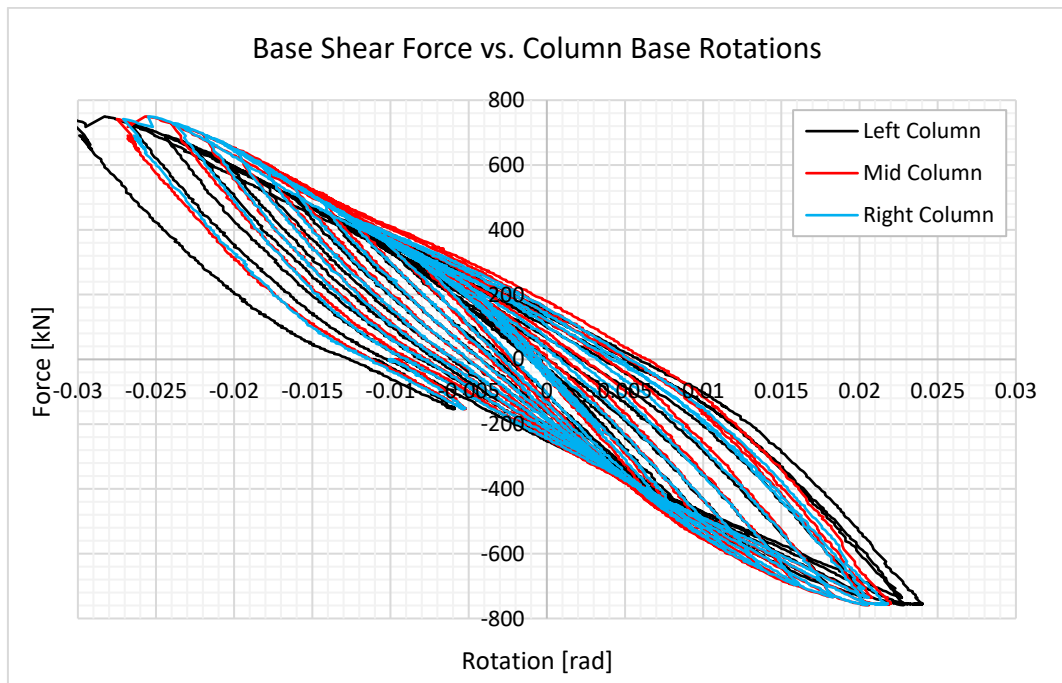
Figure 4.26: Base shear force – Column base rotation relationships obtained during FT3 test

145
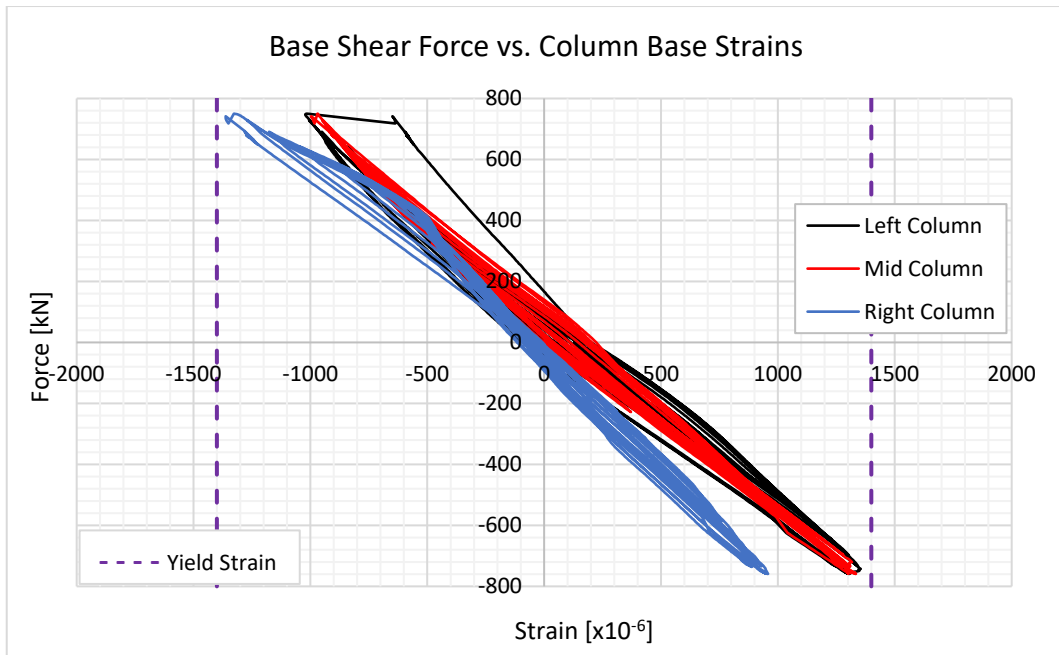
Figure 4.27: Base shear force – Column base strain relationships obtained during FT3 test
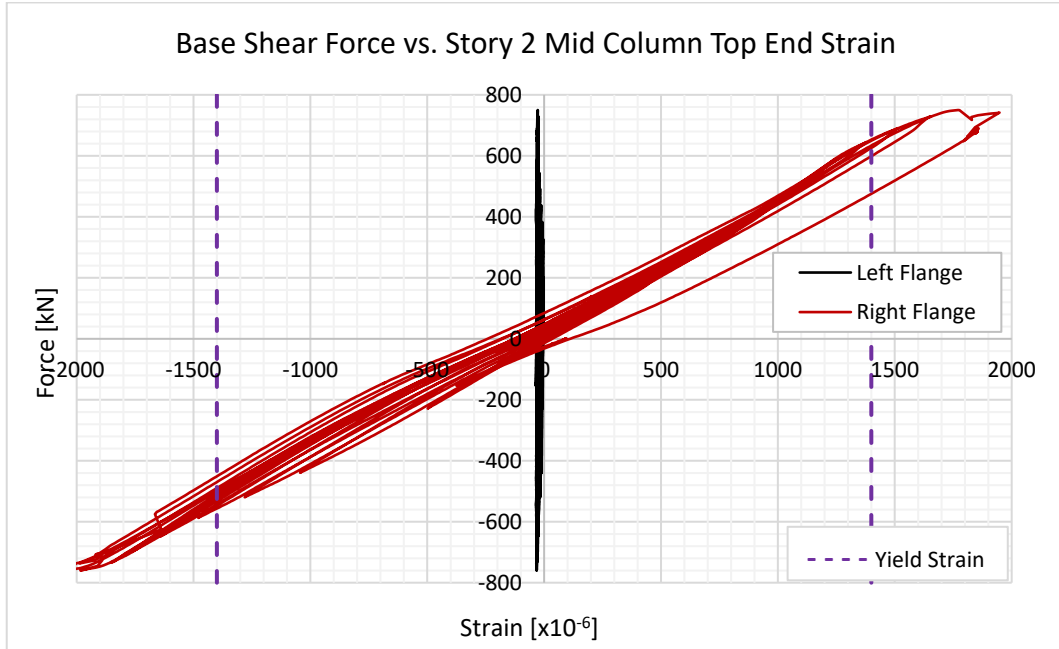
(a)

Figure 4.28: (a) Base shear force – 2nd story mid column top end, (b, c) Base shear force – 2nd story beam ends strain relationships obtained during FT3 test

(b)

(c)

Figure 4.28 (cont'd)

P-Cell #1   **θ_max = 0.027 rad**
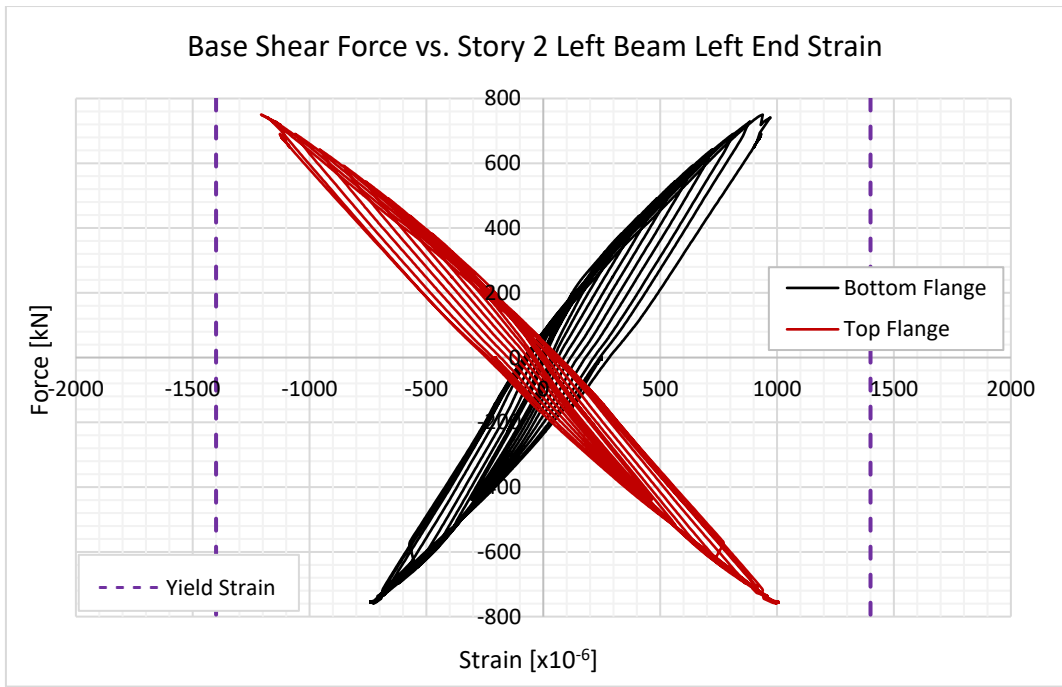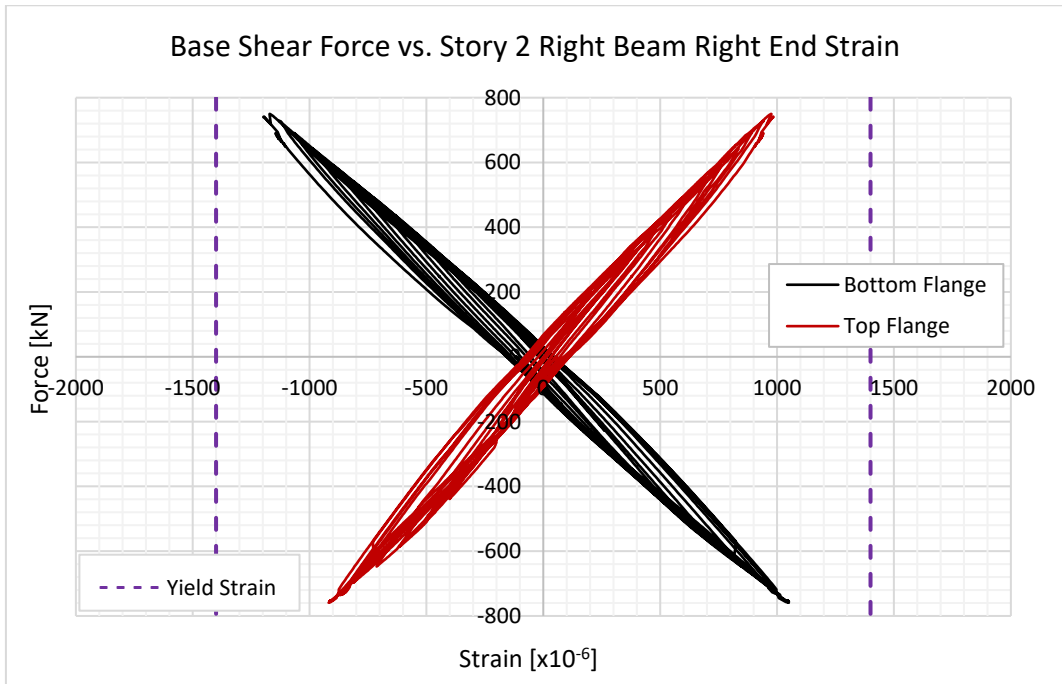
P-Cell #4   **θ_max = 0.025 rad**

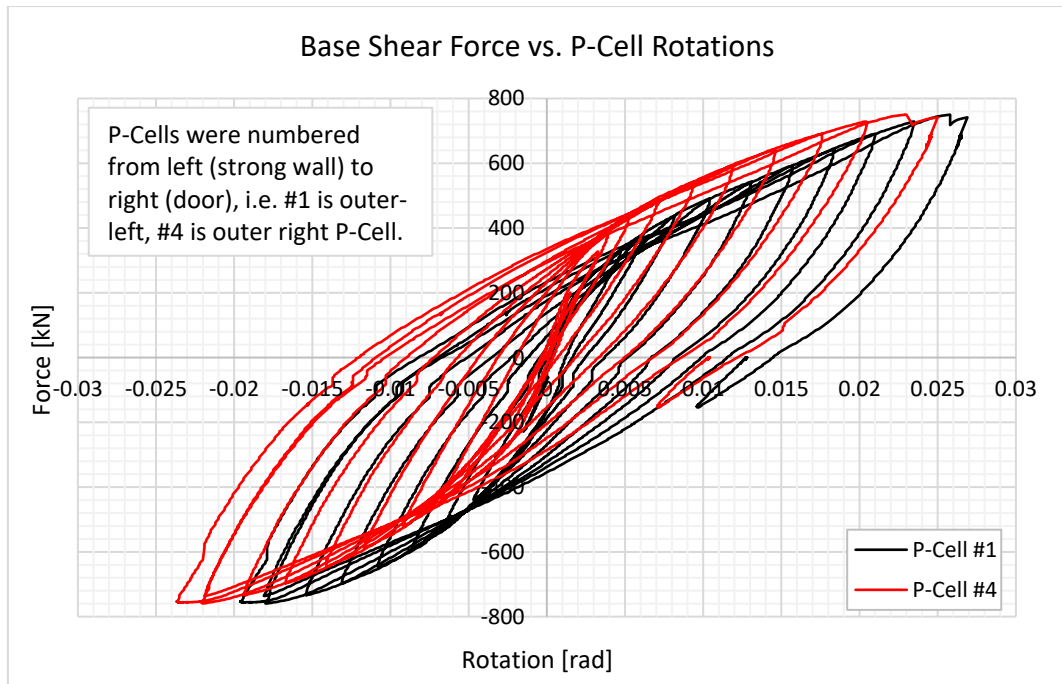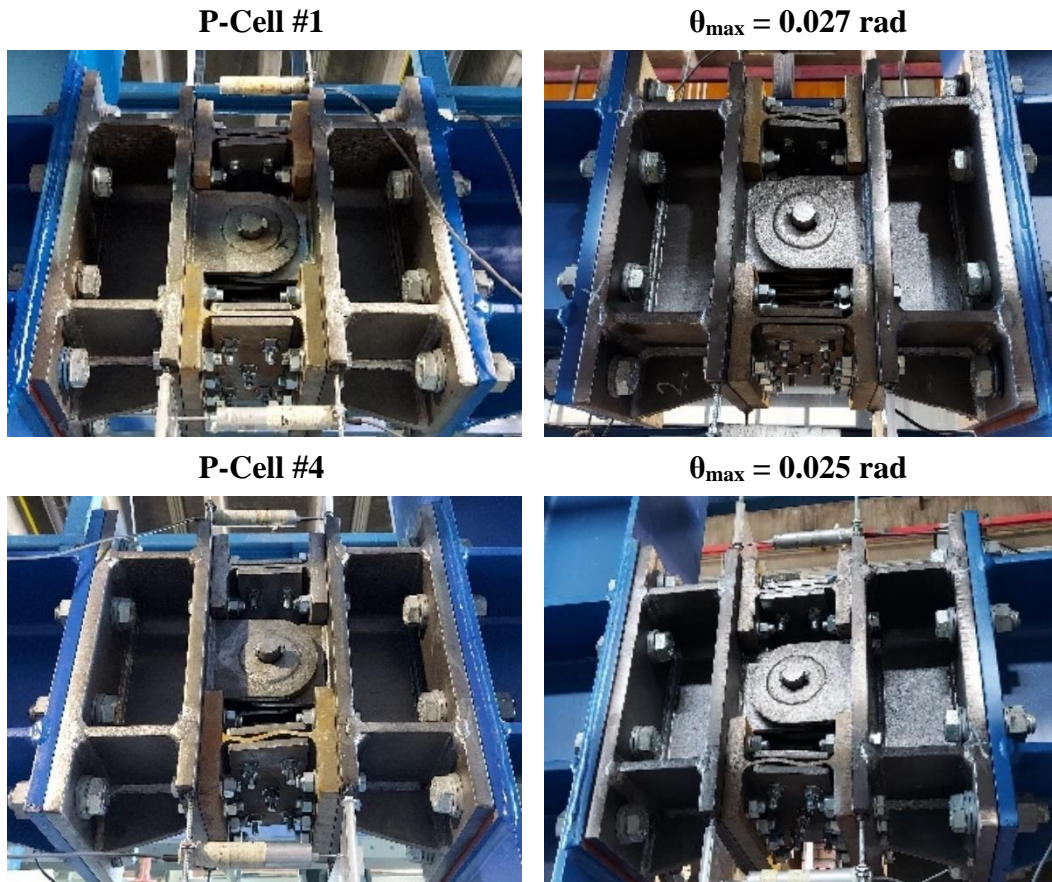Figure 4.29: Observed deformations and maximum rotations at P-Cells at the end of FT3 test

As mentioned in this section, the FT3 test was conducted with half number of P-Cells as compared to the first two tests, FT1 and FT2, and two pinned member ends at the middle column faces in order to decrease the global stiffness of the frame and achieve higher story displacements and consequently higher P-Cell rotations with the same applied load capacity, in order to observe significant plastic behavior and damage propagation of P-Cells. It was observed that reducing the number of P-Cells, which were installed to the 1st story beam ends, increased the plastic rotation demand on the remaining P-Cells, though it was still below the target rotation of around 0.04 rad.

Figure 4.16 shows that FT2 test with P-Cells mounted on all 1st story beam ends exhibited a maximum rotation of 0.014 rad in P-Cell #4, exhibiting the largest deformation, whereas the maximum P-Cell rotation recorded was around 0.027 rad, almost doubled. Corresponding deformations observed on the P-Cells are also presented in Figure 4.29. It can be concluded from the observations that even though the maximum P-Cells rotations, story drifts and P-Cell damages are significant both in their absolute values/status compared to previous test, there was still room for attaining the rotation and damage capacities of P-Cells on the test frame.

Figure 4.28 presents the strain data recorded at the 2nd story beam ends and column top end. The figure, along with the information regarding the material of the frame members, which were already given in previous sections reveals that 2nd story column top end exceeded the yield strain limit of the structural member at the latter stages of the FT3 test, while beam ends did not exhibit any yielding. In the meantime, the column bases remained in the elastic range without exhibiting any yielding during the test.

4.6   FT4 – FT5: One-Bay, Fixed-Base Frame with Two P-Cells

Frame tests FT1 through FT3 were performed on the 2D, two-story, two-bay steel frame, which was presented in Section 4.1. P-Cells with different numbers were installed at the ends of the 1st story beams in those tests. After their completion, one bay on the right side was dismantled, and a two-story, one-bay frame was constructed with two P-Cells at the ends of the 1st story beam. The material and geometrical properties, member end conditions and P-Cell properties remained the same. The rationale for creating the one-bay frame was to impose larger rotation demands on the P-Cells at lower lateral force demands by reducing the global frame stiffness.

Elevation view, and several details of the frame are shown in Figure 4.30. As seen in the figure, the test frame with the same end conditions as FT2 and FT3 frames has P-Cells at both ends of the 1st story beam. Displacements and corresponding lateral

forces are applied at both story levels with the same 500 kN-capacity actuator pistons.
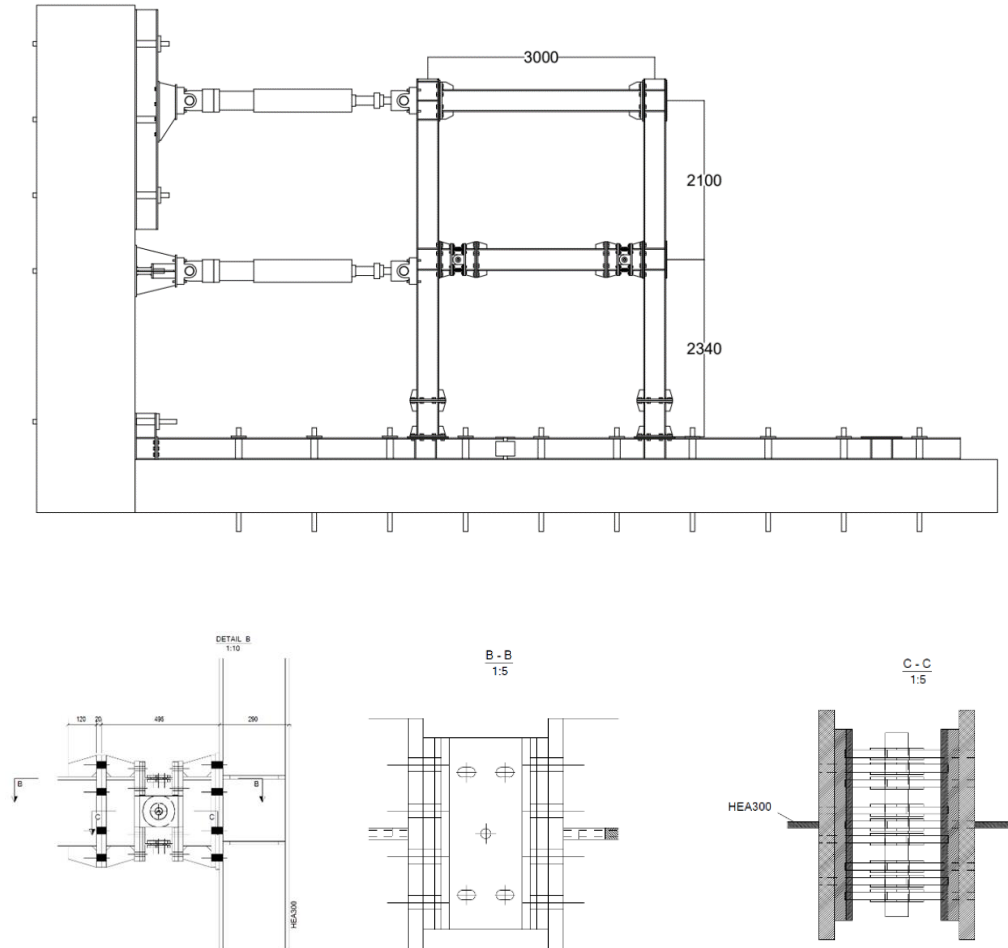
Figure 4.30: Elevation view and detail views of one-bay test frame and P-Cells

4.6.1 FT4 Test: Pseudo-Dynamic Test Series

The frame test series FT4 was the first tests, which were performed on the one-bay frame described at the beginning of this section, and it was also the test that a pseudo-dynamic loading with a ground motion record was applied to the frame sequentally

with increasing amplitudes of acceleration, by linearly scaling the acceleration values. Selected ground motion record is presented in Figure 4.31. Story displacements, P-Cell rotations, column base rotations, strains at the column bases and strains at the 2nd story beam ends and mid column top, which were expected to remain elastic, were continuously recorded during the series of test under pseudo-dynamic.
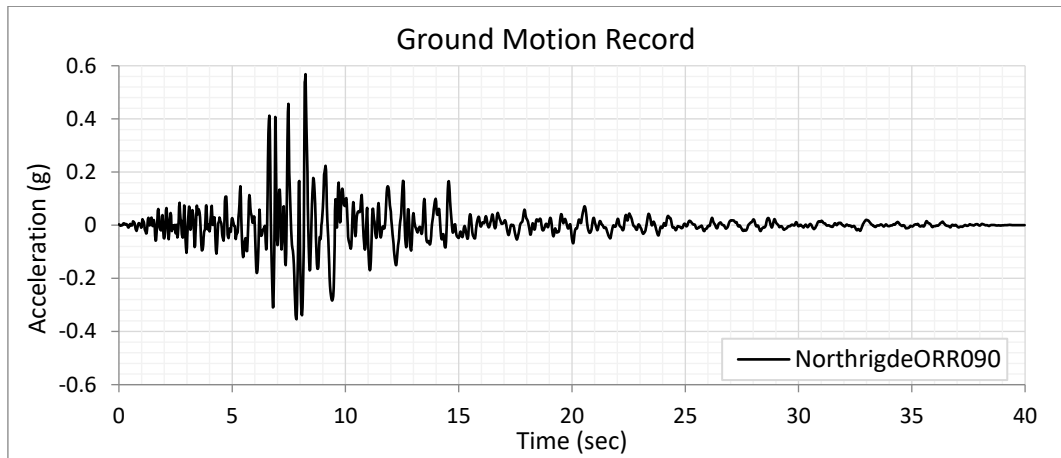
Figure 4.31: Ground motion record used in FT4 test series

The mass matrix of the frame that was imposed to the test actuator system and corresponding vibration periods of the frame are given below.

$$\bar{m} = \begin{bmatrix} 18 & 0 \\ 0 & 18 \end{bmatrix} tons \qquad \middle| \qquad \bar{T} = \begin{bmatrix} 0.424 \\ 0.086 \end{bmatrix} sec$$

Relation between those recorded parameters is presented in this section from Figure 4.32 to Figure 4.34 with the graphs listed below.

1. Story displacements vs. base shear force
2. P-Cell rotations vs. base shear force
3. Column base strains vs. base shear force
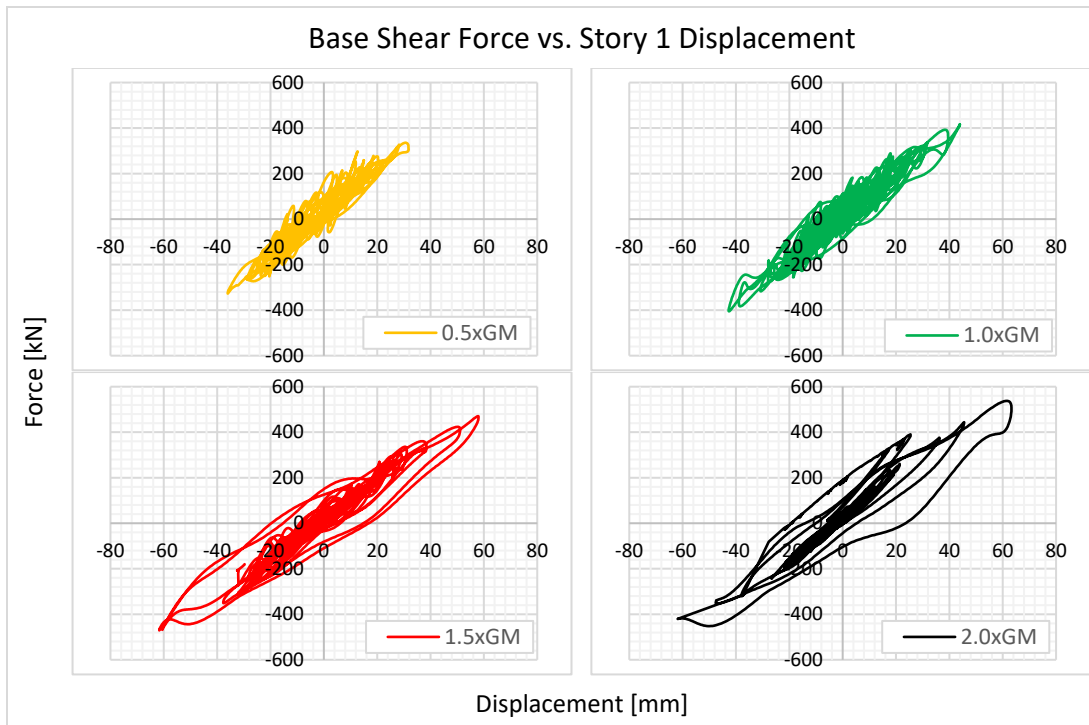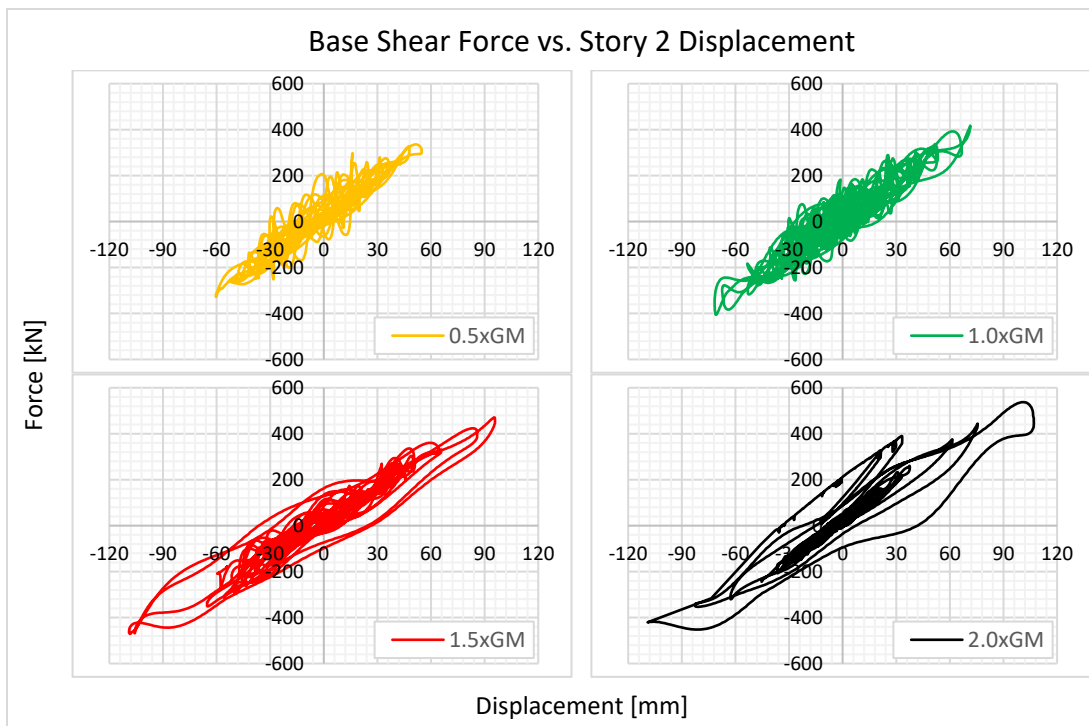
Figure 4.32: Base shear force –Story displacement relationships obtained during FT4 test series, (a) 1st Story (b) 2nd Story

152

Figure 4.33: Base shear force – P-Cell rotation relationships obtained during FT4 test series, (a) P-Cell #1 (b) P-Cell#2
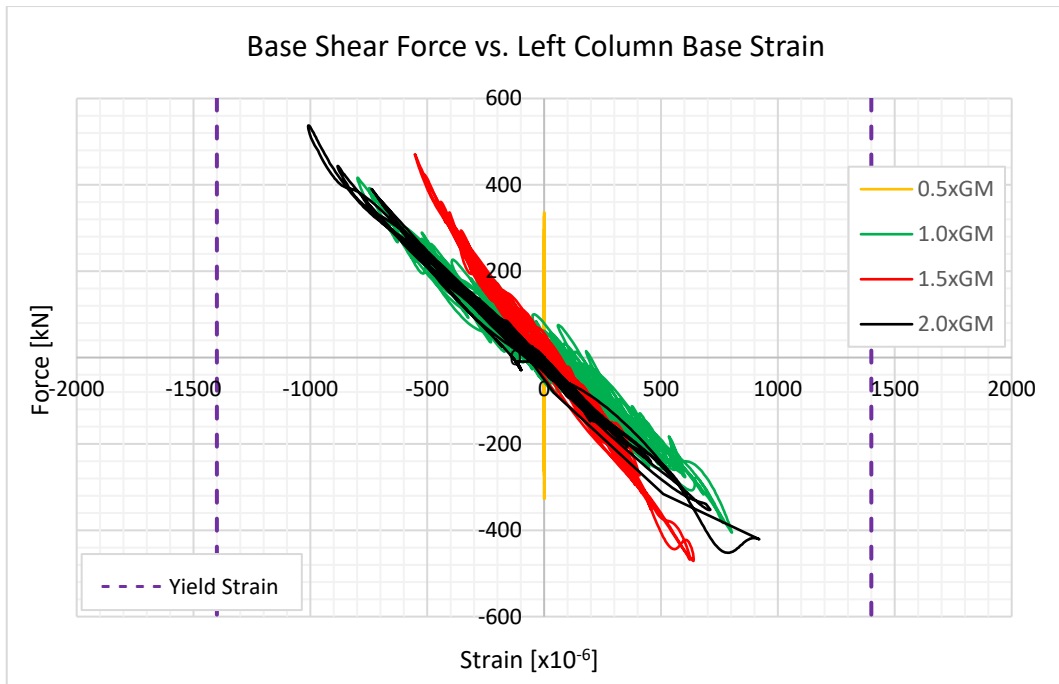
(a)
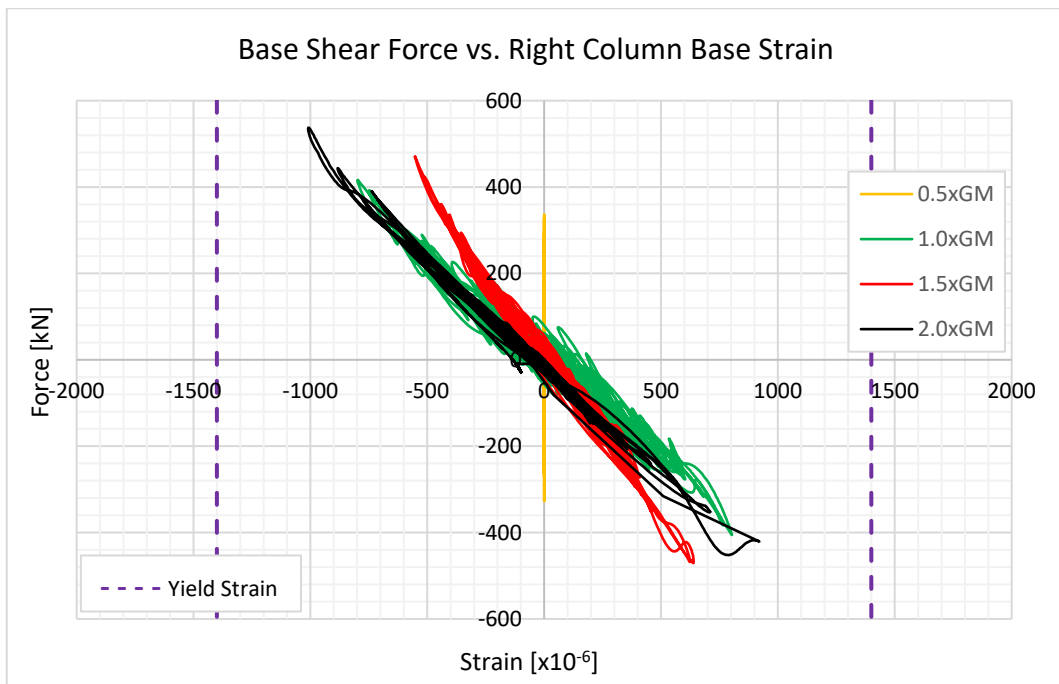
(b)

Figure 4.34: Base shear force – Column base strain relationships obtained during FT4 test series, (a) Left column (b) Right column

154

The first test of the series was performed under 50% of the original ground motion record, mainly in order to observe the behavior of the test frame and P-Cells with relatively smaller amplitudes of acceleration. Afterwards, the series of the tests was continued with 100% and 150% of the record. The fourth test of the series was started with 200% of the ground motion record, in order to further investigate the response of the test frame and P-Cells, after observing significant inelastic behavior during the test under 150% of the record. However, around 8th second of the record, at the strong motion region, the part that connects the Story 2 piston to the frame suddently ruptured, and the test was aborted at that time. Afterwards, it was decided not to repeat the same test and continue with a reversed cyclic test with new P-Cell units. That test is presented in subsequent section. The graphical results of the test performed with 200% record were presented along with the series, for convenience; however its results were not further discussed.

It can be observed from Figure 4.32 that the maximum Story 2 displacements obtained during the test series covering the application of 50%, 100% and 150% of the ground motion record were 60 mm, 72 mm, and 110 mm, respectively. The maximum obtained P-Cell rotations at the cycle of peak acceleration, on the other hand, were 0.01 rad, 0.014 rad, and 0.024 rad. P-Cell deformations at the end of the test performed under 150% record are also presented in Figure 4.35.

P-Cell #1 and #4 $\theta_{max} = 0.024$ **rad**
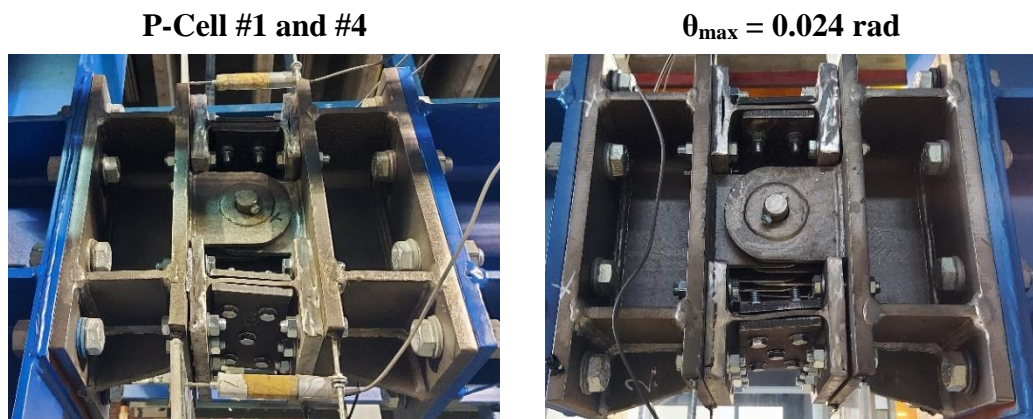
Figure 4.35: Observed deformations and maximum rotations at P-Cells at the end of FT4 test series

4.6.2   FT5: Reversed Cyclic Test

FT5 was the last test, which was conducted in the scope of the frame test phase of this study. It was performed on the one-bay frame described in Section 4.6, under the same incremental reversed cyclic loading protocol presented in Figure 4.36 with uniform load profile during the entire test. Story displacements, P-Cell rotations, column base rotations, strains at the column bases and strains at the 2nd story beam ends and mid column top, which were expected to remain elastic, were continuously recorded during the test under that loading. Additionally, base shear force was recorded as the sum of lateral forces recorded from piston load cells, considering static equilibrium.

Relation between those recorded parameters is presented in this section from Figure 4.37 to Figure 4.40 with the graphs listed below.

1. Story displacements vs. base shear force
2. P-Cell rotations vs. base shear force
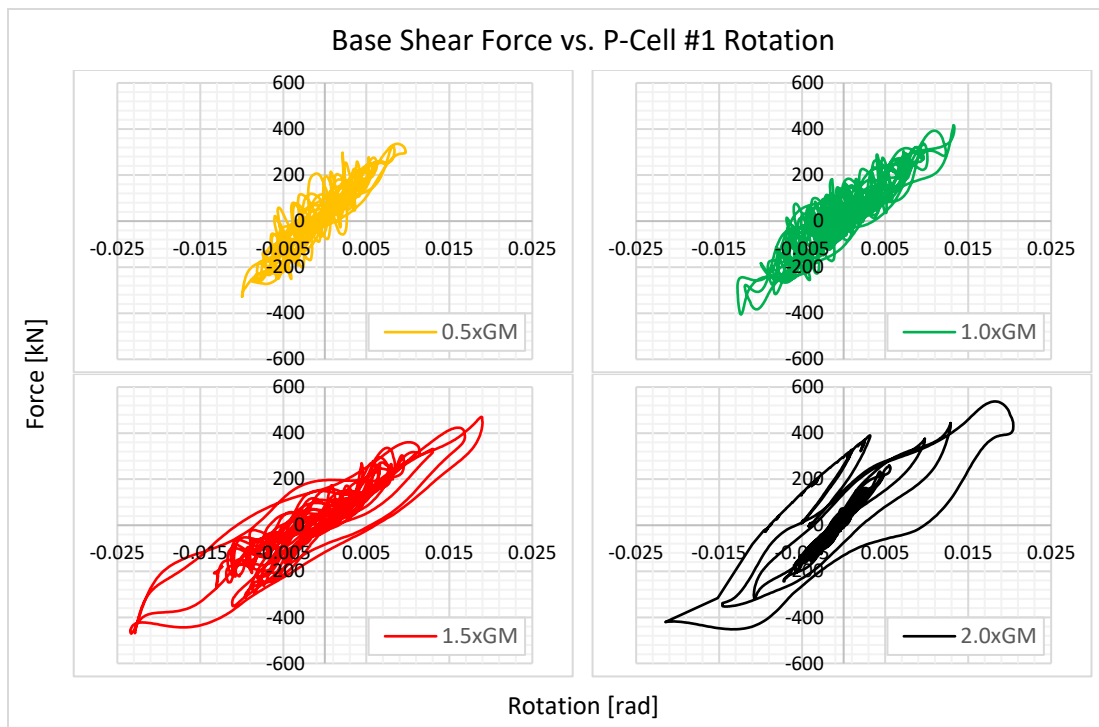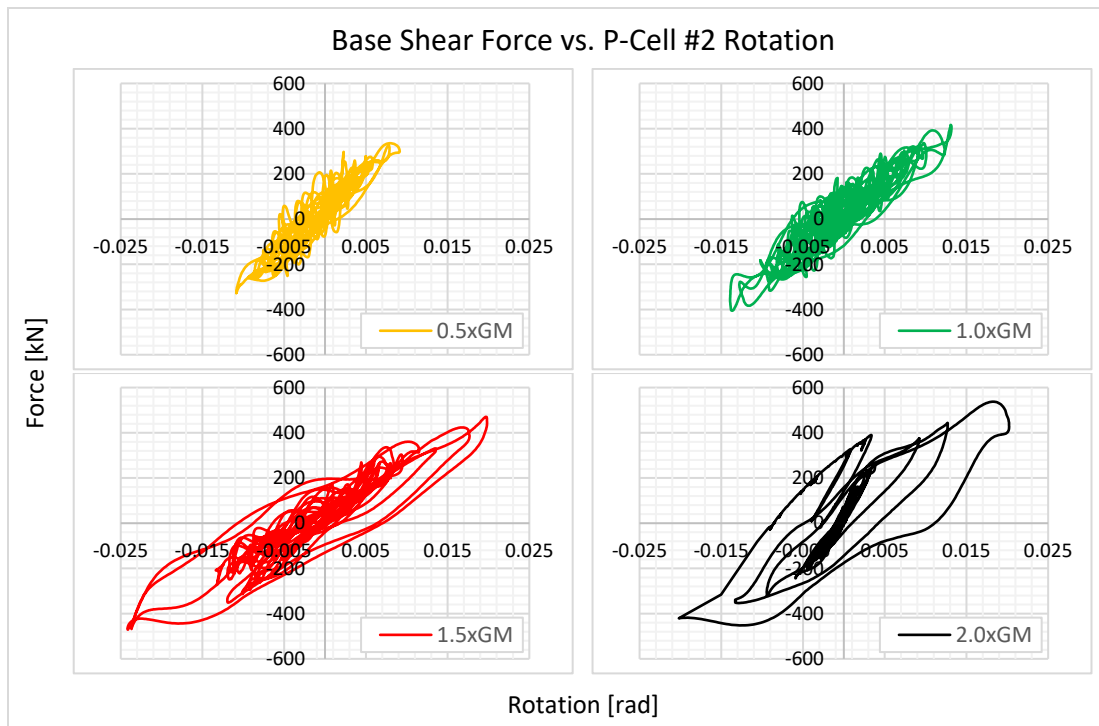3. Column base rotations vs. base shear force
4. Column base strains vs. base shear force
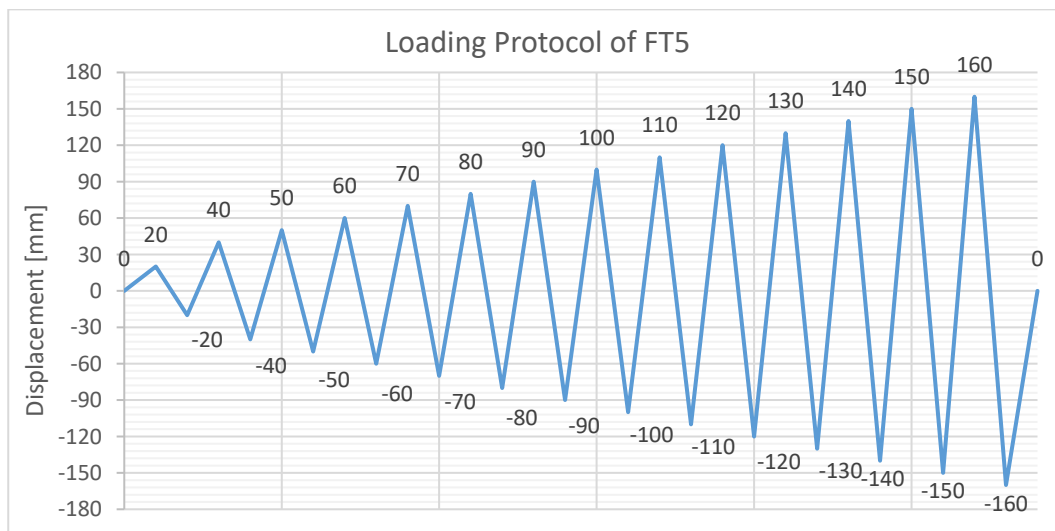
Figure 4.36: Displacement-imposed loading protocol of FT5 test, applied at the 2nd story level
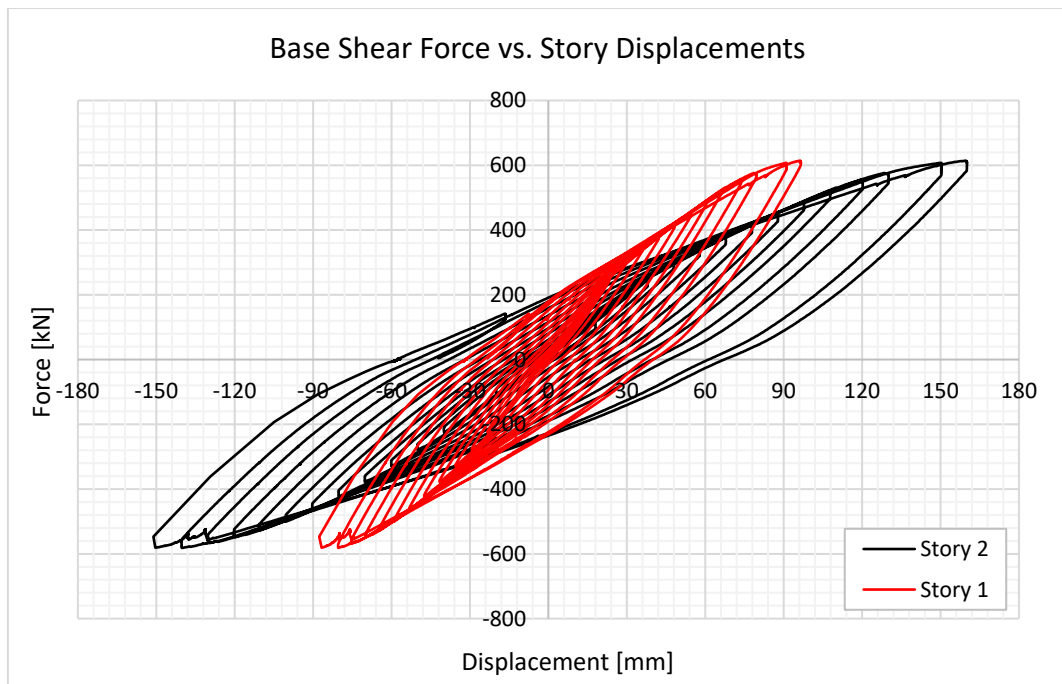
Figure 4.37: Base shear force – Story displacement relationships obtained during FT5 test
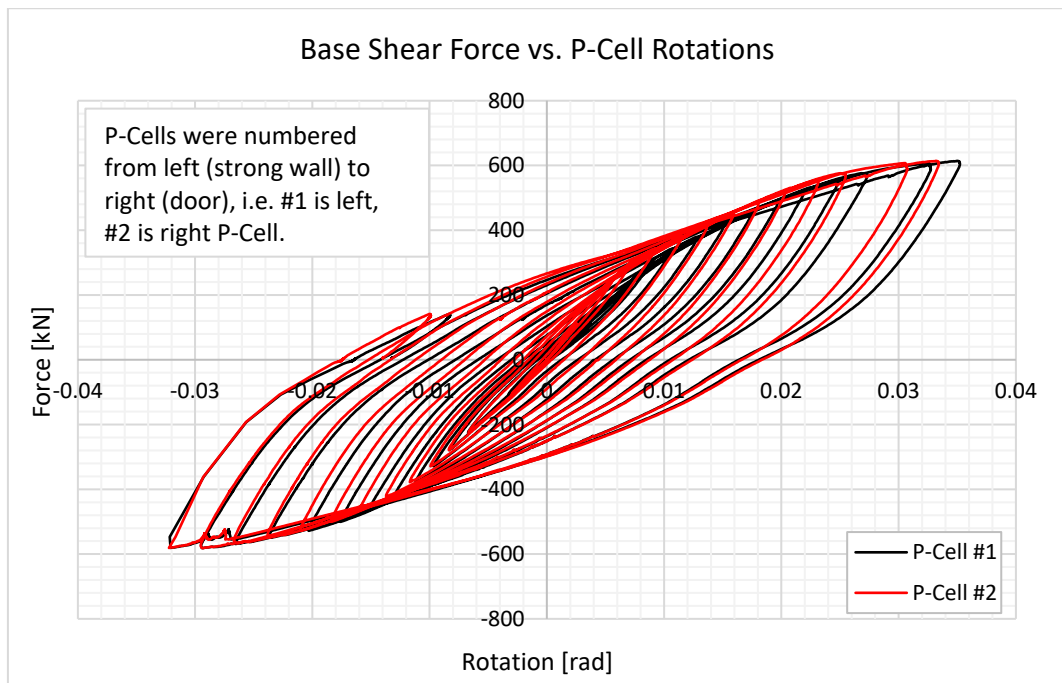
Figure 4.38: Base shear force – P-Cell rotation relationships obtained during FT5 test
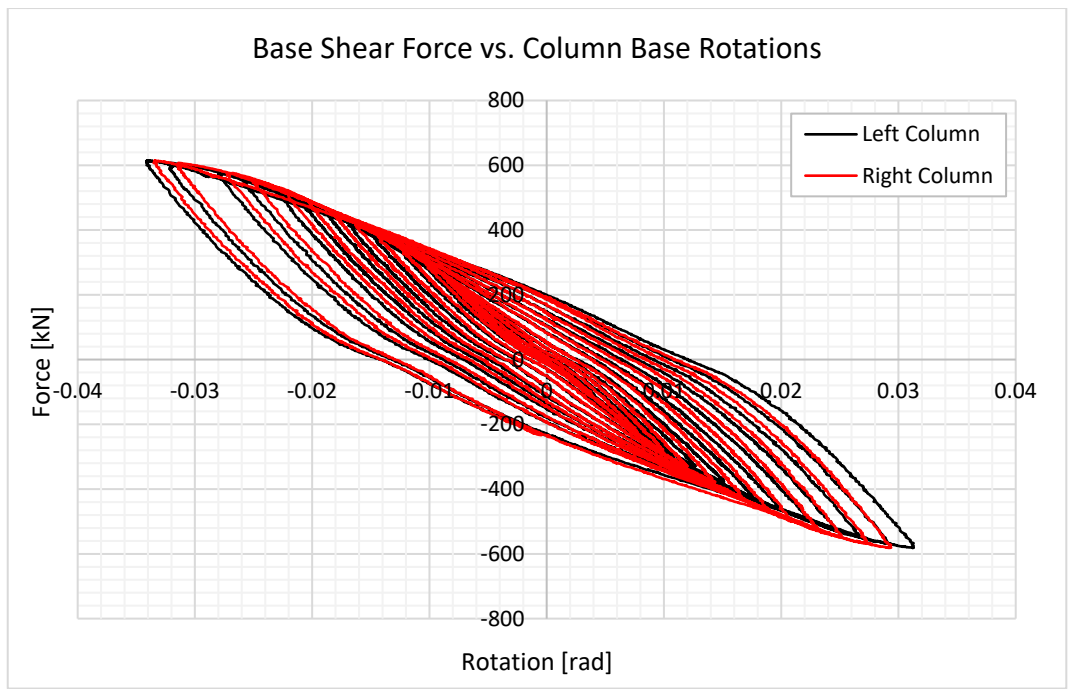
Figure 4.39: Base shear force – Column base rotation relationships obtained during FT5 test
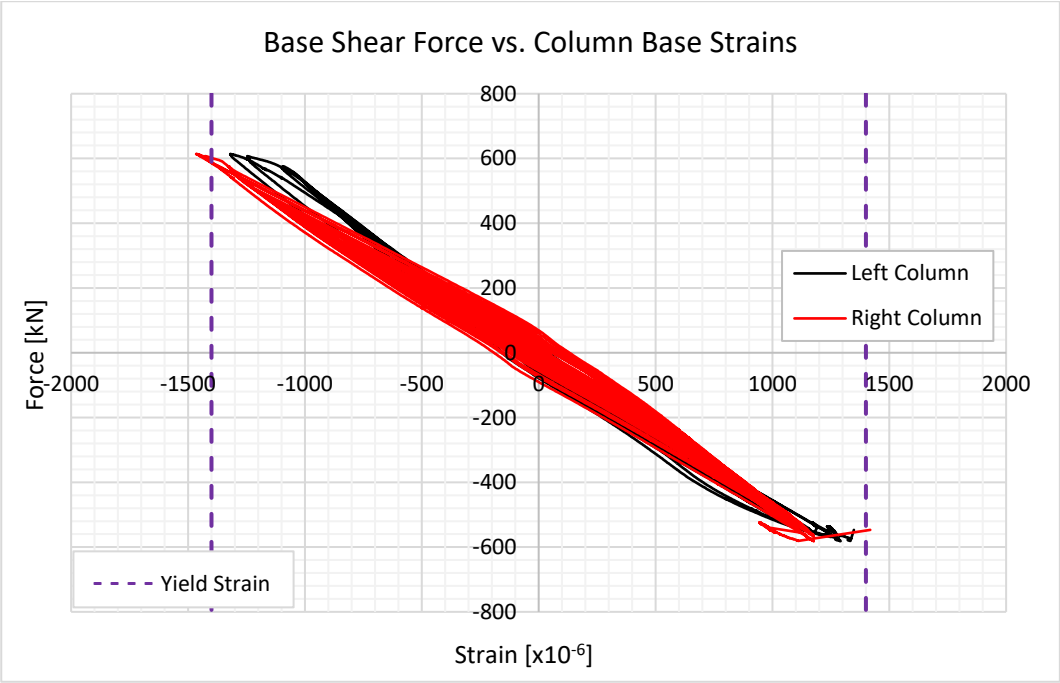
Figure 4.40: Base shear force – Column base strain relationships obtained during FT5 test
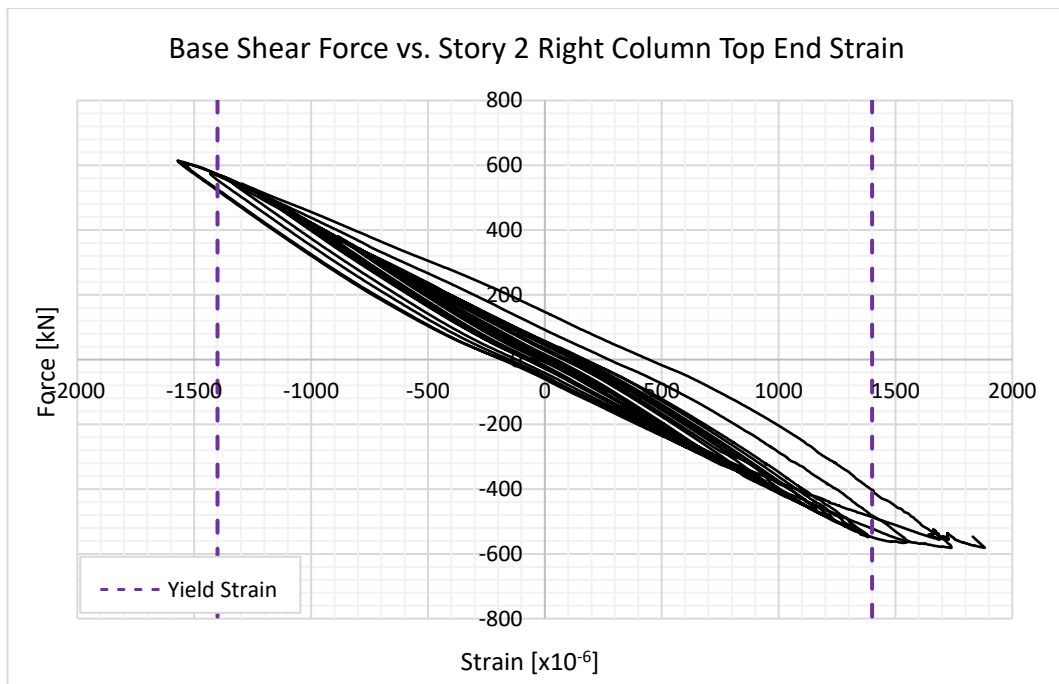
(a)
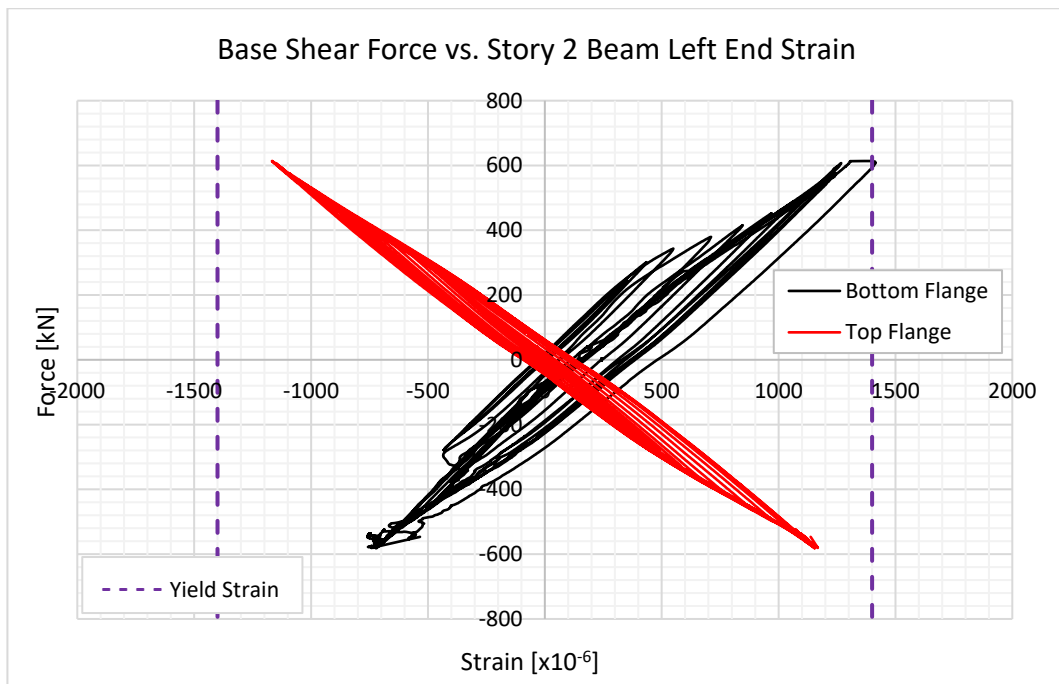
(b)

Figure 4.41: (a) Base shear force – 2nd story right column top end, (b) Base shear force – 2nd story beam left end strain relationships obtained during FT5 test

The constructional differences between FT3 and FT5, mainly the number of bays, which was already discussed in Section 4.6, led the frame reach relatively higher story displacements and consequently, higher P-Cell rotation capacities. Figure 4.38 reveals that both P-Cells exhibited rotation values around 0.035 rad, while observed deformations in Figure 4.42 are consistent with the results obtain during this test, and with the deformations observed in previous frame tests and PT4 test at similar rotation levels. It was also inferred from beam and column strains given in Figure 4.41 that the test frame essentially remained in the elastic range while interstory drift ratio at the 1st story exceeded 4% in the frame, and P-Cells exhibited large rotation values in the post-yield range.

P-Cell #1   **θ_{max} = 0.0352 rad**

P-Cell #4   **θ_{max} = 0.0334 rad**
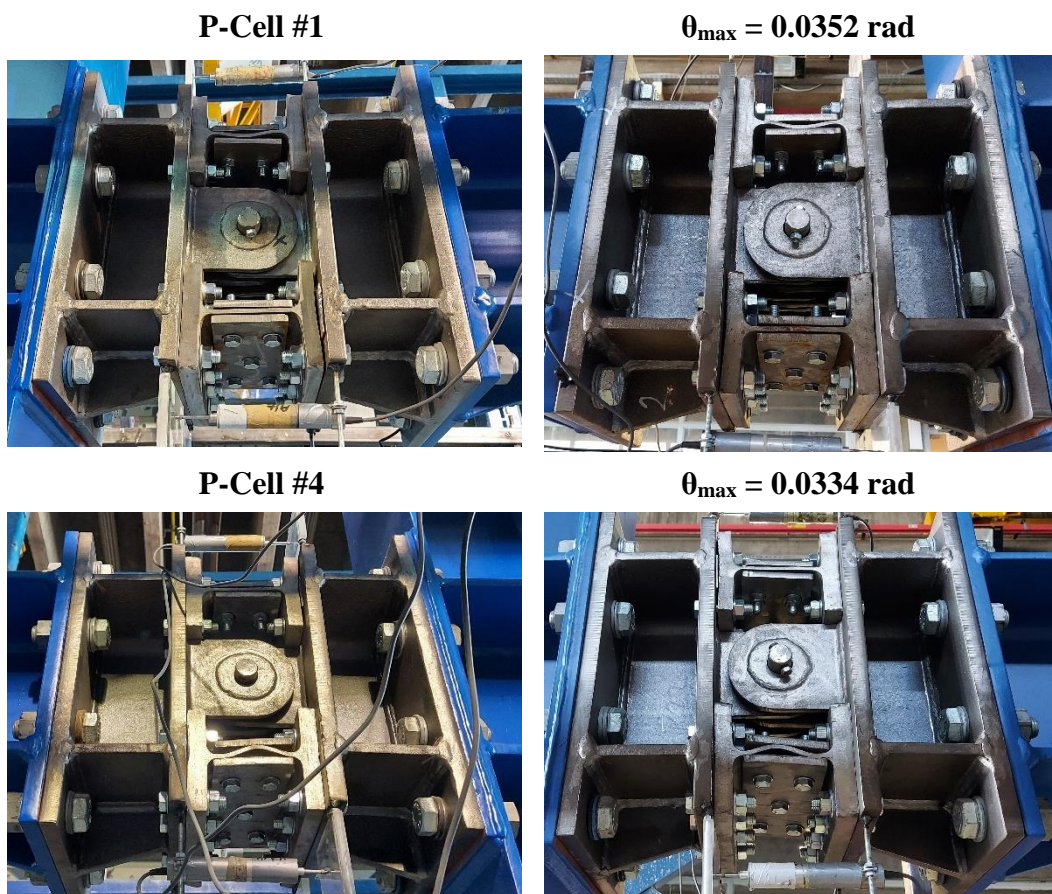
Figure 4.42: Observed deformations and maximum rotations at P-Cells at the end of FT5 Test

CHAPTER 5

SUMMARY AND CONCLUSIONS

5.1   Summary

The aim of this study has been to develop a plastic hinge device particularly for beam-ends where plastic hinge formation is expected due to adherence to the strong column-weak beam principle, a fundamental concept in seismic design. These devices serve multiple essential functions, including constraining plastic deformations within the defined beam zones, hence dissipating the stored hysteretic energy in the structure in this zone during earthquake motion, and being easily replaceable. This replaceability not only enhances the post-earthquake practicality, but also ensures compatibility with the existing structural framing system without altering the architectural design. In the development process, a central focus was placed on meeting the structural design criteria, and attention was given to ensuring interchangeability in the device components.

As an initial step, the methodology for the design of P-Cells and type testing was developed and presented in Chapter 3. By following those methodologies, an experimental setup was designed, produced, and tested in the structural laboratory, which would be suitable for the device design parameters and the resulting dimensions which was considered in the prototype design. The forces and displacements to be applied in the experiments were determined by considering the device capacities and it was ensured that the test specimens would attain the targeted performance.

The chapter also includes the results of P-Cell type tests, which were performed to observe the maximum rotational capacity and failure mode of each P-Cell type. For that purpose, incremental displacement reversals were applied to the test setup, which converted the displacements to imposed rotations on the P-Cell units. During this study, five different types were designed and tested before achieving the final P-Cell type that had stable and robust behavior, desired performance parameters, and ease of production and applicability. The first three P-Cell type tests were designed and manufactured with a particular number of mild steel bars as deforming T/C components, with changing geometries and detailing, especially in terms of their connection and replaceability. In the wake of the results and behavior those three tested P-Cell types, a preferable design was applied and tested on the last two types, which have H-section steel profiles as T/C components, in order to eliminate stability issues observed in the former designs and to obtain a much more stable configuration. In the final test, a consistent P-Cell type has been achieved, which could be tested at macro scale under the predetermined design values.

Furtermore, five different frame tests were performed on five different two-story steel frames equipped with P-Cells at designated locations in the beam-ends, of which the design and the results are elaborated in Chapter 4. The test frames that were designed and constructed had different configurations in terms of column end conditions, the locations of P-Cells, and the number of bays. The loading types were also different, mainly reversed cyclic and pseudo-dynamic loading. Each test frame was designed and constructed with the aim of achieving structural responses in the elastic range after the cyclic loading were completed, while plastic deformation demands were contained in the P-Cells which were placed at the first story beams. In the light of this objective, five different frame tests were performed under reversed cyclic, displacement-imposed loading procedures, while one of them was applied as a series of pseudo-dynamic loading with increasing acceleration amplitudes. During the tests, base shear force and story displacement relations and member-end strain values were recorded to observe the behavior of the test frame and the demands on a member/material level. Most importantly, P-Cell rotations and their deformation

162

patterns were recorded and observed to determine their performance and effect on a frame system level.

5.2   Conclusions

It is suitable to classify P-Cell design and the type tests into two main groups in terms of the design and the experimental behavior under reversed cyclic loading. The first class includes PT1-PT2 types and the second one includes PT3-PT4 types. In this case, the first class is the P-Cell design where deforming T/C components are in the form of circular hollow-section steel bars. The class has further three configurations with slight-to-moderate changes in terms of geometry, manufacturing details, and replaceability. The second class includes the P-Cell design where T/C components are manufactured from I- and H-section steel profiles, whose web regions are subjected to tensile and compressive forces and deformations under load reversals, and flanges are directly utilized for their replaceability.

According to the results obtained in this study, the following conclusions are drawn.

- Welding of a T/C component is a critical aspect of designing and manufacturing a P-Cell, in terms of both its location and the stresses that can develop on them during a seismic event. The premature rupture of T/C components that were employed in PT1 type at the welding locations exhibited this phenomenon clearly. Configuration changes in the T/C bars of the latter P-Cell types with the use of tapered bars, in other words increasing the sectional dimensions of the bar ends for the amount of welding and moving the end regions away from the mid regions was implemented as a remedy to the issue. However, even if rotation capacity was considerably increased relative to the preceding types, the PT2B unit had similar welding rupture at the end regions, which suggest that welding always cause a source of unpredictable failure.

- Torsional rotation along the P-Cell central axis is another issue that significantly affects the rotational capacity of the P-Cell. This behavior, mainly resulted from asynchronous yielding of T/C bars, were apparent in both PT2 types. Those two types, where the T/C bars were revised to have tapered sections at the ends for moving welding regions away from the regions of deformation, has relatively taller bars because of the addition of the height of tapers. The situation also made the bars more susceptible to biaxial double-curvature bending, and decreased the torsional stiffness of the P-Cell. Consequently, torsional rotation and its resulting effect on early reach to the strain capacity of T/C bars reduced the rotational capacity of the P-Cell in bending.

- The issue of undesired torsional rotation along the P-Cell led to significant changes in the the type of T/C component and consequent P-Cell design. In order to eliminate the torsional behavior of the P-Cell under bending, torsional stiffness was significantly increased by placing I- and H-section steel profiles in transverse direction in the P-Cell as tension/compression component, where T/C bars were placed side-by-side in the design of first group. The first unit that this design change was utilized, PT3 unit, had an I-section steel profile as the T/C component. It was observed during the type test that torsional behavior was properly eliminated; however T/C components exhibited premature buckling under compression before significant yielding occurred during incremental load reversals.

- PT3 type test revealed that buckling of the web of steel profile T/C components before yielding or at early stages of post-yield under compression is a significant weakness that influence the performance and behavior of the P-Cell. In order to prevent such buckling behavior and attain designated P-Cell rotation targets, implementation of buckling-restraint plates at both sides of the T/C webs were considered and applied to PT4 type, which was the final design of P-Cell. Buckling-restraint plates were connected to the web of T/C components with the aim of ensuring the

components to deform freely under tension-compression load reversals at the early stages of post-yield behavior. However, at the advanced stages of load reversals, restrained buckling under compression eventually exhausted the strain capacity of T/C components. As a conclusion, design and manufacture of T/C components with steel profiles having high lateral stiffness and plate restraints achieve a P-Cell composition having a stable rotational behavior and the desired moment capacity.

- All P-Cell types exhibited an overstrength ratio varying between 1.6 and 2.4, which is a result of the mechanical properties of the of T/C component material. It is suggested that this value of overstrength should be used in the capacity design of the connecting members of framing system.

While the first stage of the investigation is the development of P-Cell and the type testing of different configurations, the second stage is the frame tests performed on the two-story steel frames with different designs as a proof of concept. The frames were designed and constructed in the search of achieving larger P-Cell rotation demands in order to investigate the behavior and performance of P-Cells and their effect on frame response. As presented in Chapter 4, five different frame tests are included in the frame test stage. Apart from the FT4 and FT5, which were carried out on the same one-bay frame design, other frame tests were carried out on different frames having different end conditions and P-Cell configurations where they are placed at the 1st story beams. In the light of the objectives of frame testing, the derived conclusions are listed below.

- The most prominent rationale for the development of P-Cell is that the plastic hinge formations at a framing system under severe load reversals are constrained at the designated regions where P-Cells are located, and the remaining structural members essentially remain in the linear elastic range. As clearly presented in the sections for all the frame tests, the structural members that were considered as critical as a result of frame analysis were investigated and strain values at their end regions were recorded. The results

for all frame tests revealed that while the frame reached large displacement values, and P-Cells exhibited significant post-yield behavior and deformations, critical structural members such as column ends and 2nd story beam members remained in the elastic range. The conclusion is considered as an indication of the effectiveness of P-Cell in imitating the plastic hinge behavior in a framing system.

- The responses of P-Cells for different frames where P-Cells were always mounted at the 1st story beam ends but at varying amounts revealed the following observations. Independent from the amplitude of rotation values, outer P-Cells exhibited rotation values relatively higher than the inner P-Cells in FT1 and FT2 tests where all beam ends were equipped with P-Cells. In FT3, where only outer P-Cell locations were equipped and inner locations were left as pinned, and in FT4, where there was only one-bay with both end equipped, the response of the P-Cells were almost perfectly symmetrical.

- Replaceability is another feature of a P-Cell, since the deforming damaged T/C components were designated as a replaceable member of the device after a severe earthquake. During the frame test stage, the same frame was repeatedly used for all the frame tests, with one slight alteration as the change in column base from pin to fixed-end. Apart from that, one-bay frame was constructed by just dismantling one bay from the two-bay frame. The only replacement in the frame between the frame tests was the significantly deformed T/C components at the end of each test. The experience and observations during the practice indicated that the replaceability of T/C components are fairly easy-to-apply.

REFERENCES

American Society of Civil Engineers, ASCE. (2022). *Minimum design loads and associated criteria for buildings and other structures*. (ASCE/SEI 7-22). https://www.asce.org/

Black, C. J., Makris, N., & Aiken, I. D. (2004). Component Testing, Seismic Evaluation and Characterization of Buckling-Restrained Braces. *Journal of Structural Engineering*, *130*(6), 880–894. https://doi.org/10.1061/(asce)0733-9445(2004)130:6(880)

Dimakogianni, D., Dougka, G., & Vayas, I. (2015). Seismic behavior of frames with innovative energy dissipation systems (FUSEIS1-2). *Engineering Structures*, *90*, 83–95. https://doi.org/10.1016/j.engstruct.2015.01.054

Dimakogianni, D., Dougka, G., Vayas, I., & Karydakis, P. (2012). Innovative seismic-resistant steel frames (FUSEIS 1-2) - experimental analysis. *Steel Construction*, *5*(4), 212–221. https://doi.org/10.1002/stco.201210026

Englekirk, R. E. (1995). Development and testing of a ductile connector for assembling precast concrete beams and columns. *PCI Journal*, *40*(2), 36–51. https://doi.org/10.15554/pcij.03011995.36.51

European Committee for Standardization, CEN. (2018). *Anti-seismic devices*. (EN 15129:2018). https://www.en-standard.eu/

Fitzgerald, T. F., Anagnos, T., Goodson, M., & Zsutty, T. (1989). Slotted bolted connections in aseismic design for concentrically braced connections. *Earthquake Spectra*, *5*(2), 383–391. https://doi.org/10.1193/1.1585528

Grigorian, C. E., Yang, T. S., & Popov, E. P. (1993). Slotted Bolted Connection Energy Dissipators. *Earthquake Spectra*, *9*(3), 491–504. https://doi.org/10.1193/1.1585726

Hao, X. Y., Li, H. N., Li, G., & Makino, T. (2014). Experimental investigation of steel structure with innovative H-type steel unbuckling braces. *Structural Design of Tall and Special Buildings*, *23*(14), 1064–1082. https://doi.org/10.1002/tal.1108

Huang, L., Zhou, Z., Huang, X., & Wang, Y. (2020). Variable friction damped self-centering precast concrete beam–column connections with hidden corbels: Experimental investigation and theoretical analysis. *Engineering Structures*, *206*. https://doi.org/10.1016/j.engstruct.2019.110150

Jaisee, S., Yue, F., & Ooi, Y. H. (2021, May 15). A state-of-the-art review on passive friction dampers and their applications. *Engineering Structures*. Elsevier Ltd. https://doi.org/10.1016/j.engstruct.2021.112022

Javanmardi, A., Ibrahim, Z., Ghaedi, K., Benisi Ghadim, H., & Hanif, M. U. (2020). State-of-the-Art Review of Metallic Dampers: Testing, Development and Implementation. *Archives of Computational Methods in Engineering*, *27*(2), 455–478. https://doi.org/10.1007/s11831-019-09329-9

Keh-Chyuan Tsai, Huan-Wei Chen, Ching-Ping Hong, & Yung-Feng Su. (1993). Design of steel triangular plate energy absorbers for seismic-resistant construction. *Earthquake Spectra*, *9*(3), 505–528. https://doi.org/10.1193/1.1585727

Kelly, J. M., Skinner, R. I., & Heine, A. J. (1972). Mechanisms of energy absorption in special devices for use in earthquake resistant structures. *Bulletin of the New Zealand Society for Earthquake Engineering*, 5(3), 63–88. https://doi.org/10.5459/bnzsee.5.3.63-88

Kimura, K., Takeda, Y., Yoshioka, K., Furuya, N., & Takemoto, Y. (1976). An experimental study on braces encased in steel tube and mortar. *Proc. Annual Meeting of the Architectural Institute of Japan*, Japan (in Japanese).

Lee, D., & Taylor, D. P. (2001). Viscous damper development and future trends. *Structural Design of Tall Buildings*, *10*(5), 311–320. https://doi.org/10.1002/tal.188

Li, H. N., & Li, G. (2007). Experimental study of structure with "dual function" metallic dampers. *Engineering Structures*, *29*(8), 1917–1928. https://doi.org/10.1016/j.engstruct.2006.10.007

Lukkunaprasit P, Wanitkorkul A, & Filiatrault A. (2004). Performance deterioration of slotted-bolted connection due to bolt impact and remedy by restrainers. 13th *World Conference on Earthquake Engineering, Vancouver, B.C., Canada*.

Makris, N. (1998). Viscous Heating of Fluid Dampers. I: Small-Amplitude Motions. *Journal of Engineering Mechanics*, *124*(11), 1210–1216. https://doi.org/10.1061/(asce)0733-9399(1998)124:11(1210)

Makris, N., Roussos, Y., Whittaker, A. S., & Kelly, J. M. (1998). Viscous Heating of Fluid Dampers. II: Large-Amplitude Motions. *Journal of Engineering Mechanics*, *124*(11), 1217–1223. https://doi.org/10.1061/(asce)0733-9399(1998)124:11(1217)

Mochizuki, N., Murata, Y., Andou, N., & Takahashi, S. (1980). An experimental study on buckling of unbonded braces under centrally applied loads. *Proc. Annual Meeting of the Architectural Institute of Japan*, Japan (in Japanese).

Nakaki, S. D., Englekirk, R. E., & Plaehn, J. L. (1994). Ductile Connectors for a Precast Concrete Frame. *PCI Journal*, *39*(5), 46–59. https://doi.org/10.15554/pcij.09011994.46.59

Open System for Earthquake Engineering Simulation. (2022). V. 3.3.0. Pacific Earthquake Engineering Research Center. Berkeley, CA.

Pall, A. S., & Marsh, C. (1982). Response of Friction Damped Braced Frames. *Journal of the Structural Division*, *108*(6), 1313–1323. https://doi.org/10.1061/JSDEAG.0005968

Pall, A. S., Marsh, C., & Fazio, P. (1980). Friction Joints for Seismic Control of Large Panel Structures. *Journal - Prestressed Concrete Institute*, *25*(6), 38–61. https://doi.org/10.15554/pcij.11011980.38.61

Rees, D. W. A. (2009). Mechanics of Optimal Structural Design: Minimum Weight Structures. In *Mechanics of Optimal Structural Design: Minimum Weight Structures*. J. Wiley. https://doi.org/10.1002/9780470749784

Reinhorn, A. M., Li, C., & Constantinou, M. C. (1995). Experimental and analytical investigation of seismic retrofit of structures with supplemental damping. Part I: Fluid viscous damping devices. *Technical Rep. No. NCEER-95–0001, National Center for Earthquake Engineering Research, State Univ. of New York at Buffalo*, Buffalo, N.Y.

Robinson, W. H., & Tucker, A. G. (1977). A lead-rubber shear damper. *Bulletin of the New Zealand Society for Earthquake Engineering*, *10*(3), 151–153. https://doi.org/10.5459/bnzsee.10.3.151-153

Saravanan, M., Goswami, R., & Palani, G. S. (2021). Energy dissipative beam-column connection for earthquake resistant moment frames. *Journal of Constructional Steel Research*, *176*. https://doi.org/10.1016/j.jcsr.2020.106428

Shen, Y., Christopoulos, C., Mansour, N., & Tremblay, R. (2011). Seismic Design and Performance of Steel Moment-Resisting Frames with Nonlinear

Replaceable Links. *Journal of Structural Engineering*, *137*(10), 1107–1117. https://doi.org/10.1061/(asce)st.1943-541x.0000359

Skinner, R. I., Kelly, J. M., & Heine, A. J. (1974). Hysteretic dampers for earthquake-resistant structures. Earthquake Engineering and Structural Dynamics, 3(3), 287-296. https://doi.org/10.1002/eqe.4290030307

Skinner, R. I., Tyler, R. G., Heine, A. J., & Robinson, W. H. (1980). Hysteretic dampers for the protection of structures from earthquakes. *Bulletin of the New Zealand Society for Earthquake Engineering*, 13(1), 22–36. https://doi.org/10.5459/bnzsee.13.1.22-36

Symans, M. D., & Constantinou, M. C. (1998). Passive fluid viscous damping systems for seismic energy dissipation. *J. of Earthquake Technology, 35*(4), 185–206.

Wang, C. L., Liu, Y., Zheng, X., & Wu, J. (2019). Experimental investigation of a precast concrete connection with all-steel bamboo-shaped energy dissipaters. *Engineering Structures*, *178*, 298–308. https://doi.org/10.1016/j.engstruct.2018.10.046

Wang, C. L., Liu, Y., & Zhou, L. (2018). Experimental and numerical studies on hysteretic behavior of all-steel bamboo-shaped energy dissipaters. *Engineering Structures*, *165*, 38–49. https://doi.org/10.1016/j.engstruct.2018.02.078

Watanabe, A., Hitomoi, Y., Saeki, E., Wada, A., & Fujimoto, M. (1988). Properties of braces encased in buckling-restraining concrete and steel tube. *Proc., 9th World Conf. on Earthquake Engineering*, Vol. IV, Tokyo-Kyoto, Japan, 719–724.

Whittaker, A. S., Bertero, V. V., Thompson, C. L., & Alonso, L. J. (1991). Seismic Testing of Steel Plate Energy Dissipation Devices. *Earthquake Spectra*, *7*(4), 563–604. https://doi.org/10.1193/1.1585644

Wu, B., Zhang, J., Williams, M. S., & Ou, J. (2005). Hysteretic behavior of improved Pall-typed frictional dampers. *Engineering Structures*, *27*(8), 1258–1267. https://doi.org/10.1016/j.engstruct.2005.03.010

Zayas, V. A., Low, S. S., & Mahin, S. A. (1990). A Simple Pendulum Technique for Achieving Seismic Isolation. *Earthquake Spectra*, *6*(2), 317–333. https://doi.org/10.1193/1.1585573

Zhao, J., Wu, B., & Ou, J. (2011). A novel type of angle steel buckling-restrained brace: Cyclic behavior and failure mechanism. *Earthquake Engineering and Structural Dynamics*, *40*(10), 1083–1102. https://doi.org/10.1002/eqe.1071

Zheng, J., Zhang, C., & Li, A. (2020). Experimental investigation on the mechanical properties of curved metallic plate dampers. *Applied Sciences (Switzerland)*, *10*(1). https://doi.org/10.3390/app10010269

CURRICULUM VITAE

Surname, Name: Tanışer, Sadun

EDUCATION

Degree	Institution	Year of Graduation
MS	METU Civil Engineering	2013
BS	METU Civil Engineering	2010
High School	Lüleburgaz Anadolu High School, Kırklareli	2005

FOREIGN LANGUAGES

Advanced English

PUBLICATIONS

1. Tanışer S., Sucuoğlu H., Topkaya C. and Azak S. "A Plastic Hinge Cell for Beam to Column Connections", Earthquake Engineering and Structural Dynamics. (2024) (Submitted).

2. Kaatsız K., Alıcı F.S., Sucuoğlu H., Kale Ö. and Tanışer S. "Seismic Performance Assessment of Base Isolation Systems in Six Hospitals during the Mw7.8 and Mw7.6, 2023 Earthquakes in South-East Türkiye", Earthquake Spectra. (2024) (In Print)

Running, Tennis, Computer Technologies, Board Games, Movies